Drying front formation in topmost soil layers as evaporative restraint
Non-invasive monitoring by magnetic resonance and numerical simulation

Steffen Merz

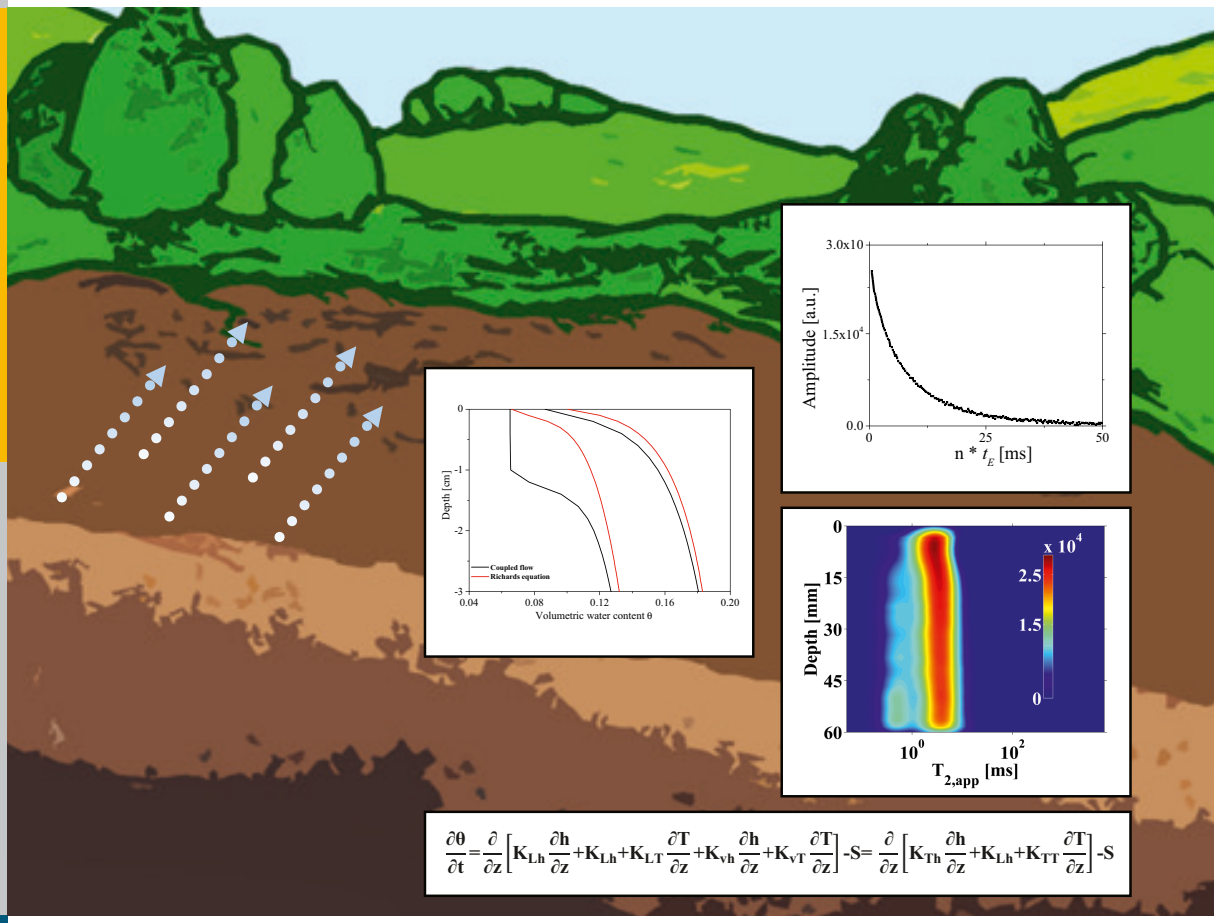

Member of the Helmholtz Association

Energie & Umwelt / Energy & Environment
Band / Volume 376
ISBN 978-3-95806-234-4

JÜLICH FORSCHUNGSZENTRUM

Schriften des Forschungszentrums Jülich
Reihe Energie & Umwelt / Energy & Environment Band / Volume 376

Forschungszentrum Jülich GmbH
Institute of Bio- and Geosciences
Agrosphere (IBG-3)

Drying front formation in topmost soil layers as evaporative restraint Non-invasive monitoring by magnetic resonance and numerical simulation

Steffen Merz

Schriften des Forschungszentrums Jülich
Reihe Energie & Umwelt / Energy & Environment Band / Volume 376

ISSN 1866-1793 ISBN 978-3-95806-234-4

Bibliographic information published by the Deutsche Nationalbibliothek.
The Deutsche Nationalbibliothek lists this publication in the Deutsche
Nationalbibliografie; detailed bibliographic data are available in the
Internet at http://dnb.d-nb.de.

Publisher and Distributor: Forschungszentrum Jülich GmbH
Zentralbibliothek
52425 Jülich
Tel: +49 2461 61-5368
Fax: +49 2461 61-6103
Email: zb-publikation@fz-juelich.de
www.fz-juelich.de/zb

Cover Design: Grafische Medien, Forschungszentrum Jülich GmbH

Printer: Grafische Medien, Forschungszentrum Jülich GmbH

Schriften des Forschungszentrums Jülich
Reihe Energie & Umwelt / Energy & Environment, Band / Volume 376

D 5 (Diss., Bonn, Univ., 2017)

ISSN 1866-1793
ISBN 978-3-95806-234-4

The complete volume is freely available on the Internet on the Jülicher Open Access Server (JuSER)
at www.fz-juelich.de/zb/openaccess.

panta rhei

Acknowledgements

First and foremost, I would like to express my gratitude to my parents for their consistent support during all the chapters of my life so far.

I sincerely thank Prof. Dr. Harry Vereecken, director of IBG-3 and first examiner of my thesis for the opportunity to work on this subject at his institute.

During the course of the years several people were involved in this thesis. Therefore I would like to thank:

- Dr. Andreas Pohlmeier for guiding me all the way through from a B.Sc. student to PhD
- Dr. Dagmar van Dusschoten for providing and maintaining the 4.7T MRI equipment
- Prof. Dr. Bruce Balcom for providing a 6 month stay at the MRI Research Center at the University of New Brunswick what goes along with plenty of fruitful scientific discussions as well as he always came up with a splendid place to spot when been asked for nice places in Canada.
- I would like to thank particularly Dr. Florin Marica for briefing me with the instruments and the workshop guys Jim Merrill and Brian Titus for manufacturing parts of my setup
- Razieh Enjilela for becoming a good friend what goes along with plenty conversations about life, art and nature
- Dr. Nils Borchard, my office mate, for helping me out in tricky situations
- The guys from the IBG-3 electronic workshop (Norman, Ansgar and Ferdie) for getting almost everything running
- The IBG workshop (Mr. Egmen, Mr Schnabel & Mr. Mans) for transferring all my setup ideas to reality
- Markus Duschl for moving around tons of soil, the NMR MOUSE, as well as assisting me with the HYPROP measurements
- The Potato Research Centre in Fredericton/Canada for providing the soil material
- Jennie McPhail from UNB/Canada for doing all the paper work related to my stay
- Dr. Youri Rothfuss for plenty of fruitfully discussions about work and life
- Prof. Dr. Jan Vanderborght for many discussions and support
- Prof. Dr. Andrea Schnepf for being the second thesis examiner
- Prof. Dr. Nicolas Brüggemann for taking the chair of the examination committee
- Prof. Dr. Josef Granwehr for conceding me the time to finalize this thesis

Summary

Evaporation from bare soil surfaces is a highly dynamic process and one major component of the global water cycle. Due to the nature of soils as complex porous materials, the process of water loss to the atmospheric boundary layer causes a considerably moisture variation in space and time on larger scales driven by the interplay between internal flow processes and the atmosphere. Particularly the top few centimeters of a soil constitute the source for vaporized water to be dissipated by the atmospheric boundary layer. Prediction of soil moisture changes on large scales is of various interests with regard to water resources management (e.g. in agriculture). To be able to describe the processes driven by evaporation on large scales, small scale measurements with high spatial resolution of moisture in the topmost soil layer are mandatory. Within this PhD work, different Magnetic Resonance (MR) concepts/apparatus and sequences were applied and assessed to monitor changes in the moisture content of evaporating soils on various scales in high resolution non-invasively while focusing on their field applicability. Particularly focus was spent on the origin of the dry surface layer as it is predicted by theory. Since the concept of single sided MR is of great potential for direct field applications a unilateral single sided sensor and a three magnet array were employed and the results were compared to measurements performed on stationary MR magnets of different concepts.

During the first phase, the moisture development of pure sand exposed to evaporation was studied. A column consisting of medium sand was evaporated and monitored using different echo based and single point imaging methods employed at a 200 MHz stationary MR magnet. The obtained vertical moisture profiles were compared to the results of a 13.4 MHz mobile unilateral single sided MR sensor (NMR-MOUSE) and the pros and cons of each concept were evaluated. As a next step, by proving the convenience of the unilateral sensor, a mini lysimeter consisting of a silt loam was exposed to evaporation under defined irradiative conditions and soil moisture was monitored using the NMR-MOUSE.

The results validate the predictions of a coupled heat, water and vapor flow model. Since soils naturally possess paramagnetic impurities and the clay content can vary considerably, MR measurements become challenging in terms of a decreasing signal to noise ratio (SNR) together with significantly accelerated signal decay what gets particularly tricky with progressing desaturation. These aforementioned inherent soil properties justify the need for feasible MR pulse sequences which ideally reduce signal decrease by relaxation acceleration due to internal and external magnetic field gradients and short detection times to reduce signal loss.

Therefore, as the second step, two echo based and two single point imaging methods were employed on a 8.5 MHz vertical magnet in order to evaluate the feasibility of this two fundamentally different methods for soil moisture monitoring using a natural silt loam exposed to evaporation in an environmen-

tal chamber under isothermal conditions and under a constant vapor pressure deficit. In addition to the 8.5 MHz magnet the sample was monitored by means of a 2.2 MHz unilateral three magnet array in order to assess the different concepts of mobile MR sensors for drying studies with focus on field applications.

After this methodological progress the moisture development over time of two sandy loam columns of different extend and a silt loam column exposed to evaporation using a climate chamber were monitored by means of the SPRITE and an echo based single point imaging technique employed on both, the 8.5 MHz and 2.2 MHz apparatus. The relevance of the classical Richards approach considering only capillary water flow and a coupled water, vapor and heat flow model were assed and cross validated using the measured evaporation rates and the MR monitored moisture profiles as a function of time. The MR data was further used to evaluate the coupled model approach since this model is favorable over the classical Richards approach when focusing on the origin and development of a dry surface layer at S2 evaporation over time.

Concluding on the basis of the conducted experiments , ^{1}H MR as a huge potential for non-invasive monitoring of water content and water environment (pores) of opaque porous systems such as soils from the mm to the cm scale in high spatial resolution. The fact that robust and fast MR methods need to be employed when investigating moisture changes in the top layer of desaturated soils in the field entails the need for MR apparatuses particularly designed for field measurements. A less heavy setup is required where fast methods can be applied which does not considerably compact the soil, does not suffer from low SNR and is immune to parasitic frequencies.

Next to measurements, there is a constant need to improve the estimation of soil water fluxes what involves the improvement of soil water flow models. This inevitable step will help us to gain a better understanding of water depletion in and from topmost soil layers at progressing desaturation.

Zusammenfassung

Die Wasserverdunstung von unbewachsenen terrestrischen Bodenoberflächen ist eine der wesentlichen und zeitgleich hochkomplexen Komponenten des globalen Wasserkreislaufs. Die bei mikroskaliger Betrachtung über einzelne Poren an der Bodenoberfläche erfolgende Verdunstung ist im feldskaligen Betrachtungsbereich ursächlich für erhebliche räumliche sowie zeitliche Wassergehaltsvariationen. Als Antriebskräfte fungieren hierbei Flussprozesse, welche durch die in mit der atmosphärischen Grenzschicht in stetiger Wechselwirkung stehenden oberen Bodenschicht hervorgerufen werden. Dabei entscheiden die ersten Zentimeter des A- Horizontes eines Bodens über die Effektivität der Wasserabgabe an die Atmosphäre. Sind die Nachleitwiderstände im Boden geringer als die atmosphärischen Kräfte erfolgt die Verdunstung des Wasser unmittelbar an der Bodenoberfläche. Sinkt in Folge stetiger Verdunstung der Bodenwassergehalt und kann keine Nachleitung aus z.B. Grundwasserleitern erfolgen, evaporiert das Wasser im Boden und wird in Form von Wasserdampf über Diffusionsprozesse sowie thermische Gradienten zur Oberfläche transportiert und über die atmosphärische Grenzschicht abgeführt. Sowohl langfristige als auch mittelbare Abschätzungen und Kalkulationen dieser Wassergehaltsänderungen und damit einhergenden Wasserverfügbarkeiten im Oberboden sind von mannigfaltigem Interesse im landwirtschaftlichen Bereich, was die Verfügbarkeit von hochaufgelösten Wassergehaltsmessungen zur Vailidierung dieser Modelle nach sich zieht. Im Rahmen dieser Doktorarbeit wurde das Austrockungsverhalten verschiedener Bodenarten im Labormaßstab mittels nicht- invasiver Messverfahren untersucht. In drei ineinander übergreifenden Versuchsphasen wurde dabei die zeitliche Änderung der Bodenfeuchte unter verschiedenen Umweltbedingungen mittels verschiedener Methoden der nicht-invasiven ^{1}H - Magnetresonanz (MR) räumlich aufgelöst. MR ermöglicht zum einen die Quantifizierung der Bodenfeuchte im Millimeterbereich, zum anderen liefert sie Informationen über den Sättigungsgrad der Poren und erlaubt somit Rückschlüsse über Wasserbewegungen innerhalb des Porensystems. Durch diese Eigenschaften wird die Methode der MR besonders interessant für den direkten Feldeinsatz, weshalb in dieser Arbeit primär auf die Feldeignung diverser MR Konzepte sowie Methoden eingegangen wurde.

Für alle Bodentypen konnte das in der Literatur beschrieben Austrockungsverhalten festgestellt und mittels MR beobachtet werden, wobei eine charakteristische Verschiebung gemessen an der Porengrößenverteilung hin zu kleineren gesättigten oder teils mit Wasser gefüllten Poren mit Ausprägung der trockenen Oberschicht gefunden wurde. Erwiesen sich für einen reinen mittelkörnigen Sand noch alle MR Methoden als geeignet, änderte sich dies deutlich mit erhöhten Lehmgehalten sowie ferromagnetischen Anteilen im Boden. Das Konzept der transportablen unilateralen MR MOUSE ermöglichte eine vertikale Auflösung der Bodenfeuchte eines Schlufflehms von 140 µm, zeigte sich

jedoch anfällig gegenüber umweltbedingten Störfrequenzen und lies darüber hinaus für diese Auflösung keine Rückschlüsse auf die Porenwasserverteilung zu. Für die Messung derartiger lehmhaltiger Böden zeigte sich deutlich, dass nur bestimmte, schnelle MR Methoden nutzbar sind um ein umfassendes Bild über der Sättigungszustand des Bodens und die Ausprägung der trockenen Bodenoberschicht zu gewinnen. Mittels speziell auf derartige Anwendungen zugeschnittener MR Methoden war es schlussendlich möglich, das Austrockungsverhalten verschiedener lehmhaltiger Bodenarten auf unterschiedlichen Längenskalen hochaufgelöst zu beobachten. Die dabei erhaltenen Daten wurden für die Validierung eines gekoppelten Wasser-, Wärme- und Dampftransportmodelles genutzt und dessen Notwendigkeit in der Anwendung gegenüber dem gängigen Richardsmodell demonstriert.

Die Ergebnisse der Arbeit zeigen deutlich, dass mittels MR räumlich hochaufgelöste Bodenfeuchtedaten auf verschiedenen Skalen gewonnen werden können, welche in Zusammenhang mit Relaxationsdaten ein umfassendes Bild sowohl des absoluten Feuchtegehaltes als auch dessen Verteilung liefern. Die mittels dieser Methode erhaltenen Daten zeigen weiterhin, dass, unabhängig von der Bodenart, die Ausprägung einer trockenen Oberbodenschicht die Wasserabgabe des Bodens deutlich einschränkt. Ferner wurde die Validierung eines gekoppelten Flussmodells mittels der MR Daten demonstriert. Insgesamt zeigte sich, dass die Ausprägung der trockenen Oberbodenschicht mittels MR im Labormaßstab anhand verschiedener Bodenarten und Skalen beobachtet und mittels Modellierung validiert werden konnte. Ist eine direkte Übertragung der meisten MR Methoden für Feldmessungen noch nicht möglich, sollte dies in naher Zukunft mit vertretbarem technischen Aufwand realisierbar werden, was weitere Perspektiven, wie z.B. feldskalige Bodenfeuchtemessungen eröffnet.

Table of contents

List of Tables

List of Figures

List of Acronyms

^{1}H MR	Hydrogen proton MR
ADC	analog digital converter
CPMG	Carr-Purcell-Maiboom-Gill
CRP	constant rate period
CT	computer tomography
CTI	constant time imaging
FID	Free Induction Decay
FOV	Field of View
FRP	falling rate period
IR	Inversion Recovery
NMR	Nuclear Magnetic Resonance
MEMS	Multi Echo Multi Slice
MOUSE	MObile Universal Surface Explorer
MR	Magnetic Resonance
MRI	Magnetic Resonance Imaging
NE	number of echoes
NP	number of points
NS	number of scans
pF	water retention curve
rf	radio frequency
S1	stage I evaporation
S2	stage II evaporation
SE	Spin Echo
SEMS	Spin Echo Multi Slice
SNR	signal to noise ratio
SPI	Single Point Imaging
SPRITE	Single Point Ramped Imaging with T_1 Enhancement
vpd	vapor pressure deficit

List of Symbols

α	reciprocal air entry value (van Genuchten parameter)	[mm, cm]
α	rf-pulse flip angle	[°]
β	shape factor for simple pore geometries	[-]
β_0	surface tension of water at 25°C	[N m^{-1}]
$\boldsymbol{B_0}$	external polarizing magnetic field strength	[T]
$\boldsymbol{B_1}$	alternating magnetic field strength	[T]
C_a	air volumetric heat capacity	[J m^{-3} K^{-1}]
C_v	volumetric heat capacity for vapor	[J m^{-3} K^{-1}]
C_w	volumetric heat capacity for water	[J m^{-3} K^{-1}]
D	diffusion coefficient of water	[m^2 s^{-1}]
D_v	water vapor diffusivity in soil	[m^2 s^{-1}]
e	evaporation rate	[mm d^{-1}]
e_{pan}	potential or pan evaporation rate	[mm d^{-1}]
e_s	saturation vapor pressure	[kPa]
ε	porosity	[-]
g	acceleration due to gravity	[m s^{-2}]
G	heat flux into the soil	[W m^{-2}]
$\boldsymbol{G}$	magnetic field gradient	[T m^{-1}]
$\boldsymbol{G_{slice}}$	slice selective magnetic field gradient	[T m^{-1}]
$\boldsymbol{G_v}$	frequency encoding magnetic field gradient	[T m^{-1}]
$\boldsymbol{G_\phi}$	phase encoding magnetic field gradient	[T m^{-1}]
$\boldsymbol{G_{\phi(x, y, z)}}$	phase encoding magnetic field gradient in x, y, z direction, respectively	[T m^{-1}]
$\gamma/2\pi$	gyromagnetic ratio	[Hz T^{-1}]
H	sensible heat flux	[W m^{-2}]
H_r	fractional relative humidity	[%]
h	pressure head	[cm]
$\hbar$	Reduced Planck's constant (also Dirac constant)	[J s]
$\boldsymbol{I}$	spin quantum number	
k	Boltzmann's constant	[J K^{-1}]
$\boldsymbol{k}$	reciprocal space vector	[m^{-1}]
$k_{v, \phi}$	frequency and phase components of the reciprocal	[m^{-1}]

K_{Lh}	isothermal hydraulic conductivity	[m s^{-1}]
K_{LT}	thermal hydraulic conductivity	[m K^{-1} s^{-1}]
K_{Th}	isothermal total hydraulic conductivity	[m s^{-1}]
K_{TT}	thermal total hydraulic conductivity	[m^2 K^{-1} s^{-1}]
K_{vh}	isothermal vapor hydraulic conductivity	[m s^{-1}]
K_{vT}	thermal vapor hydraulic conductivity	[m^2 K^{-1} s^{-1}]
K_s	saturated hydraulic conductivity	[cm d^{-1}]
$K(\theta)$	unsaturated hydraulic conductivity	[cm d^{-1}]
L	volumetric latent heat of vaporization	[J m^{-3}]
l	pore connectivity coefficient (van Genuchten parameter)	[-]
λ	apparent thermal conductivity	[J m^{-1} s^{-1} K^{-1}]
$\boldsymbol{M}$	macroscopic magnetization vector	[A m^{-1}]
$\boldsymbol{M_0}$	intial magnetization	[A m^{-1}]
$\boldsymbol{M_z^0}$	$\boldsymbol{M}$ in thermodynamic equilibrium	[A m^{-1}]
M_w	molecular weight of water	[kg mol^{-1}]
$M_{x,y,z}$	macroscopic magnetization in x, y, z	[A m^{-1}]
	direction, respectively	
$\boldsymbol{\mu}$	magnetic moment	[J T^{-1}]
n	number of spins / $(mm)^3$	[-]
n	pore size distribution (van Genuchten parameter)	[-]
P	barometric pressure	
q_h	total heat flux	[J m^{-2} s^{-1}]
q_i	flux density	[cm min^{-1}]
q_l	liquid water flux	[m s^{-1}]
q_v	water vapor flux	[m s^{-1}]
$\rho_{1,2}$	T_1 and T_2 surface relaxivity, respectively	[µm s^{-1}]
ρ_B	bulk density	[g cm^{-1}]
ρ_G	grain density	[g cm^{-1}]
ρ_s	water vapor density at the soil surface	[kg m^{-3}]
ρ_a	water vapor density above soil surface at a reference height	[kg m^{-3}]
ρ_w	saturated vapor density	[kg m^{-3}]
r	pore radius	[mm]
r_a	resistance of the atmospheric boundary layer to vapor flow	[s m^{-1}]
r_H	resistance of the atmospheric boundary layer to heat flow	[s m^{-1}]

$\boldsymbol{r}$	coordinate in space	[m]
R	universal gas constant	[J mol^{-1} K^{-1}]
RH	relative humidity	[%]
R_n	net radiation	[W m^{-2}]
$\boldsymbol{S}$	spin angular momentum	[-]
S	sink term	[-]
SH	sensible heat flux	[W m^{-2}]
S/V	ratio of pore surface to fluid volume	[mm^{-1}]
τ	duration of $\boldsymbol{G}_v$ or $\boldsymbol{G}_\phi$	[ms]
τ_p	duration of the rf-pulse	[ms]
τ_s	time between each subsequent FID record point	[ms]
θ	volumetric water content	[cm^3 cm^{-3}]
θ_r	residual volumetric water content	[cm^3 cm^{-3}]
θ_s	saturated volumetric water content	[cm^3 cm^{-3}]
Θ	effective saturation	[-]
t_E	echo time	[ms]
t_p	time after pulse	[ms]
t_R	repetition time	[ms]
T	absolute temperature	[K]
T_a	air temperature	[K]
T_s	soil surface temperature	[K]
T_1	longitudinal or spin-lattice relaxation time	[s]
T_2	transversal or spin-spin relaxation time	[s]
T_2^*	enhanced T_2 relaxation time due to $T_{,inhomogeneous}$	[s]
$T_{2,\,app}$	observable, parameter dependent relaxation time (“apparent”)	[s]
$T_{2,\,bulk}$	relaxation time of the bulk fluid	[s]
$T_{2,\,diffusion}$	relaxation time due to diffusion	[s]
$T_{,inhomogeneous}$	enhanced signal decay due to field inhomogneities	[s]
$T_{2,\,surface}$	surface relaxation time at a fluid-solid interface	[s]
t	time	[s]
υ_0, ω	Larmor frequency	[s^{-1}]
ω_{slice}	Larmor frequency under influence of $\boldsymbol{G}_{slice}$	[s^{-1}]
x, y, z	main directions in the laboratory frame	[-]

General Introduction

Soil is one of the essential factors crucial for human life and with respect to the global water cycle, the major key component determining the water transport between the atmosphere and the phreatic water through the unsaturated or vadose zone [*Nimmo*, 2009]. Depletion of moisture can be specified with respect to the evaporating surface, where two regimes are distinguished: i) Transpiration, the water loss through plant tissues and ii) Evaporation, where water is withdrawn from bare surfaces such as soils and plants (intercepted water). If i and ii occur simultaneously the process is termed evapotranspiration. 60% of terrestrial precipitation is returned by plant transpiration (40%) and evaporation (20%) [*Oki and Kanae*, 2006] whereby the evaporation process consumes approximately 25% of the incoming solar energy what amounts to $\approx 4.5 \times 10^3$ Terawatts [*Trenberth et al.*, 2009]. Thus, soil moisture loss due to evaporation plays a key role in the portioning of incoming solar energy into sensible and latent heat and affects air temperature, relative humidity and the origin of clouds which in turn have an impact on the global energy cycle as well as influence the precipitation amount [*Dai et al.*, 1999; *Seneviratne et al.*, 2010]. Soil thermal and hydraulic properties are strongly linked and coupled to the atmospheric conditions but processes and mechanisms within the soil control to a large extend not only the dynamics of evaporation but can determine a priori how much water is lost to the atmosphere. The strong coupling between these processes leads to highly dynamic interactions and variability in the porous medium and gives rise to nonlinear behavior. The gist about evaporation lays in its nature as a two stages process for the majority of porous materials (Figure 1). If a porous medium initially saturated with water is exposed to evaporation, the depletion of water occurs in two distinct stages if: i) a continual supply of heat exists that meets the latent heat requirement ii) a vapor pressure deficit (The difference between the theoretical pressure exerted by vapor saturated air at a given temperature and vapor that is currently held in the air.) prevails at the soil surface and iii) a continual supply of water to the evaporation site is sustained. During the first initial stage the proceeding evaporation process gives rise to an increasing matric suction head at the surface due to a constantly increasing number of liquid-gas interfaces which are controlled by gravity, capillary and viscous forces. As long as water menisci are able to balance these forces and sustain a continuous hydraulically connected liquid network (film region), water will flow from the saturated region to the evaporating surface induced by capillarity and driven by changes in the curvature of the liquid-gas menisci ("capillary pumping"). This stage, controlled by the evaporativity of the atmosphere, is often referred to as constant rate period (CRP) since meteorological parameters such as solar radiation, air temperature, air humidity and wind speed determine the available energy for vaporization and the amount of moisture which will be purged from the porous medium surface.

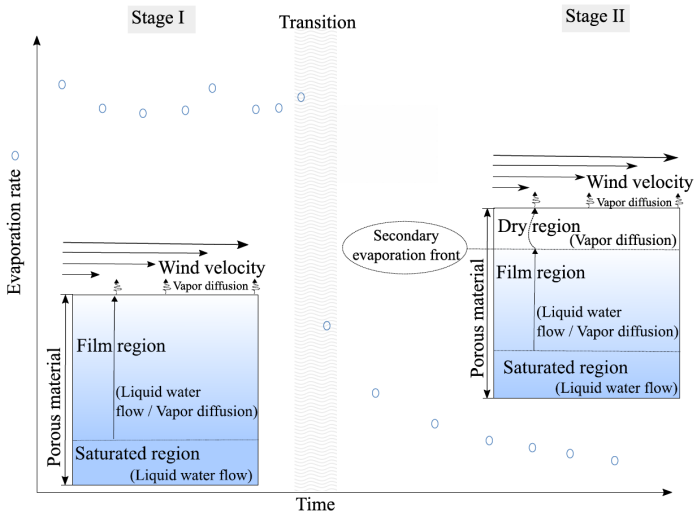

Figure 1. Cross section of a porous medium with: i) an external boundary layer where the vapor is purged ii) a fully saturated innermost region where the voids are fully occupied by water (saturated region) iii) an intermediate innermost region where voids are occupied by water or air (film region) and at stage II iv) a dry region only occupied by air (saturated vapor pressure).

Since atmospheric conditions are major driving factors of evaporation during stage I the process is characterized by a constant evaporation rate, close to the rate from a free water surface exposed to the same conditions. As long as moisture is drawn upward to sustain the evaporative demand and the moisture gradient can compensate for the decreasing hydraulic conductivity *S1* will persist. But with progressing drying more films become detached from the porous medium surface because capillary flow cannot be sustained over larger lengths. Now, an increasing dry region between the surface and the secondary evaporation front inside the porous medium develops and drying is controlled by diffusion through the dry layer. As a consequence the evaporation rate drops significantly what marks the onset of stage II or falling rate period (FRP) since the dry layer constitutes an evaporative restraint. The most common methods for estimating evaporation and evapotranspiration by using net radiation, wind speed, air temperature and relative humidity are the ones introduced by Penman [*Penman*, 1948] and Monteith [*Monteith*, 1965], Priestley and Taylor [*Priestley and Taylor*, 1972] and Penman-Brutsaert [*Katul and Parlange*, 1992]. Since over the course of the years the amount of methods to calculate evaporation has increased drastically and

is therefore behind the scope of the thesis the reader is referred to the standard work of *Brutsaert* [1982] and the comprehensive overview given by *Abtew and Melesse* [2013] and *Novák* [2012].

Water exchange at the soil surface is a key variable in land-surface models [*Desborough et al.*, 1996; *Maxwell and Kollet*, 2008; *Sellers et al.*, 1997] but, since pore scale processes are the major driving force, modeling the dynamic interactions at the bare soil interface requires very detailed models with a high vertical resolution in the order of a few millimeters. Even today evaporation data and particularly moisture data of the topsoil in high spatial resolution for model validation are rare due to their complex nature. Hence, there is a need for non-invasive pore scale monitoring with high spatial resolution over time during moisture depletion in evaporating soils. The simplest approach to determine moisture on small scales are gravimetric techniques but they deliver only a bulk value for a certain volume and are moreover invasive. Other techniques such as tensiometer, microwave methods, electromagnetic applications, neutron scattering or gamma ray are either strongly affected by soil water content and soil composition or cannot be applied easily due to their harmful nature [*Robinson et al.*, 2008; *Vereecken et al.*, 2008] . Magnetic Resonance (MR) methods are advantageous over the aforementioned techniques to bridge the gap between theoretical models and reality, because they provide: i) noninvasive measurements ii) achievable resolutions below 1 millimeter iii) a measured signal which is a direct measure of moisture in the probed volume iv) information not only about the amount of water but also about the environment of the water, the pore size [*Wolter and Krus*, 2005].

The first application of MR on a soil material is reported for 1959 where *Pickett and Lemcoe* investigated the shear strength of a clay-water system. One year later in 1960, *Andreev and Martens* first applied MR to determine moisture of packed podzolized sandy loam samples of various saturations and proved the advantages of this technique in terms of measurement time and accuracy over the gravimetric determination and electrometric methods. Since this time the popularity of this technique in the field of soil science has steadily increased. In 1978 the concept of permanent magnets and pulsed radio frequency was invented by the petroleum industry in order to determine oil reservoirs in geologic formations [*Kleinberg and Jackson*, 2001]. *Gummerson et al.* [1979] reported the use of Magnetic Resonance Imaging (MRI) using slice selection with an achievable resolution < 2 mm on various porous materials during drying. In 1985 *Paetzold et al.* first applied the concept of unilateral or single sided MR in the field to monitor moisture but it still took several years until these instruments became more manageable in terms of weight and size [*Casanova*, 2011; *Marble et al.*, 2007]. The first images of a porous medium during moisture depletion have been recorded in 1989 by *Guillot et al.* while studying the water distribution as a function of time. *Hinedi et al.* [1993] first employed the concept of pore size distribution on soils using MR relaxation. In the same year *Amin et al.* [1993] mapped the spatial and temporal distributuion of water in

model and real soil blocks in order to asses the feasibility of 2D and 3D MRI. MR imaging and relaxometry methods were constantly enhanced and applied multifarious on porous media and soil materials over the course of the years [*Balcom et al.*, 2003; *Bird et al.*, 2005; *Camaiti et al.*, 2015; *Keita et al.*, 2013; *Marica et al.*, 2014; *Muir and Balcom*, 2012; *Pohlmeier et al.*, 2008; *Stingaciu et al.*, 2009; *Straley et al.*, 1994; *Van der Heijden et al.*, 2009]. Nevertheless, high resolution monitoring of evaporating soils as well as using the concept of unilateral MR still remain rare. Despite other direct visualization techniques like, e.g. dye transport and neutron radiography [*Shokri and Or*, 2011; *Shokri et al.*, 2008] the only investigations on drying of a model soil using MR relaxometry and imaging were reported by *Faure and Coussot* in 2010. The main objective of this thesis was therefore to improve our understanding on the formation of dry surface layers in soils as evaporative restraint by using high resolution MR methods and unilateral portable sensors in order to investigate their ability for direct field application. Firstly, a model soil was exposed to evaporation and high field MR relaxometry and imaging were employed in order to achive vertical high resolution moisture profiles. Additionally, these measurements were compared to a portable mobile unilateral MR sensor. As a step further the portable unilateral MR sensor was employed on a laboratory lysimeter consisting of $4x10^{-2}$ m^3 natural soil material (silt loam) in order to monitor vertical moisture profiles during water depletion where the surface and bottom temperature of the soil where additionally recorded in order to determine the evaporation stages. There are still difficulties and limitations encountered in soil MRI due to the inherent fast relaxation times in natural soils with higher clay content and paramagnetic impurities where MRI images can be either distorted or even larger fractions of water are invisible. These issues are exacerbated with decreasing moisture where relaxation processes are accelerated what coincides with a decreasing signal to noise (SNR) ratio. By this reason, different MR methods with short detection times were assessed on various evaporating soil material in order to identify the most feasible MR method for monitoring moisture in soils with significant clay and silt content. In a third step, the methods which were identified most suitable where employed on a silt loam and a sandy loam using columns of different length in order to quantify moisture changes while the samples were exposed to evaporation under constant ambient conditions. The MR relaxation data in combination with high resolution vertical moisture profiles were then compared to simulation results by using i) the classical Richards' approach and ii) a coupled water, vapor and heat flow model.

This thesis is organized as follows:

Chapter I deals with the investigation of water content changes and the origin of a dry surface layer under desaturated conditions in a sand exposed to evaporation monitored by a high field 4.7 MR scanner in comparison to a portable unilateral MR sensor (NMR-MOUSE) [*Merz et al.*, 2014].

Chapter II demonstrates the feasibility of the portable unilateral sensor to monitor water content changes of a natural silt loam on the dm scale were the results were validated by means of a coupled water, vapor and heat flow model [*Merz et al.*, 2015a].

Chapter III explores the potential of MR by comparing different stationary MR and unilateral concepts at low and higher filed strength to monitor moisture in high resolution in desaturated soils with dry topmost layers which possess high amounts of clay and silt [*Merz et al.*, 2015b]

Chapter IV compares moisture profiles of a silt loam and a sandy loam investigated by MR to a coupled water, vapor and heat flow model and the classical Richards' approach. Soil columns of two different sizes and soils exposed to evaporation under constant ambient conditions were monitored by means of MR and compared to numerically simulated vertical moisture profiles of a coupled model focusing on the increasing dry surface layer under desaturation [*Merz et al*., 2016].

Due to the fact that the results chapters address very different aspects of the main research question, each chapter consist of objectives, introduction and a material and method section. A general overview on MR and the model approach are given as two separate chapters prior to the result section.

I. NMR – Theoretical Aspects

If nuclei with an intrinsic magnetic dipole moment $\boldsymbol{\mu}$ resulting from the spin angular momentum $\boldsymbol{S}$ are placed in a static external magnetic field $\boldsymbol{B_0}$ pointing in *z*-direction by definition two physical phenomena occur: alignment and precession. The spin angular momentum vector exists in a number of different quantum states ($\boldsymbol{I}$) which take the value of zero, positive integers or half integers ($\boldsymbol{I}$ = 0, 1/2, 1, 3/2, 2, …). In an external magnetic field $\boldsymbol{\mu}$ will align in different orientations with respect to $\boldsymbol{B_0}$ where the number of states is determined by $2\boldsymbol{I}+1$. For ^{1}H nuclei with spin= ½ only two states (+ ½ and – ½) are possible, where the energy difference (Δ E) between those states is proportional to $\boldsymbol{B_0}$. The resonance condition is given by $(\Delta E) = \hbar|\gamma|\boldsymbol{B}$ and therefore the resonance frequency ($=(\Delta E/h)\ \upsilon_0 = \boldsymbol{B_0}\gamma/2\pi$, what is known as the Larmor frequency. In thermal equilibrium the population of + ½ states and – ½ states is described by Boltzmann's law

$$\frac{n_{-1/2}}{n_{+1/2}} = exp\left(-\frac{(h/2\pi)\gamma \boldsymbol{B_0}}{k\,T}\right) \tag{1.1}$$

where *n* represents the population in the lower (+) and upper (-) energy levels, *h* is the Planck's constant, γ is the magnetogyric ratio, *k* the Boltzmann's constant and *T* the absolute temperature.

As given by Equation 1.1 more components pointing up than down the overall sum is a vector pointing up according to

$$\boldsymbol{M} = \sum \mu_{+z} - \sum \mu_{-z} \tag{1.2}$$

in the direction of $\boldsymbol{B_0}$. There is no component observable for the *xy* plane because the components have an equal probability of pointing in any direction for both, the -1/2 and +1/2 state and therefore the vector sum is zero.

In thermal equilibrium the magnetization is denoted as $\boldsymbol{M_z^0}$. If a radiofrequency field $\boldsymbol{B_1}$ (rf-pulse) is applied at Larmor frequency transverse to *z*, $\boldsymbol{M_z^0}$ is perturbed from equilibrium and flips towards the transverse (*xy*) plane. The angle α $\boldsymbol{M}$ is rotated about $\boldsymbol{B_1}$ is equal to

$$\alpha = \gamma \boldsymbol{B_1} \tau_p \tag{1.3}$$

known as the flip angle where for example a 90° pulse causes a complete transfer of the longitudinal magnetization (*z*) in the transverse plane (*xy*). After the rf-pulse the precessing transversal magnetization

$\boldsymbol{M}$ induces a measurable electromagnetic force in a receiver coil together with the thermal noise. The time dependence of $\boldsymbol{M}$ in the presence of $\boldsymbol{B_0}$ in the vector model is described by the Bloch Equations [*Bloch*, 1946]:

$$\frac{dM_x}{dt} = \gamma M_y(B_0 - \omega/\gamma) - \frac{M_x}{T_2} \tag{1.4a}$$

$$\frac{dM_y}{dt} = \gamma M_z B_1 - \gamma M_x(B_0 - \omega/\gamma) - \frac{M_y}{T_2} \tag{1.4b}$$

$$\frac{dM_z}{dt} = \gamma M_y B_1 - \frac{M_z - M_0}{T_1} \tag{1.4c}$$

After the rf-pulse is switched off the signal starts to decay, what is called Free Induction Decay (FID), where two types of relaxation occur, causing the signal loss in the *xy*-plane. The recovery of the longitudinal magnetization in *z* direction (thermal equilibrium) based on the release of absorbed energy to the surroundings (lattice) called spin-lattice or longitudinal T_1 relaxation. This process is described by Equation 1.4c with the solution

$$M_z(t) = M_0\left(1 - exp\left\{-\frac{t}{T_1}\right\}\right) \tag{1.5}$$

where M_0 denotes the initial magnetization at time=0. The transverse magnetization is the sum of magnetization vectors from different part of the excited volume experiencing a homogenous $\boldsymbol{B_0}$. These vectors are called isochromats. After the application of an rf- excitation pulse some isochromats experience a larger magnetic field and thus precess faster than those experience a smaller field. As a consequence the isochromats get out of phase (dephasing). This is the second type of relaxation called spin-spin or transverse T_2^* relaxation driven by interactions among individual spins and the local field inhomogeneities which is described by Equation 1.4a and 1.4b with the solution

$$M_{xy}(t) = M_0\, exp\left\{-\frac{t}{T_2^*}\right\}. \tag{2.6}$$

The inhomogeneities are driven by instrumental imperfections or susceptibility effects between different materials (e.g. pore fluid and the solid matrix) and para- or ferromagnetic impurities.

Relaxation Mechanisms of Liquids in Porous Media

T_1 and T_2 relaxation are driven by magnetic interactions between protons, where the T_1 relaxation rate is given by

$$1/T_1 = 1/T_{1,\,bulk} + 1/T_{1,\,surface} \tag{1.7}$$

where $T_{1,\,bulk}$ is the bulk fluid relaxation rate and $T_{1,\,surface}$ the relaxation time of the fluid resulting from pore surface relaxation. The transverse relaxation rate in porous media can be expressed by

$$1/T_2^* = 1/T_{2,app} + 1/T_{2,\,inhomogeneous} \tag{1.8}$$

where $1/T_{2,\,inhomogeneous}$ describes dephasing due to static inhomogeneities of the magnetic field. $1/T_{2,app}$ is the apparent relaxation time which can be divided into three main processes:

$$1/T_{2,app} = 1/T_{2,\,bulk} + 1/T_{2,\,surface} + 1/T_{2,\,diffusion.} \tag{1.9}$$

$1/T_{2,bulk}$ is the relaxation rate in a uniform field for bulk solutions, usually in a range of 0.3333 s^{-1} for pure water. The estimation of pore size distributions from T_2 measurements assumes a fast diffusion regime where relaxation at the pore surface is much slower compared to the diffusional transport of spins towards the surface. Relaxation in the fast diffusion regime occurs when the diffusional motion of the ^{1}H proton through the entire pore volume is faster compared to the surface relaxation [*Keating and Knight*, 2012]. T_2 of a fluid in a single pore is related to surface relaxation and the surface-to-volume (*S/V*) ratio:

$$1/T_{2,\,surface} = \rho_2 (\mathrm{S/V})_{\mathrm{pore}}. \tag{1.10}$$

This term provides the link between pore size and relaxation times by describing the surface relaxation at the fluid-solid interface, where ρ_2 is the T_2 surface relaxivity parameter which varies with mineralogy and describes the capacity of a solid surface to enhance relaxation. S/V_{pore} is the ratio of pore surface to fluid volume and can also be expressed as β/r, where r is the pore radius and β is a shape factor for simple pore geometries (1= planar, 2 = cylindrical, 3 = spherical). The signal loss due to diffusion in gradients in the short diffusion time regime is described by [*Mitchell et al.*, 2010]:

$$1/T_{2,\,diffusion} = D(\gamma G t_E)^2 / 12 \tag{1.11}$$

where D is the molecular diffusion coefficient of the liquid, G the magnetic field gradient and t_E the inter-echo spacing. Finally, the relaxation rate $1/T_{2,inhomogeneous}$ can be compensated for by a Hahn echo [*Hahn*, 1950] or a Carr-Purcell-Meiboom-Gill (CPMG) [*Meiboom and Gill*, 1958] echo train which is the standard technique for measuring transverse relaxation. The term "apparent" in Equation 1.9 refers to the fact that the observable rate depends on the choice of the experimental parameter t_E, which controls the diffusion term [*Pomerantz et al.*, 2008].

The Free Induction Decay (FID) and Carr-Purcell-Meiboom-Gill (CPMG) method

As described in the preceding the FID decay is always enhanced due to instrumental imperfections. This enhanced phase spread due to inhomogeneities can be compensated for what was discovered by Hahn in 1950 [*Hahn*, 1950]. The Spin Echo (SE) method enables to distinguish between the homogenous decay and the inhomogeneous decay. The method starts similar to the FID measurements by employing an rf-excitation pulse of flip-angle α (commonly α = 90°).

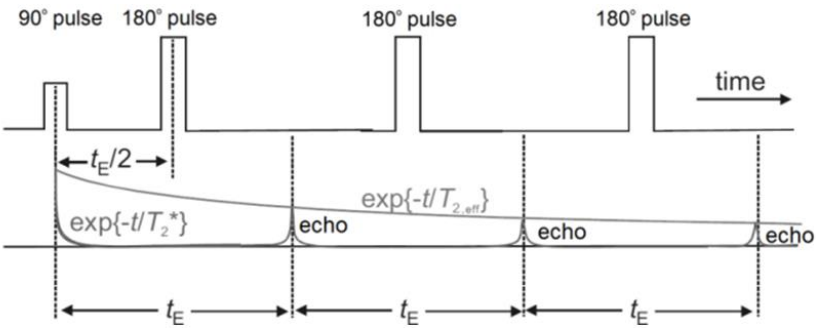

Figure 2. Carr-Purcell-Meiboom-Gill (CPMG) method. After a 90° rf excitation pulse a series auf subsequent n 180° pulses is followed at time $n*t_E$ yielding an echo decay train of n echoes where the enhanced decay due to instrumental imperfections and possible susceptibility effects has been removed and thus the decay is only driven by the fluctuating microscopic magnetic fields (spin-spin interaction). Modified after *Behroozmand et al.* [2015].

Instead of recording the decaying signal after the receiver dead time a second pulse of typically either twice the amplitude or the duration of the first pulse (commonly α = 180°) is applied after a time midway the 90° and the first 180° pulse ($t_E/2$) (Figure 2). This leads to a refocusing of the phase spread by inverting the sign of the phase acquired previous to the second pulse, where the refocused isochromats generating a signal at a certain time what is called echo and the corresponding time t_E, the echo time. In 1954 Carr and Purcell [*Carr and Purcell*, 1954] proposed the use of subsequent 180° pulses during one shot.

One major drawback of this sequence was the fact that pulse imperfections lead to a decay of the echo train. To overcome this issue Meiboom and Gill [*Meiboom and Gill*, 1958] introduced a 90° phase shift of the rf of the π/2 pulse relative to the phase of the π pulses, what led to the most robust method frequently used for porous media, the Carr-Purcell-Meiboom-Gill (CPMG) method. As illustrated in Figure 2 CPMG measurement typically consists of a 90° rf excitation pulse and a series of subsequent 180° pulses where the amplitude of the echoes are recorded yielding a decay curve where the effect of $T_{2,inhomogeneous}$ has been removed.

Magnetic Resonance Imaging (MRI)

In an MR imaging experiment the MR spectrum maps the density of spins in a certain volume along a gradient axis. External field gradients $\boldsymbol{G}$ are applied in order to achieve a spatially resolved signal, where the Larmor frequency becomes depended on the position $\boldsymbol{r}$:

$$\omega(\boldsymbol{r}) = \gamma\,(B_0 + \boldsymbol{G}\cdot\boldsymbol{r}). \tag{1.12}$$

In the following the process of spatial encoding will be described for of the fundamental techniques in MRI, Spin Echo Multi Slice (SEMS) (Figure 3) and Single Point Imaging (SPI) (Figure 4) methods. It should be noted that besides spin echo methods a second type of method exists which generates an echo. This method makes use of the magnetic field gradients in order to refocus the signal and is therefore termed gradient echo. Since this method falls out of the scope of this thesis it will not be explained in detail and the reader is referred to *Markl and Leupold* [2012] and *Hennig* [1991].

The slice selective gradient G_{slice}

If a field gradient $\boldsymbol{G_{slice}}$ (Figure 3 first line) is applied in a desired direction in the presence of the rf-pulse only those spins at the plane whose ω_{slice} equal the rf-frequency will resonate. This procedure is termed slice selection, where the slice thickness can be determined either by the bandwidth of the pulse and the strength of $\boldsymbol{G_{slice}}$. Since $\boldsymbol{G_{slice}}$ dephases the magnetization in the applied direction, an inverse slice selective gradient pulse is applied right after $\boldsymbol{G_{slice}}$. For the described SEMS method $\boldsymbol{G_{slice}}$ needs to be applied also during the application of the refocusing pulse after time $t_E/2$. In order to select multiple slices of the sample under question the center frequency of the rf-pulse can be modified whereat $\boldsymbol{G_{slice}}$ is kept constant in strength and a gap is commonly introduced to avoid signal overlap from vicinal slices (“cross talk”).

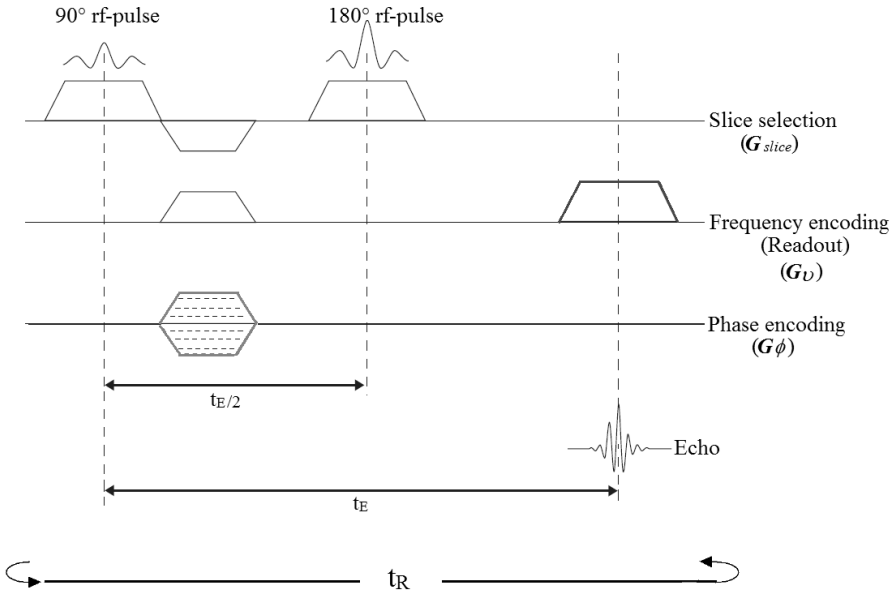

Figure 3. Basic pulse diagram of a Spin Echo (SE) sequence. The slice selective gradient applied ($\boldsymbol{G}_{\text{slice}}$) during the 90° rf-pulse dephases the magnetization along the direction of slice selection. An inverse slice selective gradient pulse is applied afterwards to compensate this effect. After the 90° pulse a frequency ($\boldsymbol{G}_{\upsilon}$) and phase encoding ($\boldsymbol{G}_{\phi}$) gradient is applied. After time $t_E/2$ a 180° rf- pulse is applied in the presence of $\boldsymbol{G}_{\text{slice}}$ which refocuses the spin phase spread where a signal (echo) is generated after time t_E (echo time) in the presence of $\boldsymbol{G}_{\upsilon}$. The sequence is repeated after a delay time t_R (repetition time) where the strength of $\boldsymbol{G}_{\phi}$ is incrementally ramped in equal steps for each cycle (dotted lines).

The frequency Gυ and phase Gϕ encoding gradients

The spatial localization within the plane of a selected slice is a two-step process where additionally gradient fields, $\boldsymbol{G}_{\upsilon}$ and $\boldsymbol{G}_{\phi}$ are introduced either parallel or perpendicular to $\boldsymbol{B}_{\boldsymbol{0}}$. These gradients characterize each spin isochromat by a unique frequency and phase. To achieve information on the location of the protons in the selected slice a static gradient field $\boldsymbol{G}_{\upsilon}$ is applied. Under the influence of $\boldsymbol{G}_{\upsilon}$ the frequency of each spin isochromat differs and is linearly related to certain spatial location along the direction of $\boldsymbol{G}_{\upsilon}$. This gradient separates the signal according to its location along the first dimension and is commonly termed frequency encoding or readout gradient. As indicated in Figure 3 the gradient typically consists of a prephasing gradient lobe and a readout gradient lobe separated by the 180° refocusing pulse. Once $\boldsymbol{G}_{\upsilon}$ has separated the signal according to its location along the first dimension, another gradient will further

separate the signal from each location. To separate the signal components along the second dimension in the slice a gradient field $\boldsymbol{G_\phi}$ induces a phase shift on the spins. While $\boldsymbol{G_\phi}$ is applied after the 90° rf-pulse each spin along this direction is subject to a unique magnetic field strength causing an increase in frequency according to Equation 1.13 and thus a persistent phase shift after $\boldsymbol{G_\phi}$ is switched off. $\boldsymbol{G_\phi}$ is applied at different strength for each subsequent sequence cycle in order to achieve a predefined image resolution. After the spins are spatial encoded a 180° rf-pulse is employed and an echo forms after time t_E in the presence of $\boldsymbol{Gv}$. The sequence can be repeated several times (after a delay t_R, usually 5x T_1) determined by a predefined image resolution in the direction of by $\boldsymbol{G_\phi}$. Methods using spin echoes exist in various forms, e.g. multi echo, fast spin echo and combined gradient and spin echo methods. Because SE methods on one hand require relatively long scan times due to a long t_R and the desired image resolution in the direction of $\boldsymbol{G_\phi}$ and on the other hand are open to image distortions due to the applied frequency encoding, fast scanning methods are desirable. Since one main issue of SE imaging relates to the frequency encoding, another common MR method is Constant Time Imaging (CTI) or Single Point Imaging (SPI) where all spatial information is obtained by using $\boldsymbol{G_\phi}$. A single data point of the FID is collected in the presence of $\boldsymbol{G_{\phi(x,\,y,\,z)}}$ at a fixed evolution time t_p after the excitation pulse. The applied rf- pulse is commonly chosen with $\alpha < 90°$ (usually <10°) and only $\boldsymbol{G_\phi}$ gradients are applied for spatial encoding. Figure 4 shows the schematics of a typical 3D SPI method where $\boldsymbol{G_\phi}$ encodes all spatial directions. To achieve a full representation of the sample the sequence is repeated several times, depending on the chosen image resolution, by incrementally ramping the strength of $\boldsymbol{G_{\phi(x,\,y,\,z)}}$. Since the flip angle is much smaller compared to SE methods what leads to a reduction of t_R, the measurement time is sufficiently shorter.

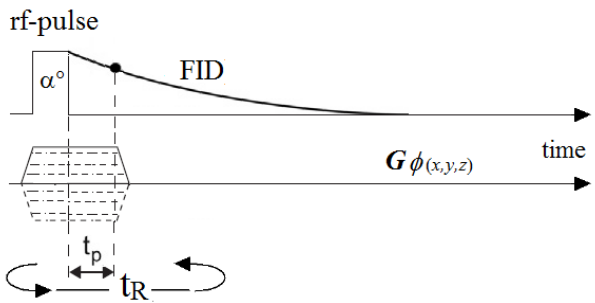

Figure 4. Conventional Single Point Imaging (SPI) pulse sequence.
Each gradient step corresponds to one sample excitation.

The k-space formalism

For all MR methods the acquired time domain signal is digitalized by means of an analog-digital-converter (ADC) and a virtual reciprocal space, called k-space, is discretized in a particularly fashion depending on the MR method. For a simple SE measurement the k-space is defined as:

$$k_v(t) = \frac{\gamma}{2\pi} \int_0^t G_v(\tau) d\tau \tag{1.13}$$

and

$$k_\phi(t) = \frac{\gamma}{2\pi} \int_0^t G_\phi(\tau) d\tau \tag{1.14}$$

where τ is the duration of the frequency or phase encoding gradient. After a delay of t_R the sequence is repeated until the desired image resolution has been achieved by incrementally ramping the strength of G_ϕ for each cycle. Processing the encoded signal $p(k_x, k_y)$ using a two dimensional Fourier Transform yields to a signal intensity distribution in real space described by:

$$M_0(x,y) = (2\pi)^{-2} \iint p(k_v k_\phi) exp\{-ik_v x\} exp\{-ik_\phi y\} \, dk_v dk_\phi \tag{1.15}$$

MR imaging methods are commonly distinguished in terms of the scheme of ***k***-space acquisition. A detailed description on MR pulse sequences and k-space acquisition can be found in *Bernstein et al.* [2004]; *Gallagher et al.* [2008]; *Mezrich* [1995].

Concepts of MR magnets

Commonly three types of MR magnets are distinguished for creating B_0: i) resistive electromagnets, ii) permanent magnets and iii) persistent superconducting magnets. Superconducting refers to the fact that once the magnet is charged a stable magnetic field is sustained without an external supply of current due to superconducting wires which need to be kept close to absolute zero. The cryogen system consists of a dewar filled with liquid helium surrounded by a second dewar filled with liquid nitrogen. A thermally isolated bore is located in the center of the superconducting solenoid coil providing access for the sample. Four types of magnets can basically be distinguished with regard to the bore size (in horizontal or vertical direction): narrow bore, wide bore, ultra wide bore and open bore. The design of superconducting magnets allows very high and homogeneous fields to be achieved. For imaging and spectroscopy applications the field strength for this kind of magnets ranges from 0.7 T to 23.5 T. General information about these kind of magnets and an overview on the design principles and theories is given by *Laukien and Tschopp* [1994].

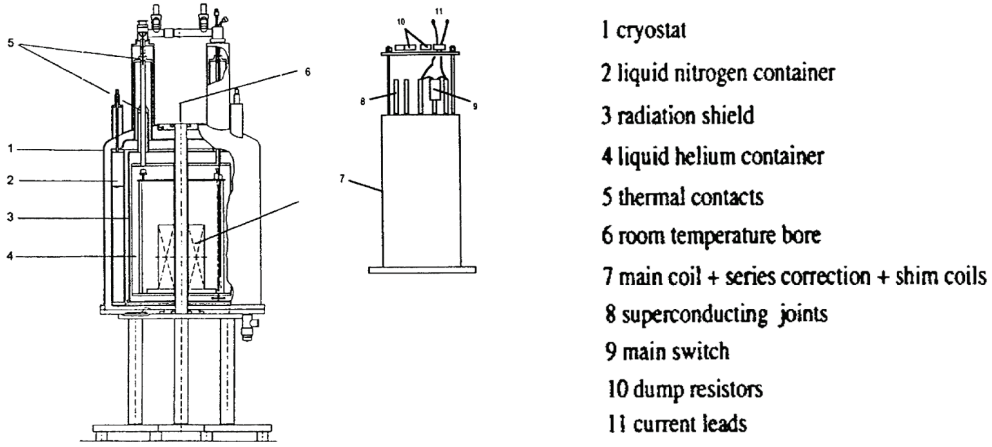

Figure 5. Superconducting MRI system (Reference: *Laukien and Tschopp* [1994])

Resistive electromagnets are rarely used in MR imaging in order to create B_0 due to the enormous cost of electricity required to maintain the field. The main advantage of these magnets is that they can be powered off easily. Permanent magnets provide a permanent magnetic field and offer a low cost alternative compared to the other magnet types. Depending on the material of the magnet field strengths up to 1 T can be achieved. Two concepts of permanent magnet arrangement can be distinguished: i) inside out, unilateral or single sided designs and ii) Halbach arrays. The concept of single sided or unilateral magnets first introduced in 1978 by the oil industry is advantageous over superconducting magnets in the way that these systems are portable in most cases and arbitrarily large samples can be studied. Further, no cryogenics need to be supplied on a regular basis which can dramatically reduce the maintenance costs of a system. Mainly two different classes of unilateral instruments exist. The first category refers to magnets with a sensitive spot above one face where three different geometries are differentiated. For this design $\boldsymbol{B_0}$ can be orientated either perpendicular (bare magnet) or parallel to the surface (C- and U-shaped) as shown in Figure 6. $\boldsymbol{B_0}$ and $\boldsymbol{B_1}$ created by the rf-pulse are orthogonal within some region where the gradient of $\boldsymbol{B_0}$ and the rf- bandwidth define a sensitive volume at a certain distance to the surface. The second class of instruments generates a point where $\boldsymbol{B_0}$ is locally homogenous, the "Sweet Spot" which allows a larger rf-bandwidth. The generated magnetic field gradients of the sweet-spot magnets are considerably reduced compared to the design of the first class what considerably limits diffusive attenuation. Besides these two

main designs the concept of inside-out MR is extensively employed in the petroleum industry, known as MR well-logging where the sensitive volume is located at a certain point from the tool. A detailed description of logging tools and their applications can be found in *Coates et al.* [1999]; *Kleinberg and Jackson* [2001] and *Sucre et al.* [2011]. The third concept of permanent magnets is the Halbach array named after their inventor Klaus Halbach. Permanent magnets are arranged in a circle following the filed lines of a homogenously magnet in the center. Various magnet arrangements exist where field strengths significantly stronger than the field of the individual bar magnets are achieved. Since Halbach setups are portable and self-shielded they are suitable for a variety of MR applications. The reader is referred to *Zhu and Howe* [2001] and *Raich and Blümler* [2004] for a comprehensive overview of Halbach arrays.

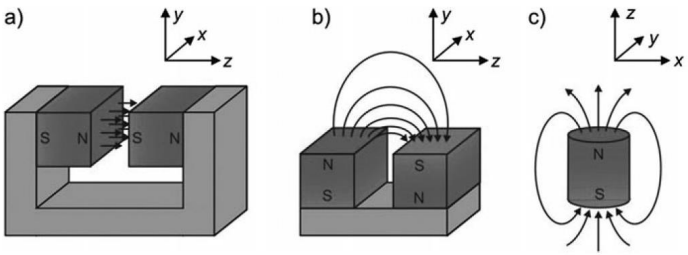

Figure 6. Common unilateral magnet designs: a) C-shaped geometry. The sample is placed in the homogeneous field inside the gap. b) U-shaped geometry. The sample is placed in the stray field above the gap. c) Bar magnet. The sample is placed in the stray field of the magnet (Reference: *Casanova* [2011]).

MR instruments

Various instruments have been employed in the context of this work: A 4.7 T high field superconducting ultra-wide bore scanner operating at 200 MHz ^{1}H resonance (Magnex Scientific, UK) equipped with a 300 mT/m gradient system and a "birdcage" type quadrature *rf*- resonator with an internal diameter of 100 mm and 100 mm length, operated by a Varian console was used for the investigations presented in Chapter 1 and 1.1 of this thesis. Additionally, a unilateral MR device, the **MO**bile **U**niversal **S**urface **E**xplorer (MR- MOUSE, Model PM-25, Magritek Ltd., Wellington/NZ) which is a portable but heavy (50 kg) open MR sensor, operated by a KEA^{2} spectrometer (Magritek Ltd., Wellington/NZ) and processed by the Prospa software package (Magritek Ltd., Aachen/Germany) was employed. The results of Chapter 2 and 3 are achieved by means of: i) A vertical bore MARAN DRX-HF imaging system (Oxford Instruments) equipped with 1 kW Techron gradient amplifiers (Typ 7782, AETechron, Elkhart, IN, USA), water cooled gradient coils and a custom-built rf-resonator with a resonance frequency of 8.5 MHz and an inner diameter of 45 mm ii) A vertical bore MARAN DRX spectrometer (Oxford Instruments Ltd., Oxford,

UK) equipped with an 25 W amplifier and a rf- probe with an inner diameter of 51 mm operating at 2.2 MHz resonance frequency. iii) A unilateral three magnet array with a copper shielded solenoid probe of 42 mm inner diameter and a sensitive spot of 24 x 15 x 10 mm^3 displaced 20 mm from the magnet surface and centered at a frequency of 2.25 MHz. The three magnet array was operated by means of a LapNMR console (Tecmag, Houston, USA), connected to a 250 W rf amplifier (TOMCO, Stepney, Australia) and a preamplifier (MITEQ, Hauppauge, USA). A detailed description of the NMR-MOUSE can be found in [*Blümich et al.*, 1998] and for the three magnet array the reader is referred to [*Marble et al.*, 2007] and [*García-Naranjo et al.*, 2010].

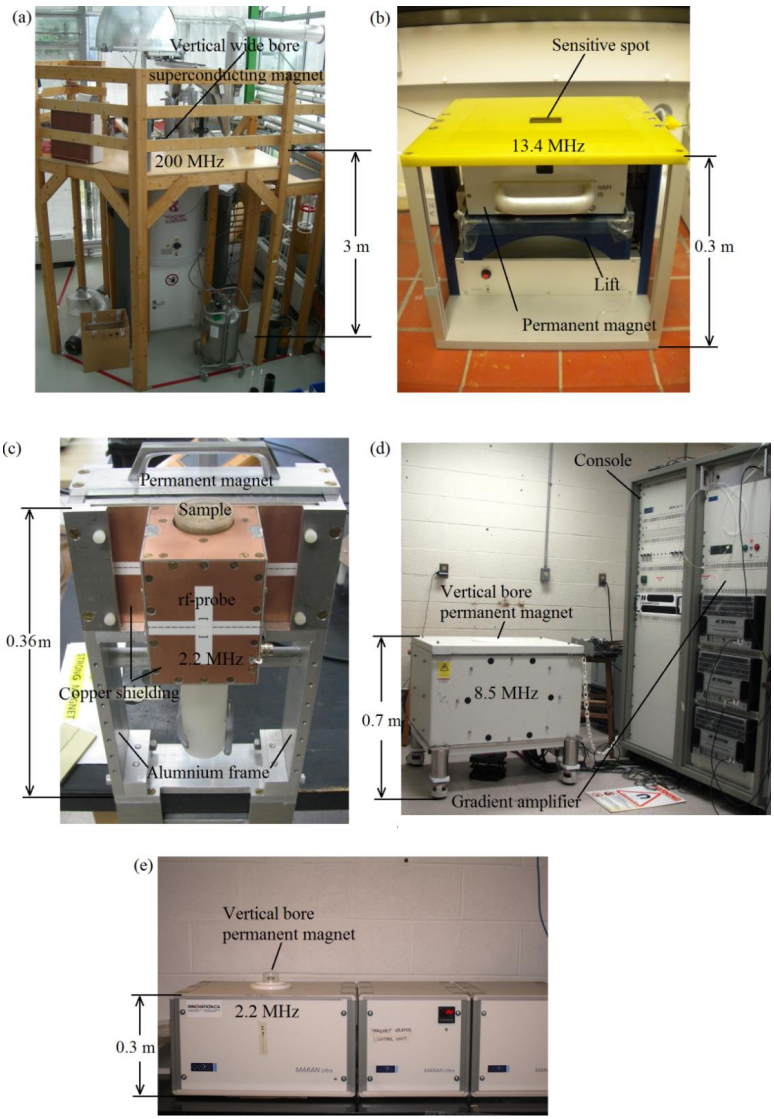

Figure 7. Overview of MR magnets used in the framework of this thesis. (a) 200 MHz wide bore superconducting scanner. (b) Portable unilateral MR magnet operating at 13.4 MHz (c) 2.2 MHz unilateral three magnet array developed at the MRI research center at the University of New Brunswick Canada. (d) 8.5 MHz system (e) Benchtop system operating at 2.2 MHz.

II. Vadose Zone Modeling Approaches

Darcy's law and the Richards equation

Vadose zone processes are essential for water and ecosystems since they are at the nexus of water and energy fluxes. In order to describe water movement in the vadose zone the Richards equation [*Richards*, 1931] is the most common modeling approach from sample to field scale. To solve the Richards equation the initial and boundary conditions, the hydraulic conductivity function $K(h)$ and the moisture retention characteristic $\theta(h)$ need to be defined. Classically, a soil water retention curve describes the amount of water retained in a soil under equilibrium at a certain matric potential. Among others [*Too et al.*, 2014], two parameterization methods with different modifications are commonly used: the van Genuchten [*van Genuchten*, 1980] and Brooks-Corey [*Brooks and Corey*, 1964] parameterization. The shape of the retention curve depends on the pore size distribution and the pore shape of the medium and is different for drainage and for imbibition due to hysteresis phenomena. This effect is mostly ignored for the majority of applications and the $\theta(h)$ relationship is deduced from the main drainage curve. Due to a couple of drawbacks of the Brooks-Corey model if applied in numerical simulations, the van Genuchten model is widely considered for soil water retention parameterization. It is further imperative to determine the unsaturated hydraulic conductivity $K(h)$ in order to solve the Richards equation. In contrast to the saturated hydraulic conductivity K_s, $K(h)$ varies strongly in time and with position what makes it complicated to determine. The majority of models calculate $K(h)$ by approximating the porous medium as a bundle of capillary tubes with laminar flow and interfering the pore size distribution from the water retention characteristic. Frequently, the Mualem-van Genuchten [*Mualem*, 1976; *van Genuchten*, 1980] approach is used to determine the relative $K(h)$. The one dimensional Richards' approximation considers: i) isothermal water flow and ii) uses an unsaturated hydraulic conductivity based on the capillary bundle model and is therefore not feasible to predict moisture as a function of depth accurately. Since the vadose zone is directly coupled to the atmosphere, many processes inside the soil are influenced by the net radiation flux. Heat can be transported by: i) conduction, the transmission of thermal energy from one particle to another ii) radiation, the transfer of thermal energy from a body to its surroundings by electromagnetic waves iii) convection, the transport of heat by a fluid in motion. If the latter is accompanied by a phase change the heat transfer can be increased considerably. In soils heat transport occurs predominantly by convection and conduction, with or without latent heat transport (phase change without change in temperature). Volumetric heat capacity and heat conduction are the thermal soil properties which govern the heat conduction. The meteorological conditions dominate the exchange at the soil surface which is driven by radiation, convection and conduction (with or without phase change). The thermal properties of a soil are closely linked to its water content, where flow of water and thermal energy entailing each other.

As shown in various studies in unsaturated soils mass and energy between liquid and vapor are frequently exchanged in the topmost layer [*Jassal et al.*, 2003; *Zeng*, 2013] what lead to a distinct dry layer below the surface of a bare soil where the profile below this layer remains wetter. Therefore, to compute vertical moisture profiles caused by evaporation the water flow needs to be coupled to the vapor and heat fluxes since the Richards' approach considers only water flow in the liquid phase and ignores the effects of vapor and therefore overestimates the moisture in the top layer as Figure 8 reveals [*Liu et al.*, 2005; *Novak*, 2010; *Sakai et al.*, 2009].

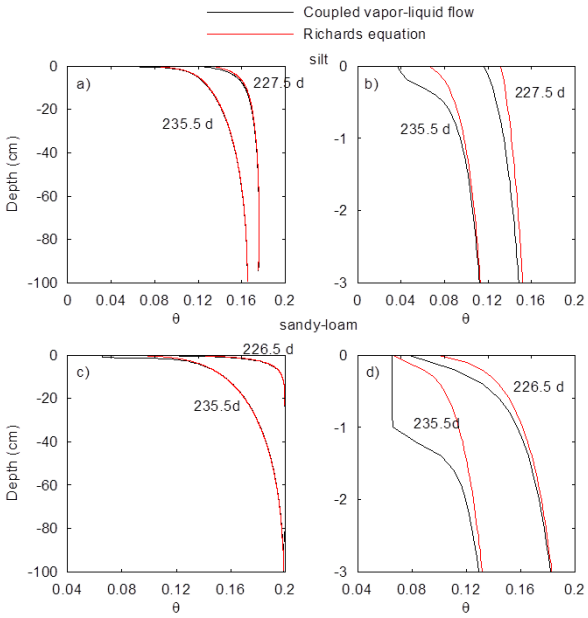

Figure 8. Simulated water content profiles using a non-isothermal vapor-water flow model (black line) and the Richards equation (red line) in the silt (top panels) and sandy-loam (bottom panels) soil. The right panels zoom in the top 3 cm of the soil profile (Courtesy of Prof. Jan Vanderborght, personal communication).

III. Results

Chapter I

Moisture profiles of the upper soil layer during evaporation monitored by NMR [1]

Abstract

Near surface soil moisture profiles contain important information about the evaporation process from a bare soil. In this study, we demonstrated that such profiles could be monitored non-invasively and with high spatial resolution using Nuclear Magnetic Resonance (NMR or Magnetic Resonance MR). Soil moisture profiles were measured in a column exposed to evaporation for a period of 67 days using a stationary Magnetic Resonance Imaging (MRI) high field scanner and a unilateral MR sensor. The column was packed with medium sand and initially saturated. Two distinct shapes of soil moisture profiles that are characteristic for stage I (evaporation rate is controlled by atmospheric demand) and stage II (evaporation rate is controlled by the porous medium) of the evaporation process were followed by both, MRI and unilateral MR. During stage I, an approximately uniform decrease of soil moisture over time was monitored, whereas during stage II, s-shaped moisture profiles developed which receded progressively into the soil column. These promising results and the specific design of the unilateral MR system make it very well suited for determining soil moisture profiles in the field.

[1] Adapted from: Merz, S., Pohlmeier, A., Vanderborght, J., van Dusschoten, D. and Vereecken, H. (2014) Moisture profiles of the upper soil layer during evaporation monitored by NMR. *Water Resources Research* 50(6), 5184-5195.

1. Introduction

Evaporation from bare soils is one key factor controlling water and energy exchange between the land surface and atmosphere [*Hanks et al.*, 1967; *Huxman et al.*, 2005; *Seager et al.*, 2007]. A large body of literature describes evaporation as a two stage process [*Coussot*, 2000; *Faure and Coussot*, 2010; *Lehmann et al.*, 2008; *Scherer*, 1990; *Schlünder*, 2004; *Shokri and Or*, 2011] with an initially high and often presumed constant evaporation rate (stage I or constant rate period (CRP)) close to that of an open water surface and primarily limited by the vapor pressure deficit between surface and air and the energy available to vaporize soil water. It should be noted that in some cases, e.g. when the soil surface dries out, also transfer through the air layer above the soil may become limiting [*Schlünder*, 2004; *Shahraeeni et al.*, 2012]. During stage I evaporative demand is supplied by liquid flow from the deeper soil towards to a secondary drying front, located at the soil surface [*Yiotis et al.*, 2001]. Stage I evaporation ends when the water potential at the soil surface falls below a critical threshold value. At this point of drying capillary flow ceases and the liquid films become detached from the surface (depinning) which marks the onset of stage II or falling rate period (FRP) [*Belhamri*, 2003; *Schlünder*, 2004]. The secondary drying front recedes inside the porous medium leading to a lower evaporation rate that mainly depends on porous medium properties such as pore size distribution. In Richards' equation only liquid flow is considered and vapor transport is neglected which leads to an overestimated moisture content in the topmost soil layer Therefore it is essential to take liquid water, vapor and heat flow into consideration as demonstrated by *Saito et al.* [2006].

A couple of methods exists that estimate soil evaporation on large scales from water content distributions in the surface layer [*Abtew and Melesse*, 2013; *Rossel et al.*, 2011; *Stafford*, 1988]. Since evaporation processes are sensitive to changes in the pore system and produce steep gradients of soil moisture in the shallow layer, non-invasive methods with high spatial resolution in the vertical direction are necessary for their investigation. *Shokri et al.* [2008] and *Shokri and Sahimi* [2012] investigated drying front dynamics by means of neutron radiography and synchrotron x-ray tomography using coarse sand in a Hele-Shaw cell and a small cylinder (12 mm height and 5 mm in diameter), respectively. These methods can, however, not be applied outdoors or directly in the field.

In recent years, Magnetic Resonance (MR) and Magnetic Resonance Imaging (MRI) have become versatile toolkits for soil and environmental research since they allow to study processes non-invasively [*Hall et al.*, 1997; *Nestle et al.*, 2002]. The main advantages are that these methods directly measure hydrogen and thus water as well as they provide versatile information, i.e. besides the mere water content also the local dynamics of the liquid in the pore system and the motion of tracers can be observed [*Pohlmeier et*

al., 2013]. MR and MRI are used for a broad range of applications to study various processes and materials, e.g. drying of mortar and cement [*Faure et al.*, 2012; *Valckenborg et al.*, 2001; *Van der Heijden et al.*, 2009], characterization of natural soils [*Haber-Pohlmeier et al.*, 2010; *Jaeger et al.*, 2009; *Pohlmeier et al.*, 2009; *Stingaciu et al.*, 2010; *Stingaciu et al.*, 2009] and rocks [*Song*, 2010], mapping of moisture content changes in porous media during drying, wetting or drainage [*Amin et al.*, 1993; *Balcom et al.*, 2003; *Deurer et al.*, 2002; *Faure et al.*, 2011; *Sněhota et al.*, 2010]. A comprehensive overview on MRI for investigation of mass transport in porous media is given by *Koptyug* [2012]. Driven by the fact that conventional MRI devices are immobile and therefore not suitable for in situ field measurements portable MR devices have been developed. One type is a unilateral, open U-shaped magnet which probes a sensitive volume at some distance away from its surface [*Casanova*, 2011]. Such devices use permanent magnets instead of an electromagnet, and are therefore not as heavy as the device presented by *Paetzold et al.* [1985].

The primary objective of the present work is to investigate whether the development of a shallow dry layer during stage II of evaporation can be observed with the unilateral MR sensor in the laboratory. Such a drying layer develops under dry soil conditions when the effective water diffusivity increases with decreasing volumetric water content due to an increasing contribution of vapor flow [*Assouline et al.*, 2013; *Han and Zhou*, 2013; *Keulen and Hillel*, 1974; *Shokri et al.*, 2008; *Shokri et al.*, 2010]. For this purpose we monitored the evolution of moisture profiles in the topmost layer of a laboratory column filled with natural sand by using 3D MRI and unilateral MR. Classical spin echo methods may suffer from short signal lifetimes, what is mostly the case for natural soils with an increasing pore surface/volume ratio and the presence of ferromagnetic or paramagnetic elements [*Foley et al.*, 1996; *Hall et al.*, 1997]. Therefore, as a secondary objective, we evaluated a pure phase encoding MRI sequence to determine water contents in soils with short signal lifetimes. As demonstrated by [*Muir and Balcom*, 2012; 2013] this has been proven to be an effective alternative method for fluid imaging in porous media with short signal lifetimes. We therefore compared a spin echo method to a pure phase encoding sequence.

2. Material and Methods

Porous Media

A Perspex column was packed (Figure 9) with medium sand (FH31 Quarzwerke Frechen) with a grain size distribution of: 1% (>0.71mm), 9% (0.5 – 0.71mm), 33% (0.36 – 0.5mm), 39% (0.25 – 0.36mm), 14% (0.18 – 0.25mm) and 4% (<0.18mm). The column consisted of a cylinder with 110 mm in height and 80 mm in diameter. Due to fixing reasons in the MRI tomograph a cylinder with 20 mm in height and 65 mm in diameter was connected to the top. The bottom was closed by a porous plate with pore size of 10 –

16 µm, a diameter of 60 mm and thickness of 5 mm (Robu GmbH, Hattert/Germany). After initial saturation the bottom was sealed, so evaporation could only took place at the column surface. Evaporation was followed over a period of 67 days. To calibrate the MRI signal on moisture a sealed reference tube with saturated sand packing was used. All characteristic parameters of the sample are summarized in Table 1. Air temperature, relative humidity and weight of the system were recorded hourly. The vapor pressure deficit (*vpd*) was computed as follows:

$$vpd\ [kPa] = e_s\ (1-(RH/100)) \tag{3.1.1}$$

where *RH* is the relative humidity and e_s is the saturation vapor pressure according to *Buck* [1981]:

$$e_s = F\ exp\ (17.27T/\ (T+237.3)) \tag{3.1.2}$$

where F = 0.611 kPa, and T is the temperature in °C. The temporal evolution of the *vpd* was used as a proxy for the temporal variation of the potential evaporation of the soil column.

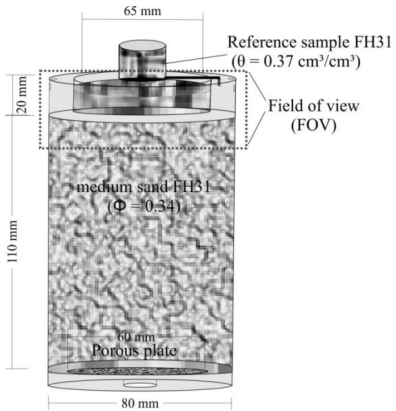

Figure 9. Scheme of the sand (FH31) column used for 200 MHz stationary MRI and 13.4 MHz unilateral NMR sensor measurements**.** Only the first 30 mm and 19.8 mm where monitored by the 200 MHz magnet and the 13.4 MHz unilateral NMR sensor, respectively.

Hydraulic Properties

The water retention curve of the sand was measured by using the HYPROP© - Laboratory evaporation method for the determination of water retention curves and unsaturated conductivity (UMS GmbH, Munich/Germany). The bulk density and the porosity of the sample were 1.69 g cm^{-3} and 0.36 cm^3 cm^{-3} re-

spectively. The measured water retention curve as well as the hydraulic parameters of the sand derived from fitting the van Genuchten [*van Genuchten*, 1980] function to the data, are shown in Figure 10 and presented in Table 1. It should be noted that the saturated hydraulic conductivity K_s could not be determined for this type of sand with the HYPROP© method and therefore, the value of *Sucre et al.* [2011] was used for computing the hydraulic conductivity function based on *Mualem* [1976].

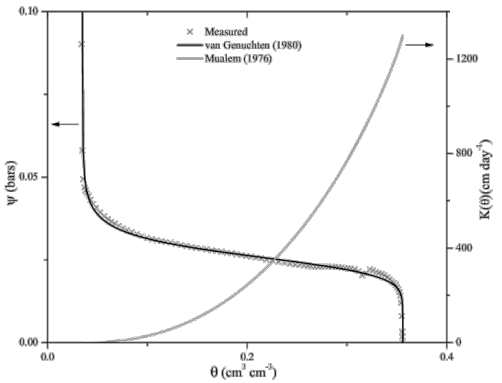

Figure 10. Water retention curve and hydraulic conductivity of the FH31sand material. The hydraulic conductivity was taken from Sucre et al. [2011]

Table 1. Van –Genuchten –Mualem parameters for the FH31 sand material.

Bulk density(g/cm^3)	Total porosity (θ_s)	θ_r	K_s(cm/day) †	α (cm^{-1})	l	n
1.69	0.34	0.035	1300	0.0385	0.5	8.5

† K_s taken from *Sucre et al.* [2011]

MR/MRI setup

For imaging we used a 4.7 Tesla (υ_0=200 MHz) high field vertical ultra-wide bore superconducting magnet (Magnex Scientific, UK), a 300 mT/m gradient system and a "birdcage" type quadrature *rf*- resonator with an internal diameter of 100 mm and 100 mm length, operated by a Varian console. During drying of the sample images were recorded at certain times by two different sequences. The parameters used for MRI are listed in Table 2.

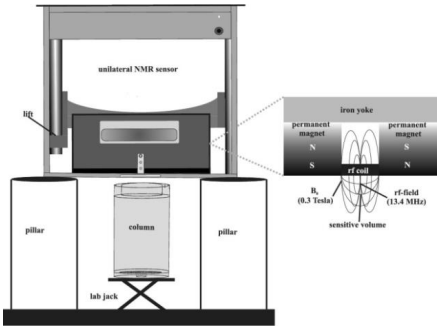

Figure 11. Scheme of the unilateral single sided MR sensor (NMR-MOUSE), mounted on a lift enabling to change the distance of the sensitive volume (40 mm x 40 mm x 0.14 mm) to or through an object, respectively. To investigate moisture profiles from the columns surface the sensor

Figure 12depicts the characteristics of each sequence. For detailed information on MRI/MR sequences the reader is referred to *Bernstein et al.* [2004]. The position of the column inside the scanner was kept identical for all measurements, including at least 1 cm of the reference tube and 4 cm of the column inside the field of view (Figure 9). The NMR-MOUSE (Model PM-25, Magritek Ltd., Wellington/NZ) is a portable open MR sensor, operated by a KEA^2 spectrometer (Magritek Ltd., Wellington/NZ) and processed by the Prospa software package (Magritek Ltd., Aachen/Germany). Based on the principles of "inside-out" MR, the device is equipped with permanent magnets in U-shaped configuration generating a gradient perpendicular to the surface. The MOUSE operates at a reference frequency of 13.4 MHz with a gradient of 7.5 T/m at a distance of 25 mm from the magnet surface with a resolution (thickness of the excited volume) of 0.1 mm. The sensitive volume is excited by an *rf*-coil that is placed 5 mm above the magnet, so that the effective maximum penetration depth is 18 mm. A profile is measured by moving the magnet by a lift, where the sensitive volume is moved through the upper 18mm of the sample. A sketch of the device is presented in Figure 11 whereas a detailed description of the system as well as the concept of single sided MR is given in *Blümich et al.* [1998] and *Casanova* [2011]. The unilaterally measured moisture profiles were recorded using 9 steps at a separation of 2 mm resulting in a maximum penetration depth of 18 mm. Table 2 lists all specific parameters for each sequence.

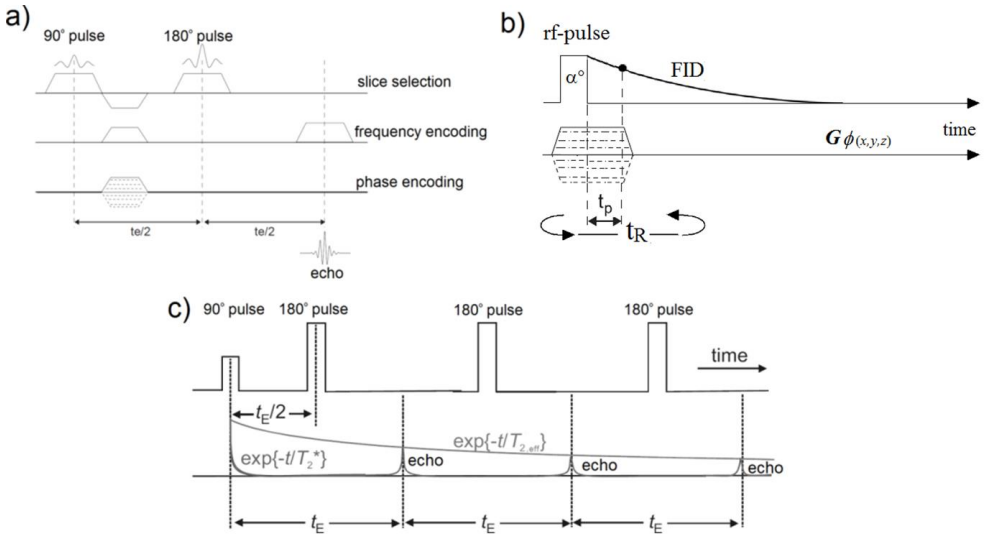

Figure 12. a) Spin Echo Multi Slice (SEMS). b) Single Point Imaging 3D (SPI3D). c) Carr-Purcell-Meiboom-Gill (CPMG) sequence. After *Bluemich* [2005] and *Varian* [2007].

Table 2. MR methods parameters. Spin echo multi slice (SEMS), Single point imaging 3D (SPI3D), Multi echo multi slice (MEMS) and Carr-Purcell-Meiboom-Gill (CPMG) sequences for MR and MRI measurements. t_R = repetition time; t_E = echo time; t_p = time after pulse; α = flip angle; *NE* = number of echoes; *NS* = number of scans; FOV = field of view; $T_{2,eff}$ = transverse (or spin-spin) relaxation time; M_0 = initial magnetization; MObile Universal Surface Explorer (MOUSE)

Sequence	t_R [s]	t_E [ms]	α (°)	*NE*	*NS*	FOV [mm]	Slices	Resolution (x,z,y) [mm]	Derived parame-ters	Measurement time [min]
SEMS	10	3.04	90	1	2	70x100	35	0.78x3.1x0.78	*M(te)*	*60*
SPI3D	0.01	0.05 (t_P)	6	-	2	120x150x120	-	3.75x2.34x3.75	*M(tp)*	*45*
MEMS	13	4	90	128	2	70x100	3	0.78x3x0.78	M_0, $T_{2,eff}$	*120*
CPMG (4.7T)	7	2.4	90	1536	1	-	-	-	M_0, $T_{2,eff}$	*0.05*
CPMG (MOUSE)	7	0.1	90	1536	128	-	10	40x0.14x40	M_0	*180*

Moisture profiles

MRI measurements were processed as follows:

First, the homogeneity of the sample was checked via T_2 mapping using a multi echo multi slice (MEMS) sequence [*Bernstein et al.*, 2004]. For each voxel, an exponential function was fitted to the echo train decay:

$$M(t) = M_0 \exp -[(NE^* t_E) / T_{2,app})] \quad (3.1.3)$$

where $M(t)$ is the signal amplitude, M_0 the initial magnetization, NE the number of echoes and $T_{2,app}$ the effective T_2 relaxation time. Secondly, for both, SPI and SEMS the investigated images were normalized on a saturated sample. From the normalized MRI signals and the water content of the reference sample, the moisture content for each voxel was calculated. This procedure is based on the assumption that the relation between the MRI signal and the water content is linear. To check this assumption, MRI signals of various calibration samples using the same sand with similar packing density and known water content were measured using identical parameters for SEMS and SPI3D as used for the sand column. Since the MRI signal was not homogeneous in a horizontal slice of the calibration samples, the average MRI signal of a region of interest in the calibration samples was plotted versus the gravimetric water content (Figure 13).

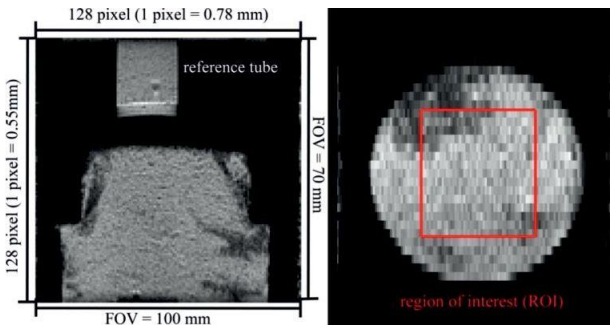

Figure 13. MRI images of the column. Left: Vertical slice of the column investigated by MRI using a SEMS sequence Right: Horizontal slice exhibiting the region of interest (ROI) equal to the area probed by the unilateral NMR sensor.

For the unilateral sensor the following procedure was used: The obtained CPMG echo decay train was fitted by an exponential decay function (Equation. 3.1.1). Since the reference sample that was used for MRI could not be measured with the unilateral MR sensor, a water sample (with volumetric water content

of 100%) was used as a reference. M_0 obtained from the soil sample was divided by M_{0ref} obtained from the water sample to determine the volumetric water content for each volume.

3. Results and Discussion

Drying rate and environmental conditions

The evaporation rate normalized on the vapor pressure deficit (vpd) over 67 days is shown in Figure 14 as an average over seven days. The evaporation rate was determined from the rate of mass loss recorded hourly by a digital balance. During stage I the normalized evaporation rate was approximately around 2 mm day^{-1} kPa^{-1} with a corresponding total mass loss of 153.6 g. After day 52 the rate dropped to 0.75 mm day^{-1} kPa and a continuous decrease in the normalized evaporation rate could be observed until day 67 with a corresponding mass loss of 25.6 g. During 67 days of drying the volumetric moisture content decreased from θs = 0.34 cm^3 cm^{-3} to 0.05 cm^3 cm^{-3} after 67 days yielding an overall mass loss of 179.2 g.

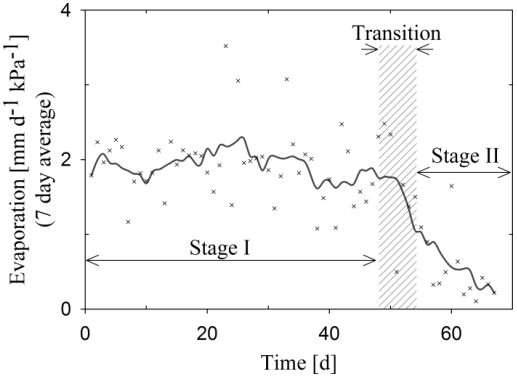

Figure 14. Evaporation rate normalized on vapor pressure deficit (cross) as an average over 7 days (grey line). Between day 48 and 55 the onset of stage II evaporation occurred.

MRI and unilateral moisture profiles

In Figure 15, MRI images of horizontal slices through the middle of the calibration tubes obtained by SEMS and SPI are presented. Despite the fact that the sand was homogeneously packed and mixed with water, the MRI signal was not homogeneous for these tubes. The signal heterogeneities might have been caused by layering effects due to the packing, what can led either to variations in water content or in signal because of shorter T_2 times. However, these signal heterogeneities were averaged out when calculating the water content profiles. Between θ = 0.05 cm^3 cm^{-3} and θ = 0.4 cm^3 cm^{-3} a linear relationship be-

tween signal intensity and volumetric water content was assumed to derive the moisture content from the MRI signal intensity.

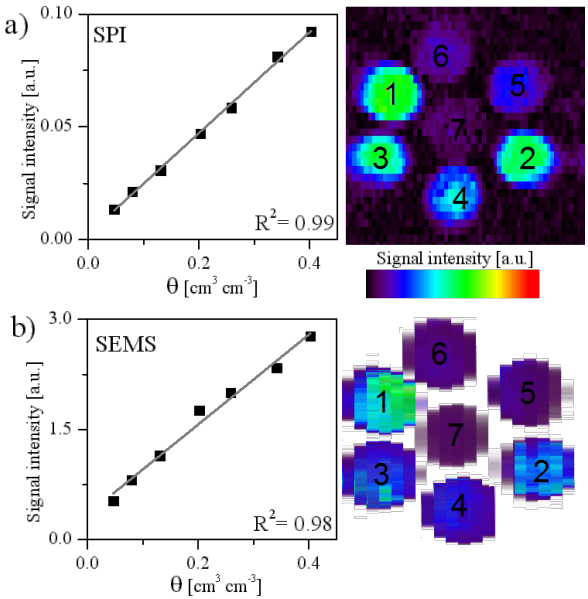

Figure 15. Calibration relations between MRI signal and volumetric water content(left) obtained with SPI3D (a) and SEMS (b), where the grey lines are linear fits. Right images: MRI cross section through the calibration phantom for Single point imaging (top) and Spin echo multi slice (bottom), where each pot is different in water content. (θ [mm^3 mm^{-3}] 1: 0.4, 2: 0.34, 3: 0.26, 4: 0.2, 5: 0.13, 6: 0.08, 7: 0.05)

Layering effects due to packing as well as cracks can influence evaporation in several ways, therefore we checked for heterogeneities using a MEMS sequence. Figure 16 exhibits no significant heterogeneous T_2 patterns for the used column, but larger pore sizes (longer T_2) were observed near the walls where packing was less dense. The drying stages during the experiment could be linked to the shape of the vertical soil moisture profiles that were derived from MRI measurements. Figure 17 shows vertical soil moisture profiles that were monitored using MRI and the unilateral MR sensor. During stage I, the moisture content in the upper soil layer was virtually homogeneously distributed and the evaporation front is located at the soil surface.

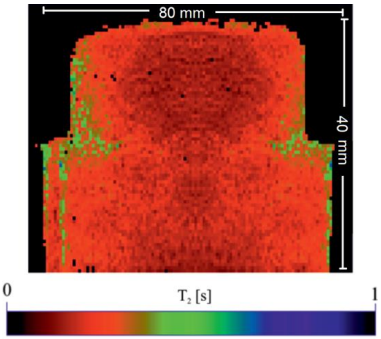

Figure 16. Distribution map of effective transverse relaxation times $T_{2,eff}$ obtained by fitting Equation 3.1.3 to images monitored by MEMS for a vertical cross section of the saturated column.

After reaching a critical water content at the surface (0.035 cm^3 cm^{-3} for the used column at day 50), the evaporation front receded into the soil forming an increasingly thick dry surface layer. Water transport was now controlled by the vapor pressure gradient and evaporation flux proceeded via vapor transport. With increasing thickness of the dry layer the overall evaporation rate decreased. The drop in the normalized evaporation rate coincided with the time where a receding secondary evaporation front was observed in the moisture profiles. Onwards drying, the drying rate decreased and the secondary evaporation front receded deeper into the soil, with a final depth of 20 mm at day 67. The moisture content profiles obtained by SEMS (dotted lines in Figure 17) exhibited a nearly homogenous saturated upper part of the initially saturated column which are in good agreement with the gravimetrical determination. With increasing drying the profiles investigated by SEMS showed a homogenous drying behavior during stage I. The development of a steep moisture gradient in the upper 1 cm after a certain time was caused by a decrease in the capillary film which finally ceased when the critical point of drying was reached. This gradient was still detectable by SEMS after the onset of stage II but now attached to the secondary evaporation front inside the soil. Comparing the SEMS profiles to those investigated by SPI (dashed-dotted lines in Figure 17) an identical shape for both drying stages can be found. The most obvious difference between SEMS and SPI was that single point imaging exhibited higher moisture content for all profiles during both stages. These may be related to a baseline offset on the SPI measurement what led to higher moisture content. The assumption of a baseline offset was substantiated by the fact that for both, SEMS and SPI, the investigated profiles were identical in shape for stage I and II. The constant baseline offset led to a small relative deviation at high water content and a large deviation at low water content. However, both, the spin echo as well as the single point imaging sequence enabled to follow the drying process of the column down to the residual water content. For the unilateral MR (dashed line in Figure 17) it should be

noted that only the first 18 mm were monitored. The moisture profiles investigated by the sensor revealed similar homogenous drying patterns with an increasing gradient in the upper part as monitored by SEMS and SPI. Nevertheless, the investigated moisture content seems to be lower compared to SEMS and SPI. This is a consequence of the open geometry of the unilateral MR sensor as well as the thickness of the excited slice which is only 0.14 mm.

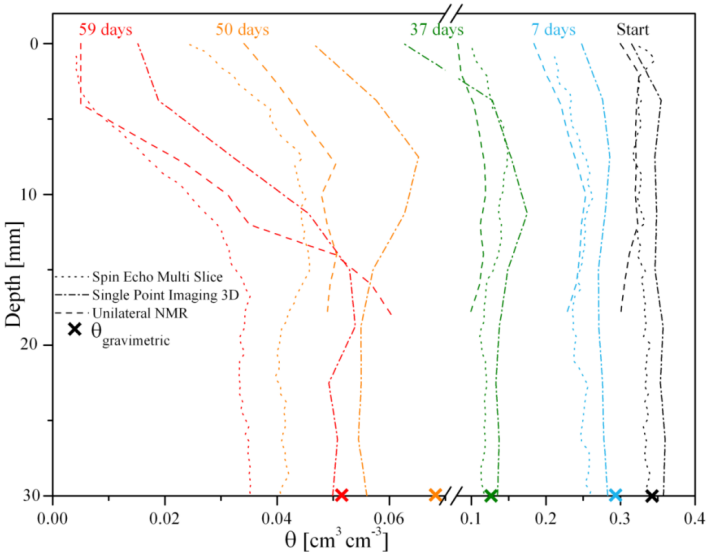

Figure 17. Moisture profiles over time monitored by SEMS, SPI3D and the unilateral NMR for the topmost 30 mm (SEMS and SPI3D) or 18 mm (Unilateral NMR) of the column (soil surface=0) The profiles should be read from right to left starting with the saturated condition (start) on the right. The gravimetric total water contents are plotted as crosses on the abscissa.

Relaxation analysis

Another suitable approach for following a drying process of porous media is to monitor the relaxation decay over time by using a CPMG sequence. As expected, the amplitudes of the decay curves, obtained from fitting Equation 3.1.3 to the data, are directly proportional to the proton density in the measured volume and, in turn, the moisture content. The open geometry of the sensor is sensitive to environmental radiofrequency noise, where the signal to noise ratio (SNR) decreases rapidly with decreasing moisture content. The relaxation times measured with the unilateral MR sensor are strongly controlled by diffusion of H_2O in the external 7.5 T/m gradient [*Casanova*, 2011]. Therefore, we additionally investigated the T_2 distribution in the homogeneous magnetic field of the MRI scanner over 67 days in order to obtain infor-

mation about the range of pores that remained saturated or that were partially filled with water (Figure 18). The first distribution curve reflects the condition after 4 days of drying, what in fact can be assumed as almost saturated ($\theta = 0.31$ cm^3 cm^{-3}). The distribution functions of the FH31 sand can be described as a main mode with T_2 around 250 ms with a broad shoulder at faster relaxation times (smaller pores) for the saturated conditions which broadens further at lower water contents.

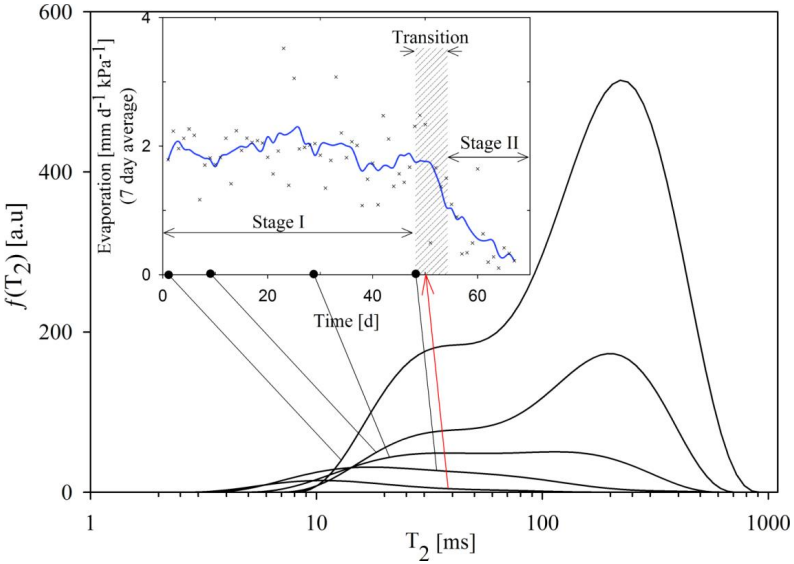

Figure 18. T_2 distribution functions for the upper 30 mm of the column over 67 days of drying. The inset shows the evaporation rate normalized on vapor pressure deficit as an average over 7 days, where the red arrow indicates the peak shift in the T_2 distribution coincided with the drop in the evaporation rate at the transition from stage I to stage II.

During the drying period the logarithmic mean relaxation time $T_{2,av}$ shifted from 150 ms for the state at $\theta = 0.31$ cm^3 cm^{-3} after 4 days of drying to 14 ms after 67 days and the total area of the main peak decreases with time. At day 22 a slight peak shift to 160 ms was observed followed by a constant decrease in amplitude until day 52 where the peak height has decayed to almost zero. Regarding the normalized evaporation rate, the vanishing of the slow mode occurred simultaneously with a drop in the rate at the end of stage I. Now, the maximum of the distribution function is located at 20 ms and shifted further with decreasing moisture to 10 ms after 67 days. The assignment of T_2 relaxation modes to pore sizes is not straightforward, since T_2 is prone for diffusional acceleration in internal gradients [*Mitchell et al.*, 2010], especially at high magnetic fields. However, the fast mode persisted below the critical water content at the

transition between stage I and stage II where continuous water films vanish. Therefore, the most likely interpretation is the assignment of the fast mode as water at the contact points between the grains and in the corners of the rough grain surface, where it is strongly retained by capillary forces. At higher water contents water in such areas will be in fast diffusive exchange with bulk water, and a differentiation from effects due to motion in internal gradients is not possible. Furthermore, bimodality can be due to chemical heterogeneity of surface sites of this natural product cannot be excluded, since *Grunewald and Knight* [2011] report on monomodal, slow relaxation in very pure quartz sand. On the other hand, bimodal T_2 distributions of sand packing have been reported in the literature and reproduced by numerical simulation using random walk based on pore space structure derived from analysis of μ-CT scans, see *Talabi et al.* [2009]. We conclude that the interpretation of the nature of the T_2 distribution functions in unsaturated natural sands requires further investigation, which is beyond the scope of this paper.

4. Summary and Conclusions

The aim of this study was to investigate moisture content changes in the topmost soil layer during evaporation by means of MR imaging and a unilateral MR sensor for assessing its later usage for field measurements. We evaporated an initially saturated sand column in the laboratory over a period of 67 days. Due to changing environmental conditions in the laboratory we normalized the evaporation rate on the vapor pressure deficit where a transition region from stage I to stage II could precisely be determined. The shape of the soil moisture profiles, monitored by MRI using a spin echo as well as a single point imaging sequence and a unilateral MR sensor, may also be used as an additional criterion to distinguish between stage I and stage II evaporation. The observed measurement differences between SEMS and SPI3D are small. Portable MR measurements are feasible for $\theta > 0.03$ cm^3 cm^{-3} for the used sand and are in good agreement with the MRI profiles. Therefore, it can be concluded that each method is appropriate to study the drying stages and the onset of the development of a secondary drying front in a model soil. Finally, additional information about the shift between stage I and stage II could be obtained from high field relaxation measurements. For the saturated sand, an approximately bimodal distribution of relaxation times was observed. During stage I the peak of the long relaxation times shifted slightly from 250 ms to 160 ms, decreased and finally vanished at the end of stage I. From this time only the peak representing the fast relaxation times remained during stage II. Based on the fact that the relaxation mechanisms of transverse relaxation at high field MR are not yet fully clear, one may assume that the rapid mode which remains during stage-II evaporation is due to insulated thin water films and water in pores corners. However, this will be one subject to further investigations.

Chapter II

Transition of Stage I to Stage II evaporation regime in the topmost soil: High-resolution MR imaging, profiling and numerical simulation [2]

Abstract

Bare soils are natural porous media where moisture and transport properties may change considerably. Under very dry conditions, it is predicted that capillary continuity from deeper soil layers to the surface ceases and evaporation decreases drastically because it is only sustained by vapor transport through an increasing dry surface layer (stage II). According to Chapter I, we firstly confirm this effect by investigating the drying of a lab-scale sand column using various MRI sequences as well as a unilateral MR sensor (NMR-MOUSE). Proving the convenience of the unilateral sensor, we take a step forward by monitoring moisture development of a natural soil under controlled ambient conditions. Finally, the experimental results clearly validate the prediction of a coupled water, vapor and heat flow model regarding the onset of stage II evaporation and the subsequent receding secondary evaporation front.

[2] Adapted from: Merz, S., Pohlmeier, A., Vanderborght, J., van Dusschoten, D. and Vereecken, H. (2015) Transition of stage I to stage II evaporation regime in the topmost soil: High-resolution MR imaging, profiling and numerical simulation. *Microporous and Mesoporous Materials*, *205*(0), 3-6.

1. Introduction

Water exchange between non-vegetated ground surfaces and the atmosphere is one significant component of the earth´s water cycle. Since soil can be considered as a porous medium, the drying process can be commonly divided into two distinct stages [*Or et al.*, 2013]. The initial period (stage I) is predominantly controlled by the vapor pressure deficit (vpd) between soil surface and the surface boundary layer. During stage I (also referred to as constant rate period) the evaporation rate is relatively constant and mainly equal to the evaporative loss from a free water surface. A decreasing water potential at the surface below a critical threshold marks the onset of stage II where capillary flow through connected liquid pathways ceases. Now, a secondary evaporation front migrates into the porous medium and an increasing dry surface layer develops. During stage II, water evaporates within the soil matrix and the vapor transport through the dry layer becomes the delimiting factor for the evaporation rate. The transition from stage I to stage II is further attended by an increase of soil surface temperature due to the reduction of the evaporative cooling effect [*Monteith*, 1981]. Experimental investigation of such shallow water depletion layers requires non-invasive, high-resolution methods like Magnetic Resonance Imaging (MRI) and one-dimensional, unilateral MR for field studies. Both have become versatile toolkits for environmental research and soil science during the last decade [*Blümich et al.*, 2014; *Nestle et al.*, 2002; *Pohlmeier et al.*, 2013; *Sucre et al.*, 2011]. Moreover, besides the mere water content MR-relaxometry also provides information on the local dynamics of water in the porous system [*Blümich et al.*, 2014].

2. Experimental

Since the drying of a sand column during evaporation using different MR and MRI sequences, has already been presented in Chapter I, this Chapter focuses on unilateral MR measurements performed on an evaporating natural soil(silt loam). The unilateral sensor (PM 25 NMR MOUSE, Magritek, New Zealand) was operated by a KEA^2 (Magritek, New Zealand) spectrometer. To assess our measurements we numerically simulated soil moisture profile development using a coupled water, vapor and heat flow model based on [*Saito et al.*, 2006] .

3. Unilateral MR measurements on natural soil

The measurements were performed using the mobile unilateral MR sensor. An insulated (Armaflex) Perspex box (626 mm x 477 mm x 180 mm (L x W x H)) placed on a digital balance and mounted on a lifting jack was equipped with two drainage pipes at the bottom (10 mm diameter) and connected to the outside of the box (Figure 1b). 21.14 kg of ground quartz silt (Millisil W3, Quarzwerke Frechen, Germa-

ny) were filled up to a height of 42 mm to cover the pipes. After the system was saturated with deionized water a temperature logger was placed in the middle of the box (to record bottom temperature) and 46.2 kg of silt loam were added.

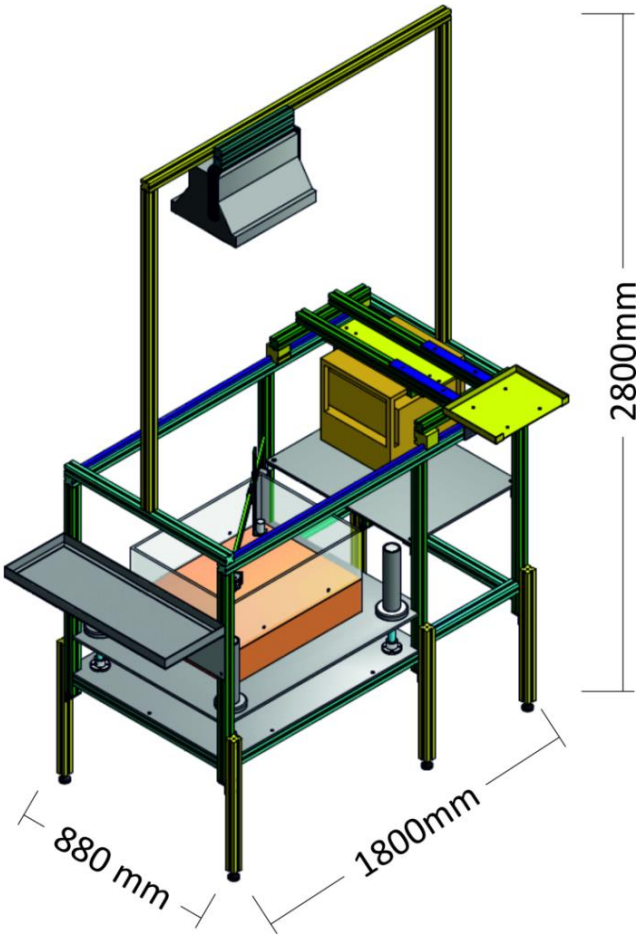

Figure 19. Setup consisting of a mercury arc lamp to ensure a defined constant radiation, the soil box filled with a silt loam and the unilateral NMR sensor mounted on a slide over the top of the soil surface allowing horizontal and vertical adjustment. The soil box was placed on a balance, both adjustable by means of a lifting jack.

The silt loam was originated from one of our test sites (Selhausen, Germany) and consisted of 14% sand, 70% silt and 15% clay. In order to determine the relative evaporation the weight of a vessel (diameter 135 mm) with a free water surface was recorded simultaneously under identical ambient conditions. A mercury arc lamp was placed at 1440 mm above the soil surface achieving constant incoming shortwave and longwave radiation of 20 W/m^2 and 470 W/m^2, respectively (determined by a net radiometer NR01, Hukseflux Thermal Sensors, Delft, The Netherlands). Further, we monitored the soil surface temperature by means of an Optris© CT LT02 infrared sensor (Optris GmbH Berlin, Germany) placed 250 mm above the soil surface (effective diameter 500 mm). The unilateral MR sensor was mounted on a slide over the top of the soil surface, allowing vertical and horizontal adjustment (Figure 1b) to retain an identical position for each measurement. The moisture content during drying was monitored by repetitive CPMG measurements at 10 various depths, where each step was separated by 1.98 mm down to a maximum penetration depth of 19.8 mm.

4. Results and discussion

The drying was monitored over a period of 71 days where the overall gravimetric water content of the box decreased from 0.5 $cm^3\ cm^{-3}$ to 0.19 $cm^3\ cm^{-3}$. Figure 3 shows the relative evaporation rate over time where around day 35 a drop in the relative evaporation rate from 0.8 to 0.2 marked the transition to stage II evaporation, coincided with an increase of the surface temperature from 19°C to 23°C. The prediction of the coupled model approach and the corresponding development of vertical soil moisture profiles for the upper 20 mm are presented in Figures 4a and 4b. During stage I a strong heterogeneous moisture distribution could be found what was due to the packing of the box. The moisture content at the surface decreased rapidly in the beginning but nevertheless, the secondary evaporation front appeared around day 35 (Figure 4 green profile) what marked the onset of stage II. However, the moisture content of the topmost layer decreased down to $<0.03\ cm^3\ cm^{-3}$ after 51 days. A comparison with the forward simulation using the coupled water, vapor and heat flow model shows that principally the onset of stage II and the subsequent receding of the secondary drying front are experimentally confirmed. However, the model predicts a later onset of the transition and weaker moisture gradients. Reasons for this are probably the neglecting of soil heterogeneity and the fact that soil physical parameters were determined independently.

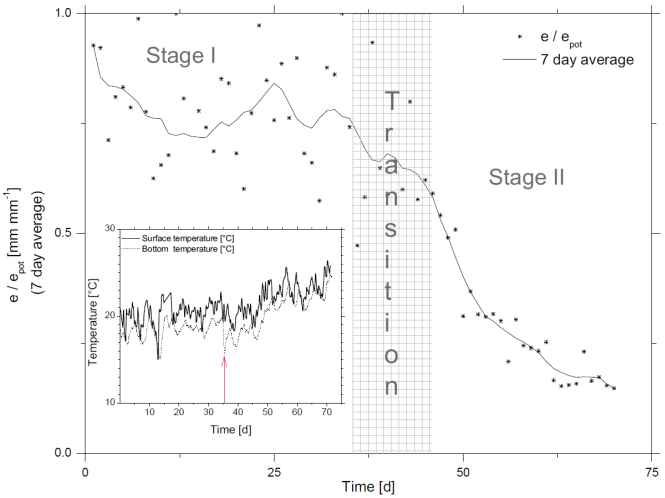

Figure 20. Relative evaporation over time averaged over 7 days**.** The soil surface temperature (black straight line) and the temperature at the bottom (dashed line) are shown as an excerpt. The red arrow marks the transition to stage II evaporation.

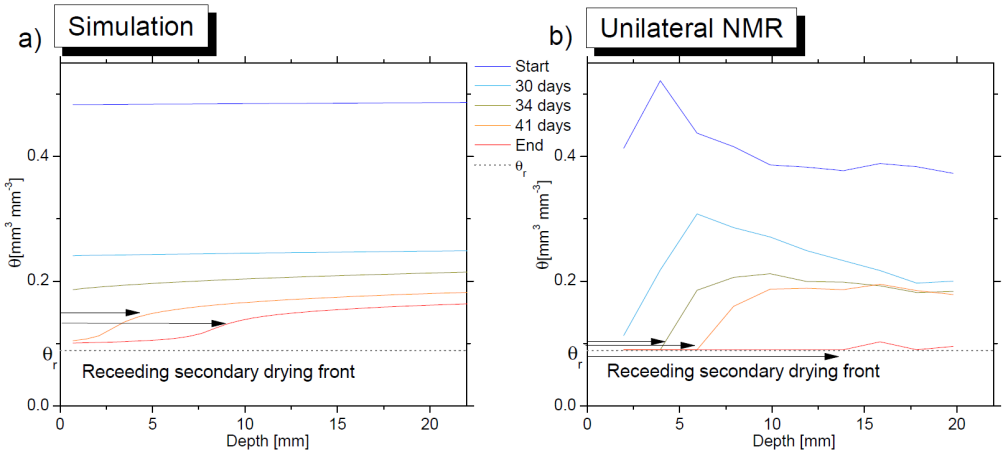

Figure 21. Numerically simulated vertical moisture profiles using a coupled water, vapor and heat flow model. b) Moisture profiles monitored by means of unilateral NMR for 5 time points. The arrows indicate the receding secondary drying front .

5. Conclusion

The isothermal drying of a silt loam was investigated using a unilateral MR sensor. Two distinct stages of drying could be identified which were directly linked to a change in the relative evaporation rate. By using the Unilateral MR sensor the drying process could be studied down to an effective moisture content of 0.03 cm^3 cm^{-3}. The higher gravimetric residual water content of 0.09 cm^3 cm^{-3} for the Selhausen soil was due to the larger amount of clay bound water. This water relaxed very rapidly and was therefore not detectable with the current setup and parameters. Our findings compared to a coupled water, vapor and heat flow approach where in good agreement with respect to the prediction of the onset of stage II evaporation. For stage I the profiles show a larger deviation over time and became biased regarding a developing moisture gradient in the upper layer. The constant deviation in moisture was due to the fact that the model assumes a perfect homogenous medium. The natural soil exhibited a strong heterogeneity and fast drying surface but, nevertheless, stage II evaporation originated firstly around day 35. Compared to the numerically predicted profiles the heterogeneity of the soil led to deviations in moisture content and shape during stage I. However, the onset of stage II (around day 35) as well as the depth of the secondary evaporation front of 5mm after 40 days is satisfactorily predicted by the coupled model. In summary, it was shown that the unilateral MR is feasible to monitor moisture changes until the onset of stage II in the topmost layer of a natural soil.

Chapter III

Drying of a natural soil under evaporative conditions: A comparison of different magnetic resonance methods [3]

Abstract

Soils are highly complex and heterogeneous porous materials, and thus measuring water distribution non-invasively with high accuracy and adequate spatial resolution still remains challenging. The first few centimeters of a soil surface control the vapor flux to the atmosphere justifying the need for high spatial resolution measurements of moisture content. The objective of this study is to compare and assess the feasibility of various high resolution MR methods in order to characterize an unsaturated porous system. We employed: .i) a Spin-Echo (SE), ii) three types of Single Point Imaging (SPI) and iii) a unilateral three magnet array in order to monitor T_1 and $T_{2,app}$ relaxation time spectra and the effective moisture saturation (Θ_{MR}) of a silt loam under progressing desaturation with focus on an emerging unsaturated surface layer, which is predicted by theory. During the first stage of drying where evaporation occurred at the soil surface, all methods showed homogeneously distributed moisture. A decreasing Θ_{MR} and a shift in the T_1 and $T_{2,app}$ relaxation time spectra to shorter values indicated the commencement of stage 2 evaporation coincided with an increasing unsaturated layer. At low water contents, the most suitable method to determine the extent of a desaturated surface zone with high accuracy was found to be Single Point Ramped Imaging with T_1 Enhancement (SPRITE). As a simple and low cost device the unilateral three magnet array was feasible to monitor the drying process until the dry surface layer developed.

[3]Adapted from: Merz, S., A. Pohlmeier, B. J. Balcom, R. Enjilela, and H. Vereecken (2015), Drying of a Natural Soil Under Evaporative Conditions: A Comparison of Different Magnetic Resonance Methods, *Appl Magn Reson*, *47*(2), 121-138.

1. Introduction

Three main processes are associated with water in porous materials: a) absorption, the entry of water into the material, b) migration, the movement of water within the material and c) desorption, the loss of water to the surroundings [*Hall and Hoff*, 2011]. On bare soil surfaces desorption occurs by evaporation and is one of the major components controlling the energy balance and fluxes between pedosphere and the atmosphere. Evaporation describes the process whereby a liquid, e.g. water, is converted from its liquid phase to the vapor phase and removed from the evaporating surface, e.g. from free or open water surfaces such as lakes and ponds, from wet vegetation surfaces or from bare soil surfaces. Since soils consist of solid skeletal material and voids which are typically filled by air or a liquid, they are porous media where drying processes are typically divided into two characteristic stages [*Or et al.*, 2013; *Scherer*, 1990; *Schlünder*, 2004]. During an initial stage often referred to as stage I ($S1$) or constant rate period, the evaporative demand is supplied by a constant liquid flow from the inside of the medium to the evaporating surface where the phase transition to vapor occurs. Once the liquid continuity to the surface ceases, the onset of stage II evaporation ($S2$) or falling rate period is marked. Now, the phase transition occurs inside the soil causing an extending unsaturated subsurface layer. A detailed understanding of these processes on the laboratory scale is crucial for the improvement of numerical models because these small scale processes manifest themselves on large scales [*Faure and Coussot*, 2010; *Or et al.*, 2013]. MR, MRI and unilateral MR have proven their potential to monitor such processes in high resolution [*Faure and Coussot*, 2010; *Keita et al.*, 2013; *Merz et al.*, 2014], but nevertheless there are still difficulties and limitations encountered in soil-water MRI. Due to the inherent fast relaxation times in natural soils with higher clay content and paramagnetic impurities, MRI images can be distorted or large fractions of water are invisible [*Amin et al.*, 1997; *Haber-Pohlmeier et al.*, 2014; *Hall et al.*, 1997; *Stingaciu et al.*, 2009]. These problems are exacerbated with decreasing moisture since relaxation times decrease, coinciding with a decreasing signal to noise (SNR) ratio [*Jaeger et al.*, 2009]. While a preceding work principally compared the convenience of different MRI methods for fluid quantifications in rocks [*Muir and Balcom*, 2013], the objective of this work is to compare the effectiveness of different MR methods and a unilateral three magnet array in an unsaturated unconsolidated porous system in regard of: i) the general ability to quantify moisture ii) the reliability of measured relaxation times iii) the spatial distribution of moisture and relaxation times and iv) the adjustability of the measurement parameters. We thereby particularly focus on the increasing dry surface layer during $S2$ evaporation as predicted by theory. For this purpose MR measurements were performed in the laboratory using a column filled with silt loam as the sample. Evaporation in a climate chamber under constant ambient conditions occurred over 15 days with a measurement focus on moisture saturation and T_1 and $T_{2,app}$ relaxation time spectra.

2. MR/MRI Principles

Assuming a two phase model in the fast diffusion limit [*Dunn et al.*, 2002], the T_1 relaxation time is described by

$$1/T_1 = 1/T_{1,\,bulk} + 1/T_{1,\,surface} \tag{3.3.1}$$

where $T_{1,\,bulk}$ is the bulk fluid relaxation rate and $T_{1,\,surface}$ the relaxation time of the fluid resulting from pore surface relaxation.

In porous media the signal decay is caused by four types of independent relaxation processes [*Kleinberg*, 1999]:

$$1/T_2^* = 1/T_{2,app} + 1/T_{2,\,inhomogeneous} \tag{3.3.2}$$

where $1/T_{2,\,inhomogeneous}$ describes dephasing due to static inhomogeneities of the magnetic field. Stationary spins in an inhomogeneous magnetic field are exposed to different $\boldsymbol{B_0}$ fields which gives rise to dephasing as described by the second term of Equation 3.3.2. This effect can be compensated for by a Hahn echo [*Hahn*, 1950] or a Carr-Purcell-Meiboom-Gill (CPMG) echo train [*Meiboom and Gill*, 1958] which is the standard technique for measuring the apparent transverse relaxation time, $T_{2,app}$, which is described as:

$$1/T_{2,app} = 1/T_{2,\,bulk} + 1/T_{2,\,surface} + 1/T_{2,\,diffusion.} \tag{3.3.3}$$

$1/T_{2,bulk}$ is the relaxation rate in a uniform field for bulk solutions, usually in a range of 3 *s* for pure water. The term "apparent" refers to the fact that the observable rate depends on the choice of the experimental parameter t_E, which controls the third term on the right hand side of Equation 3.3.3 [*Pomerantz et al.*, 2008]. The second term on the right hand side of Equation 3.3.3 is due to surface relaxation:

$$1/T_{2,\,surface} = \rho_2 (\mathrm{S/V})_{\mathrm{pore}} \tag{3.3.4a}$$

This term provides the link between pore size and relaxation times by describing the surface relaxation occurring at the fluid-solid interface, where ρ_2 is the T_2 surface relaxivity parameter which varies with mineralogy and describes the capacity of a solid surface to enhance relaxation. $(S/V)_{pore}$ is the ratio of pore surface to fluid volume and can also be expressed as β/r, where r is the pore radius and β is a shape factor for simple pore geometries (1 = planar, 2 = cylindrical, 3 = spherical).The signal loss due to diffusion in magnetic field gradients in the short diffusion time regime is described by [*Mitchell et al.*, 2010]:

$$1/T_{2,\,diffusion} = D/12(\gamma G t_E)^2 \tag{3.3.4b}$$

where D is the molecular diffusion coefficient, G the magnetic field gradient strength and t_E the inter-echo spacing.

If an rf- field is turned on in the presence of $\boldsymbol{B_0}$ all spins in the probed volume undergo a forced precession. To achieve a spatially encoded signal, additional magnetic field gradients are applied simultaneously with, or after, the rf-pulses. One distinguishes between slice selective, frequency encoding and phase encoding gradients, which can be used in various combinations, in a pulse sequence [*Bernstein et al.*, 2004; *Callaghan*, 1993; *Chang et al.*, 1999; *Nishimura*, 1996]. One category of methods to achieve spatial encoding is pure phase encoding Single Point Imaging (SPI) where three G_{phase} gradients are imposed during or immediately after the rf excitation pulse and one or multiple data points are acquired at a fixed time after excitation.

Spin Echo Single Point Imaging (SE-SPI) for Moisture Profiles and $T_{2,app}$ relaxation time spectrum

To achieve both spatially resolved $T_{2,app}$, and moisture content, a bulk measurement is performed with spatial encoding added to the signal phase by a stepped gradient pulse between the 90° and the first 180° refocusing pulse after $t_{E,0}$ /2 (Figure 22). Afterwards a regular CPMG echo train follows [*Li et al.*, 2009; *Petrov et al.*, 2011]. The image signal intensity is given by

$$M(t,\boldsymbol{r}) = M(0,\boldsymbol{r})\ exp\ -\{t_{E,0}/T_{2,app}\}\ exp\text{-}\{(n_E\text{-}1)\ (t_E/T_{2,app})\} \tag{3.3.5}$$

Where $t = t_{E,0} + (n_E - 1)t_E$. $t_{E,0}$ represents the echo time of the first pulse interval. t_E is the echo time of the following echoes and n_E is the total number of echoes. The application of a Fourier transformation to the raw data leads to a series of $T_{2,app}$ -weighted profiles [*Gallagher et al.*, 2008]. The data is then further processed by applying an inverse Laplace yielding a spatially resolved $T_{2,app}$ relaxation time spectrum.

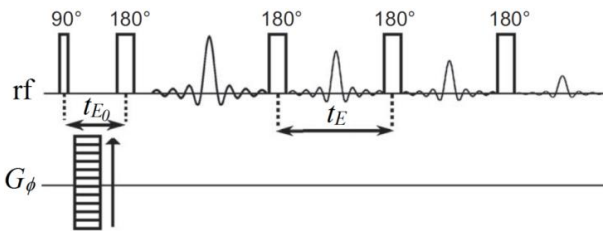

Figure 22. T_2 mapping SE-SPI method. This method employs a 90° rf excitation pulse followed by a gradient pulse G_ϕ and a series of 180° pulses.

Free Induction Decay Single Point Imaging (FID-SPI) for Moisture Profiles

In contrast to Spin Echo measurements, profiles investigated with SPI methods are T_2^* weighted. A basic SPI measurement consists of an excitation pulse with a flip angle α typically smaller than 90° applied in the presence of spatial encoding gradients where one data point is acquired at a time t_p after the excitation pulse. In the case of FID-SPI spatial encoding gradients are applied after an excitation pulse and multiple time domain points are recorded after t_p separated by a delay time τ during the FID (Figure 23). The measurement is repeated after a time t_R with an incremented strength of the magnetic field gradient pulses. All time domain points acquired are encompassed by the variable t_p below. The image signal for a certain region ($\boldsymbol{r}$) is given by [*Marica et al.*, 2014]

$$M\left(t_p,\boldsymbol{r}\right)=M(0,\boldsymbol{r})exp\left(-t_p/T_2^*\right)\ sin\,\alpha \tag{3.3.6}$$

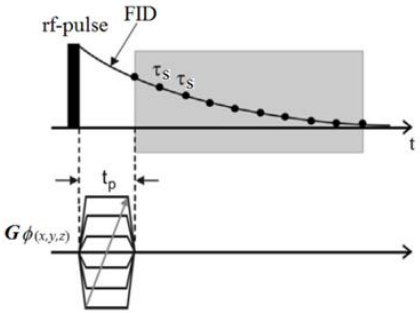

Figure 23. FID-SPI method. At time t_p after the rf excitation pulse of α = 90° and the phase encoding gradient pulse $G_{\phi(x,y,z)}$ the FID is recorded at a series of fixed times each separated by a time τ_s.

Single Point Ramped Imaging with T_1 Enhancement (SPRITE) for Imaging

A SPRITE method with centric scanning of k-space was employed for 1D and 2D moisture imaging. This method is based on full spatial phase encoding and starts *k*-space sampling at the *k*-space origin (Figure 24). The image signal intensity is given by

$$M(t_p,\boldsymbol{r})=M(0,\ \boldsymbol{r})\,exp\,\{-t_p/T_2^*\}\ \sin\,\alpha \tag{3.3.7}$$

With a bulk T_2^* of 0.24 ms for the sample under study, assumed quasi constant, and a time after pulse t_p of 0.125 ms the signal is directly proportional to the sample magnetization and thus moisture [*Mastikhin and Balcom*, 2012; *Muir and Balcom*, 2012].

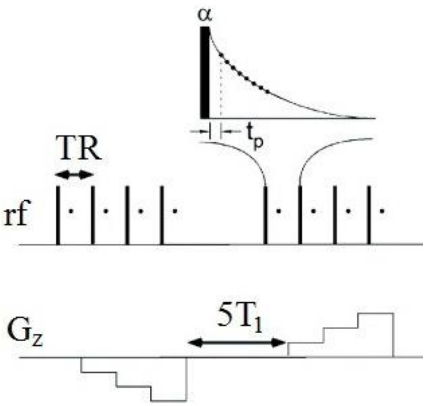

Figure 24. Schematic description of the 1D centric scan DHK SPRITE method. A single data point is acquired at time t_p after the rf excitation pulse of angle α in the presence of a phase encoding magnetic field gradient G_z. The gradient is ramped through half of the k-space where the second half is acquired after a delay of $5T_1$. The time between each subsequent rf- pulse is TR.

Spin Echo (SE) MRI for moisture determination

Spin echo imaging is one of the fundamental methods in MRI (Figure 25). The echo after a time 2τ (echo time t_E) is formed by a 90° excitation pulse and one or more refocusing 180° pulses applied after a time τ. SE images are usually obtained by applying frequency and phase encoding gradients. By imposing a slice encoding gradient, single slice or multislice acquisition can be performed to achieve a 2D representation of the 3D sample under question. The image intensity can be described by [*Bernstein et al.*, 2004; *Callaghan*, 1993]

$$M(t_E,\mathbf{r})=M(0,\mathbf{r})\ exp\{-t_E/T_{2,app}\}\ (1-exp\ \{-t_R/T_1\}) \tag{3.3.8}$$

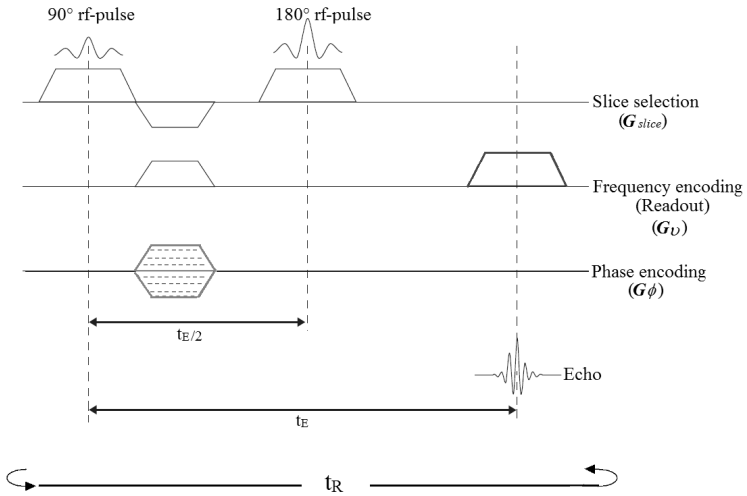

Figure 25. Basic pulse diagram of a Spin Echo (SE) method. The slice selective gradient applied (G_{slice}) during the 90° rf-pulse dephases the magnetization along the direction of slice selection. An inverse slice selective gradient pulse is applied afterwards to compensate this effect. After the 90° pulse a frequency (G_υ) and phase encoding (G_ϕ) gradient is applied. After time $t_E/2$ a 180° rf- pulse is applied in the presence of G_{slice} which refocuses the spin phase spread where a signal (echo) is generated after time t_E (echo time) in the presence of G_υ. The sequence is repeated after a delay time t_R (repetition time) where the strength of G_ϕ is incrementally ramped in equal steps for each cycle (dotted lines).

3. Material and Methods

Porous Material

A cylindrical sample 60 mm in length and 38 mm in diameter was packed with a natural silt loam (15.5% sand, 73.8% silt and 10.7% clay), a soil typically used in agriculture since it supports the growth of virtually all forms of crops. A bulk density of $\rho_B = 1.2$ g cm^{-3} and a total porosity of $\varepsilon = 0.55$ by using the relationship $\varepsilon = 1 - \rho_B / \rho_{grain}$ assuming $\rho_{grain} = 2.65$ g cm^{-3} [*Cameron and Buchan*, 2005] was achieved and the column was saturated from the bottom, which was sealed afterwards, yielding an initial volumetric water content of $\theta_s = 0.9\varepsilon$ [cm^3 cm^{-3}] [*Rogowski*, 1971]. Thereafter evaporation could only occur at the column surface. To eliminate the influence of radial radiation the sample was insulated using Armaflex. Between the MR measurements the sample was held under isothermal conditions in an environmental chamber

(Caron 6010) with a constant vapor pressure deficit of 1.1 kPa (temperature = 25°C; relative humidity = 65%). To determine the evaporation from a free water surface (pan or potential evaporation e_0) a 70 mm x 70 mm x 150 mm container was evaporated together with the sample under question under identical conditions. The weight of the system was recorded every 24 hours.

For standardization 5 glass tubes of 16 mm in diameter and 18.5 mm in height were packed separately with the same silt loam material achieving an identical total porosity of ε = 0.52. All samples were fully saturated and evaporated until 5 different volumetric water content were achieved (θ [cm^3 cm^{-3}] = 0.5, 0.31, 0.28, 0.14, 0.08). All samples were sealed in order to prevent further evaporation and thus moisture variations.

Moisture profiles

Due to the proportionality between the extrapolated MR amplitude and moisture in the sample the moisture saturation deduced from MR measurements can be expressed as the effective MR saturation:

$$\Theta_{MR}=(\Theta_{a,MR}-\Theta_{r,MR}) / (1-\Theta_{r,MR}) \tag{3.3.9}$$

with $\Theta_{a,MR}=M(0,\boldsymbol{r}) / M(0,\boldsymbol{r})_{saturated}$, where $M(0,\boldsymbol{r})$ and $M(0,\boldsymbol{r})_{saturated}$ are the signal amplitude at partial and initial saturation, respectively. $\Theta_{r,MR}$ reflects the relative MR signal at residual water content. This procedure removes the impact of systematic inaccuracies with identical characteristic caused by rf-inhomogeneities and local heterogeneities due to the soil packing.

4. MR Setup

MRI

Measurements were performed using a vertical bore MARAN DRX-HF imaging system (Oxford Instruments) equipped with Techron gradient amplifiers (Type 7782, AETechron, Elkhart, IN, USA), water cooled gradient coils and a custom-built rf-resonator with a resonance frequency of 8.5 MHz and an inner diameter of 45 mm. Measurements were performed every day with a reproducible position by using a labjack where the middle of the sample matched the isocenter of the probe.

Unilateral NMR

Additional sensitivity measurements were carried out using a unilateral three magnet array. As Figure 26a shows the original setup developed by [*Marble et al.*, 2007] and even the modifications introduced by [*García-Naranjo et al.*, 2010] only considered a horizontal orientation of the probe. Since various applications exist where the nature of the sample requires a vertical direction, the three magnet array was modified in order to enable a vertical or horizontal adjustment. Therefore, the magnet array was fixed to an aluminum frame which can be rotated between horizontal and vertical orientation allowing measurements of samples indefinite in length for both orientations (Figure 26b-d). The probe was encased in copper plates sitting on a larger plate fixed by brass screws in order to i) ensure a precise and equal positioning in the homogenous field of the magnet and ii) facilitate a fast and easy replacement of probes with certain diameter. No change in the dead time (70 µs) of the rf-probe was found after the modifications. The sample was placed vertically in the solenoid probe of 42 mm inner diameter with a sensitive spot 24 x 15 x 10 mm^3 displaced 20 mm from the magnet surface. The probe was centered at a frequency of 2.25 MHz and connected to a LapNMR console (Tecmag, Houston, USA) with a 250 W rf amplifier (TOMCO, Stepney, Australia) and a preamplifier (MITEQ, Hauppauge, USA).

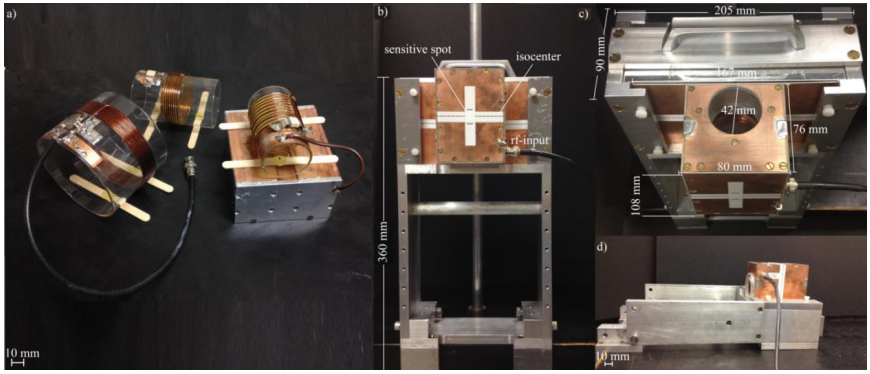

Figure 26. Setup of the three magnet array (a) 3 magnet array with probes of different diameter as originally developed by [32] . (b) Frontal view of the new 3 magnet array setup aligned for vertical measurements with the array attached to an aluminum frame. The probe is encased by means of copper plates placed on a larger plate in order to enable an accurate and easy positioning and removal. (c) Top view of the setup. (d) Side view of the new setup aligned for horizontal measurements.

5. MR/MRI Measurements

Table 3. Acquisition parameters of Inversion Recovery (IR), Carr-Purcell-Meiboom-Gill (CPMG), Spin Echo Single Point Imaging (SE-SPI), Free Induction Decay Single Point Imaging (FID-SPI), Single Point Ramped Imaging with T_1 Enhancement (SPRITE) and Spin Echo Imaging(SE) methods. Repetition time = t_R, echo time = t_E, time after pulse = t_P, flip angle = α, number of echoes =NE, number of time domain points = NP, number of scans = NS.

Measurement	Bandwidth (kHz)	t_R (ms)	t_E (ms)	t_P (ms)	α (°)	NE	NP	NS	Measurement time (min)
				8.5 MHz Imaging System					
IR	125	200	-	-	90	-	-	-	5
CPMG	125	1000	0.25	-	90	512	-	128	3
SE-SPI	125	200	0.7	-	90	512	-	128	30
FID-SPI	20	200	($t_{E,0}$ = 0.72) -	0.325	90	-	256	8	0.5
SPRITE 1D	125	200	-	0.125	2.6	-	9	128	0.7
SPRITE 2D	125	200	-	0.125	2.6	-	9	128	12
SE	125	1000	4.14	-	90	1	-	2	3
				2.2 MHz Three Magnet Array					
CPMG	125	1000	0.25	-	90	512	-	128	3

Moisture Mapping

A T_2^* of 0.24 ms (line width = 1.33 kHz) was determined by a simple 90° pulse FID measurement for the sample under study. All MRI data was acquired in a 64 or 64 x 64 pixel primary data matrix for 1D or 2D, respectively and a 128 mm field of view achieving a resolution of 2 mm / pixel. For SE-SPI, SPRITE and FID-SPI, prior to Fourier transformation, the k-space data was smoothed by using a *Hanning low pass filter* [*Williams and Taylor*, 1995]. Unilateral three magnet array profiles were acquired by fitting the echo decay train of a CPMG measurement. After each measurement the sample was raised 10 mm to achieve a moisture profile for the total sample length of 60 mm.

6. Results and Discussion

Evaporation during drying

The relative evaporation rate e/e_0, where e_0 is the pan evaporation under identical ambient conditions and the effective saturation (Θ) over time are given in Figure 27. Immediately after saturation the relative evaporation rate diminished from 0.92 to 0.8 and remained constant over a period of 9 days. Thereafter a sharp drop to 0.2 marked the onset of the S*2* evaporation regime continuously decreasing from 0.2 to 0.06 at day 15.

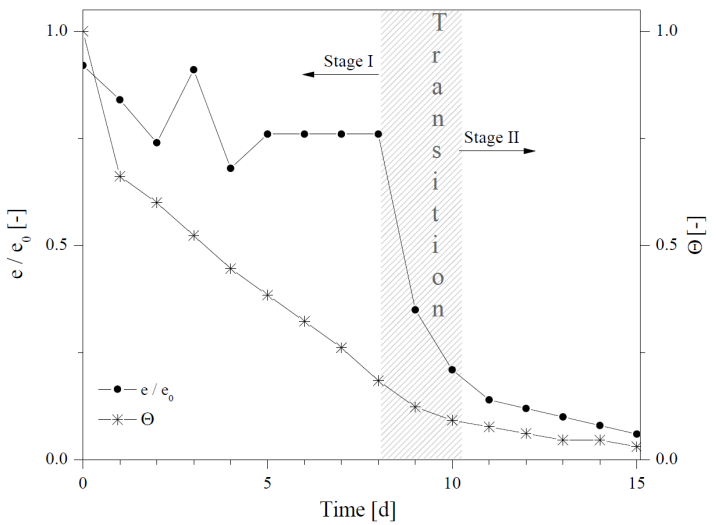

Figure 27. Relative (e/e_0) evaporation rate (filled black circles) and effective saturation Θ (cross) over time.

Moisture Profiles

First, we evaluated the sensitivity of each method using the relationship Sensitivity = SNR / $\sqrt{\text{measurement time}}$ [*Ernst et al.*, 1987], where the signal was equal to the mean MR signal intensity in a region of interest and the noise was taken as the standard deviation of the mean value derived from a flat region within the MR saturation profile. The computed sensitivities were 30 for FID-SPI and 34 for SPRITE. The highest sensitivity of 44 was obtained by the echo based SE-SPI method because this method measures $T_{2,app}$ whereas FID-SPI and SPRITE are T_2^* weighted. This is not remarkable because the sensitivity was calculated under saturated conditions where a Spin Echo (SE) method can be feasible even for porous materials with short signal lifetimes if $t_E < T_2$.

Since our main focus was the S*2* evaporation regime with an increasing desaturated surface layer, the effective MR saturation (Θ_{MR}) according to Equation 3.3.9 after 9, 11 and 15 days of drying are shown in Figure 28 for SE-SPI (a), SPRITE (b) and FID-SPI (c) and after 9 and 11 days for the unilateral three magnet array (d). S*1* evaporation occurred for approximately 9 to 10 days where the moisture content was homogenously distributed and the evaporation front located at the soil surface. Since the profiles were acquired with $t_p < T_2^*$ for SPRITE and $t_p \approx T_2^*$ for FID-SPI, differences in these profiles were caused by differences in the t_p and t_E (SE-SPI) parameters of the imaging methods. Quasi-homogenous, similar shaped, profiles with a mean Θ_{MR} of 0.20 and 0.17 were found for SE-SPI and SPRITE, respectively, whereas FID-SPI showed a mean Θ_{MR} of 0.14 and a more heterogeneous profile. The desaturated surface zone extended to 8 mm after 11 days of drying (FID-SPI) and 14 mm (SE-SPI) whereas the results from SPRITE measurements suggest a shallower extend of 6 mm. The corresponding mean Θ_{MR} at this point of drying were 0.09 (SE-SPI), 0.06 (FID-SPI) and 0.1 (SPRITE). During the S*2* evaporation regime a strong moisture gradient developed attached to the secondary evaporation front inside the soil. As drying proceeded at day 15 the extent of the dry surface layer was 28 mm (SE-SPI), 25 mm (FID-SPI) and 18 mm (SPRITE) with an corresponding mean Θ_{MR} of 0.02 (FID-SPI), 0.04 (SPRITE), and 0.03 (SE-SPI), where the latter two methods showed a linear decrease in moisture from the bottom of the column up to the transition to the desaturated surface layer. Due to the signal loss caused by i) the significantly short T_2 population at this stage of drying with low water content particularly in the topmost layer and ii) the period between excitation and signal detection (t_p and t_E), the difference in the measured extent of the dry layer was caused by the difference between the methods. The extent of the dry layer at day 15 monitored by FID-SPI differed from SE-SPI by a factor of 1.1 and to SPRITE by a factor of 1.4, whereas a factor of 1.6 was found between SPRITE and SE-SPI.

For the unilateral three magnet array a mean Θ_{MR} of 0.23 after 9 days of drying was found which decreased further to 0.08 after 11 days with an dry surface layer 10 mm in thickness.

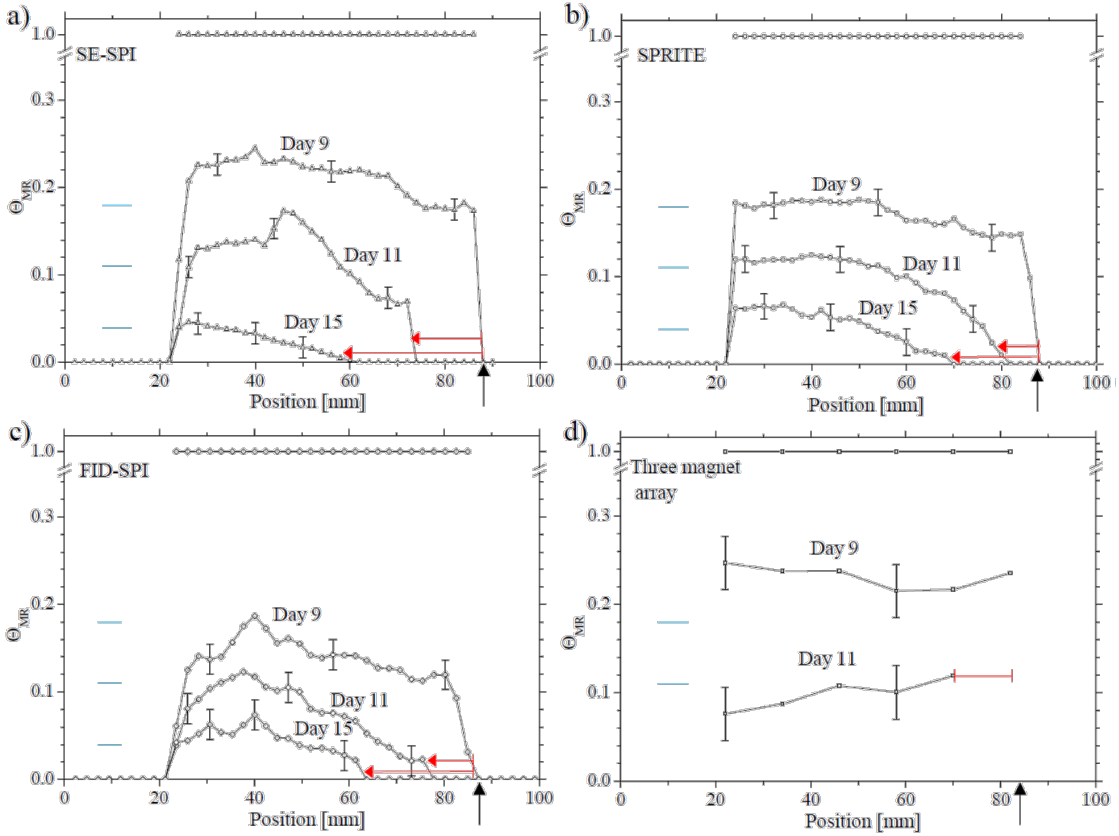

Figure 28. MR saturation profiles after 9, 11 and 15 days of drying monitored at 8.5 MHz by means of SE-SPI (a), SPRITE (b) and FID-SPI (c). The red arrow marks the depth of the secondary evaporation front. The black arrow indicates the soil surface (top) and the corresponding average effective saturation (Θ) determined gravimetrically is given as a blue line. The initial MR saturation given as the solid line at Θ_{MR} = 1 reflects the column length. The MR saturation profiles after 9 days and 11 days monitored by using the 2.2 MHz three magnet array are given in (d) where the red bar marks the extent of the secondary evaporation front.

Due to the predominant short T_2 population under progressing desaturation, and increased noise caused by the open geometry of the sensor, no profiles could be monitored after day 11 with the three magnet array. Since the size of the sensitive spot of 10 mm limited the vertical resolution of the array (see Figure 28d) and therefore a sharp drying or wetting front appears to be blurred. A future possibility is to apply an adequate inversion algorithm in order to overcome this issue. A certain volume of a sample with a sharp drying or wetting front could be placed at one end of the sensitive spot and will then be monitored by means of a certain MR method until a signal is obtained. The procedure will then be repeated whereat the sample is raised by a certain step size after each measurement. Processing the data by applying an adequate deconvolution procedure, a finer resolution should be achievable.

In order to illustrate the advantage of SPRITE over a conventional SE method for probing porous media we compared both imaging methods using samples of the same silt loam with different saturation (Figure 29). For the conventional SE method (a) an image could be achieved for the fully saturated sample only, whereas the SPRITE method (b) showed a local signal which was proportional to Θ over the whole range of saturations. The main advantage of SE-SPI towards SE is the significantly shorter echo time of $t_E = 0.7$ ms compared to $t_E = 4.14$ ms. For visualization of the drying process with focus on a desaturated surface zone we applied a 2D SPRITE method to obtain images of the moisture distribution within the soil column after certain times of drying (Figure 30) . By integrating the signal intensity of the 2D SPRITE images the corresponding moisture profiles clearly exhibit a decrease in moisture and the formation of a dry layer inside the soil. The accuracy of each method can be best assessed by plotting the mean Θ_{MR} of the entire column versus the average effective saturation Θ, determined gravimetrically for each observation day (Figure 31). For the first four days no significant difference between SE-SPI, SPRITE and the three magnet array can be observed and Θ correlates well with the mean Θ_{MR}. However, in contrast to the other methods FID-SPI systematically underestimates the moisture by a factor of 2 with progressing desaturation that is also reflected in the Θ_{MR} profiles. Since this method is T_2^* weighted both, deviation and low sensitivity of the method can be explained by the delay of $t_p = 0.325$ ms between excitation and the acquisition of the first data point which is longer than the average T_2^* of 0.24 ms. SE-SPI shows larger deviations with respect to Θ under progressing desaturation which is also caused by the short T_2 populations leading to a MR signal loss during the t_E period of 0.7 ms. Θ_{MR} investigated by means of SPRITE correlates well with Θ for all drying stages since it is a T_2^* weighted pure phase encoding method with a sufficiently short detection period of $t_p = 0.125$ ms and therefore does not suffer from multiexponential T_2 decay.

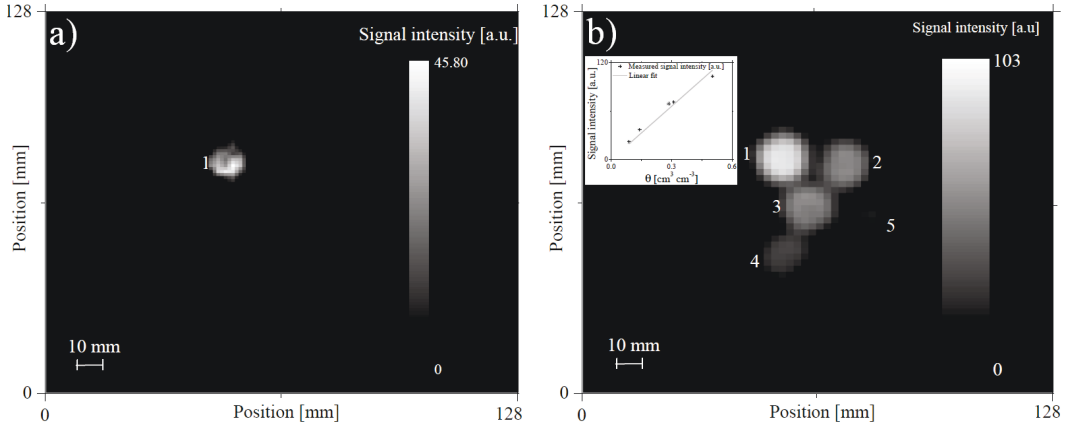

Figure 29. 2D image of a conventional Spin Echo (SE) method (a) using a t_E of 4.2 ms and a pure phase encoding SPRITE method (b) using a t_P of 0.125 ms for 5 silt loam samples with different water content. θ [cm^3 cm^{-3}]: 0.5 (1), 0.31 (2), 0.28 (3), 0.14 (4), 0.08 (5). The insert in (b) shows the relative signal intensity plotted versus the gravimetric water content.

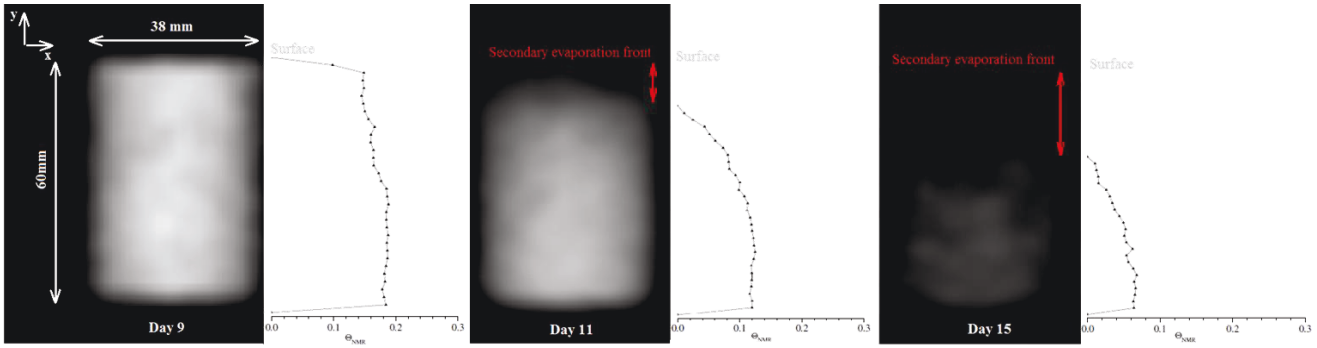

Figure 30. 2D images of the sample during drying where a dry layer developed after the onset of S2 evaporation at day 11 and further receded into the soil reaching a final depth of around 18 mm at day 15.

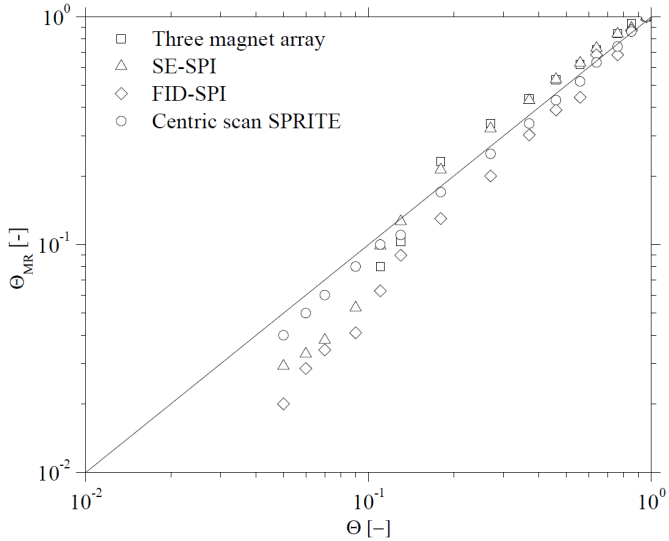

Figure 31. Effective MR saturation (Θ_{MR}) for the 2.2MHz three magnet array (□) and SE-SPI (△), FID-SPI (◇), SPRITE (o) monitored by means of the 8.5 MHz magnet plotted against the effective saturation (Θ) determined gravimetrically.

T_1 and $T_{2,app}$ relaxation times

Relaxation times of the entire sample were monitored without spatial encoding by means of IR (T_1) and CPMG ($T_{2,app}$) measurements (Figure 32) and with a vertical resolution of 2 mm by using SE-SPI ($T_{2,app}$) (Figure 33). Figure 32a shows the T_1 relaxation time spectrum where the logarithmic mean T_1 shifted from 15 ms under saturated conditions to 0.8 ms after 15 days. Due to the progressing moisture depletion, water became primarily associated with small pores, films and edges, reflected by a decreasing T_1 spectrum curve area coincided with shorter logarithmic mean T_1 values. In contrast to T_1, $T_{2,app}$ is a measure of the spin-spin interaction. Figure 32b shows the $T_{2,app}$ relaxation time spectrum where, for the sake of simplicity, the logarithmic mean $T_{2,app}$ relaxation times for each method under saturated conditions and after 11 days is summarized in Table 4.

Table 4. Logarithmic mean (lm) $T_{2,app}$ relaxation times under saturated conditions ($\Theta = 1$) and after 11 days ($\Theta = 0.11$) monitored by means of SE-SPI and CPMG using a 8.5MHz magnet and the 2.2 MHz unilateral three magnet array. The echo times are given as t_E.

Method	ν_0 (MHz)	t_E (ms)	lm$T_{2,app}$ (start $\Theta = 1$) fast mode (ms)	slow mode (ms)	lmT_2 (day 11, $\Theta = 0.11$) (ms)
SE-SPI	8.5	0.7	0.5	4.0	0.7
CPMG (whole sample)	8.5	0.25	0.3	4.0	0.6
Three magnet array	2.2	0.25	0.3	8.0	1.0

By comparing Figure 33a and b to the integral $T_{2,app}$ values of the entire column monitored by means of CMPG on the 8.5MHz system (Figure 32b) a bimodal behavior with an identical slow mode at a logarithmic mean $T_{2,app}$ of 4 ms was found although the fast mode shifted to a slightly higher value of 0.3 ms. With progressing desaturation both, the logarithmic mean $T_{2,app}$ and the area of the spectrum decreased and after 9 days the shift in $T_{2,app}$ coincided with a drop in the evaporation rate (Figure 27) down to an average effective saturation of $\Theta = 0.2$, the critical saturation value, which marked the onset of S*2* evaporation. After 11 days the logarithmic mean $T_{2,app}$ monitored by CMPG shifted to 0.6 ms and coincided with a further decreasing curve area in the relaxation time spectrum that reflects a progressing desaturation. At day 15 where the effective saturation Θ decreased to 0.05 the logarithmic mean $T_{2,app}$ could be found at 0.4 ms for CPMG measurements of the entire column.

Vertical $T_{2,app}$ profiles under saturated conditions and after 11 days monitored using SE-SPI with a spatial resolution of 2 mm are shown in Figure 33a and b. Under saturated conditions (a) a bimodal trend with a pronounced slow mode at 4 ms and a fast mode around 0.5 ms were observed. During 11 days of drying (b) the logarithmic mean $T_{2,app}$ decreased to 0.7 ms with the loss of bimodality because large pores were desiccated first and water was then primarily associated either with small pores, pore walls of larger pores or edges between pores (film water) [*Mohnke*, 2014]. At this stage of drying a secondary evaporation could be monitored by SE-SPI located at a depth of ≈ 12 mm because above this depth no signal could be detected. By comparing the logarithmic mean $T_{2,app}$ under saturated conditions and after 11 days monitored by means of SE-SPI using a t_E of 0.7 ms to a CPMG method with an t_E of 0.25 ms a good agreement could be found even if a 3 times longer t_E was used for SE-SPI. Therefore, we conclude that diffusion in

internal fields according to Equation 3.3.4b does not significantly contribute to the relaxation process. Similar effects were described by [*Kleinberg et al.*, 1993; *Kleinberg*, 1994]. They found no significant diffusion effects on T_2 measured at 2 MHz resonance frequency using short t_E, hence T_2 is dominated by surface relaxivity. Comparing the $T_{2,app}$ relaxation time spectrum monitored using SE-SPI (Figure 33a and b) and CPMG (Figure 32a) to the spectrum achieved by the unilateral three magnet array (Figure 33c and d) a bimodal behavior under saturated conditions (c) was found with a logarithmic mean $T_{2,app}$ at a slow mode of 8 ms and a fast mode of 0.3 ms. After 11 days of drying (d) the secondary evaporation front was located at a depth of 10 mm and the logarithmic mean $T_{2,app}$ shifted to 1 ms showing no bimodality. Moisture monitoring by means of the three magnet array could be performed only until day 11; thereafter no signal was detectable due to a poor S/N ratio (Figure 33d insert). However, at this stage of desaturation the secondary evaporation front was smeared out at a depth of 10 mm since the spatial resolution for the three magnet array was much coarser (10 mm) compared to SE-SPI (2 mm).

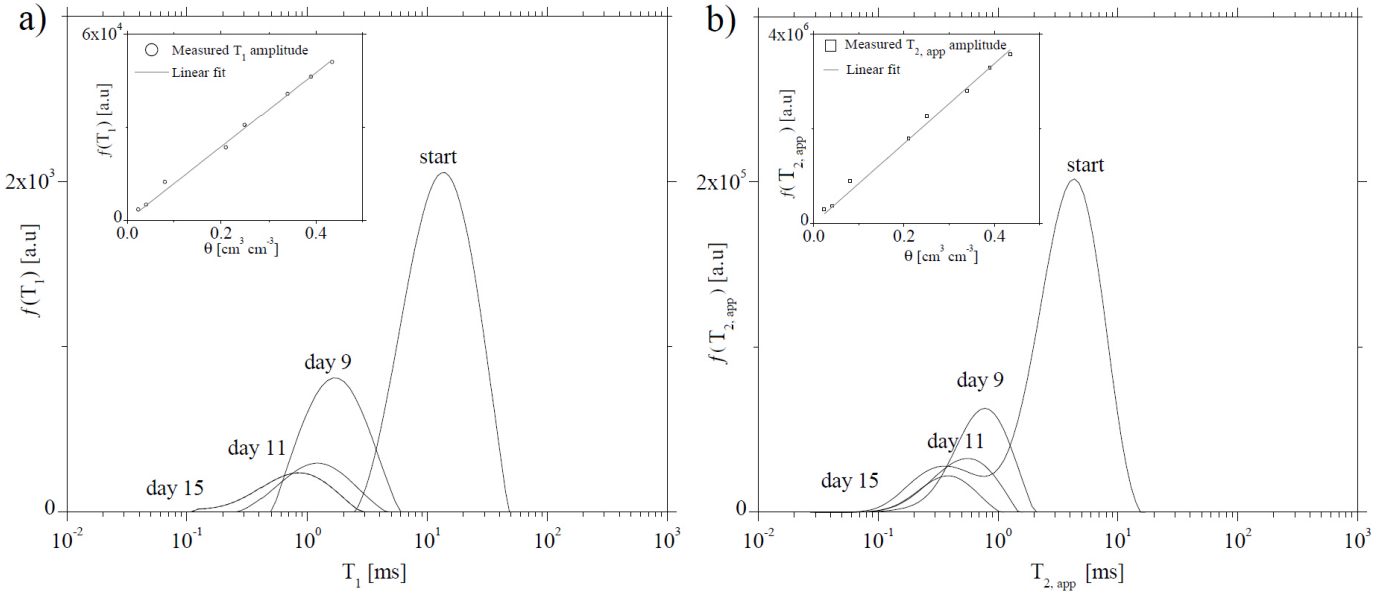

Figure 32. T_1 (a) and $T_{2,app}$ (b) relaxation time spectrum (measured at 8.5 MHz) for the silt loam under saturated conditions ($\Theta = 1$), after 9 days (the onset of *S*2 evaporation), 11 days and for the residual water content ($\Theta = 0.05$) after 15 days. The insert shows an exponential fit (grey line) for the T_1 (filled black squares) and $T_{2,app}$ (open squares) peak areas of each relaxation time spectrum plotted against the water content. The $T_{2,app}$ values (b) were determined by means of a CPMG method with an echo time (t_E) of 0.25 ms.

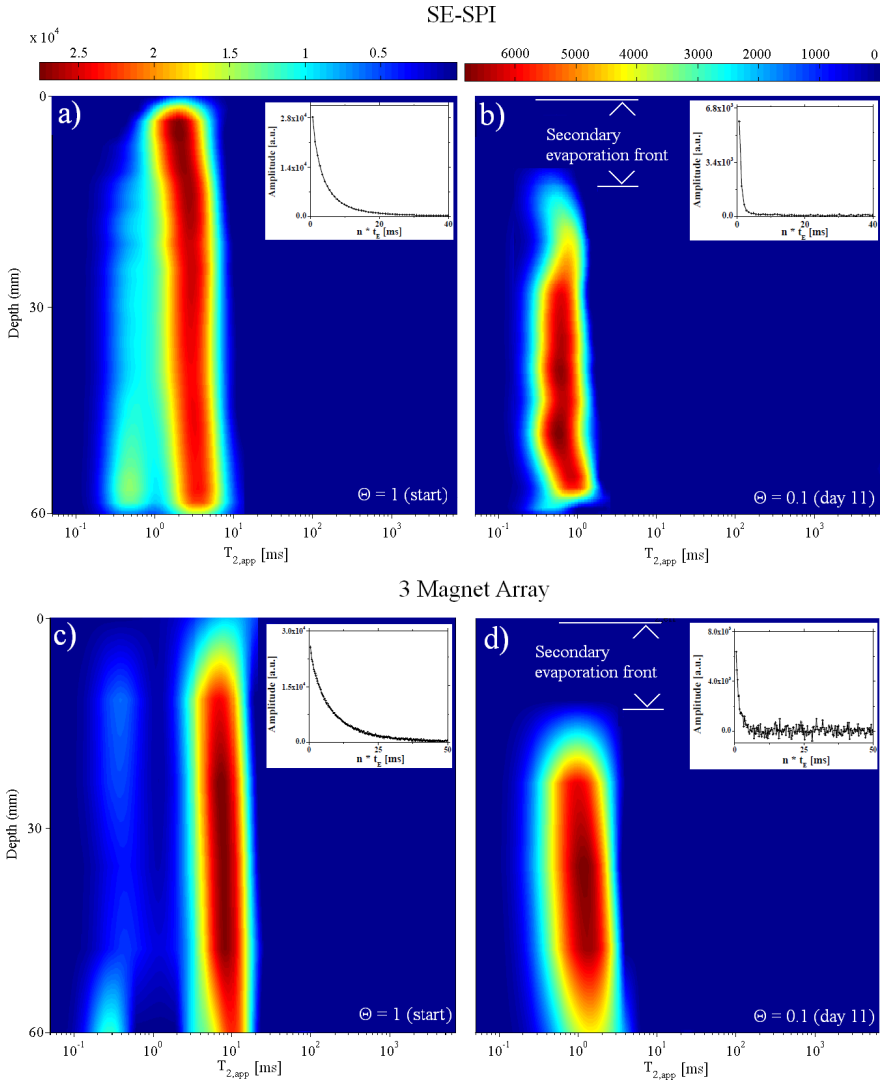

Figure 33. $T_{2,app}$ relaxation time spectrum of the silt loam column investigated at 8.5 MHz by means of SE-SPI (a and b) with a t_E of 0.7 ms and a CPMG method (t_E = 0.25 ms) using a 2.2 MHz unilateral three magnet array (c and d). A representative decay curve for each state of saturation at a depth of 30 mm is given as insert.

Because no significant shift in the $T_{2,app}$ relaxation time spectrum could be found when a larger t_E was applied on the 8.5 MHz system and an identical echo time of t_E = 0.25 ms was used for the three magnet array and CPMG, the constant shift in the $T_{2,app}$ relaxation time spectrum by a factor of 2 between the 8.5 MHz system (SE-SPI and CPMG) and the 2.2 MHz unilateral three magnet array was caused by the different Larmor frequencies and thus not due to diffusion in internal gradients. However, diffusion effects in porous media are rather complex and still the subject of investigation [*Mitchell et al.*, 2013; *Washburn et al.*, 2008]. By choosing an 8.5 MHz and a 2.2 MHz magnet as well as applying sufficiently short echo times $t_E <$ 0.7 ms, CMPG detection doesn't suffer from diffusion in internal magnetic field gradients.

7. Summary and Conclusions

The ability of different MR techniques to study moisture dynamics and relaxation time spectra during drying of a natural porous medium was assessed on a 8.5 MHz MRI instrument and a 2.2 MHz unilateral magnet. The conventional SE frequency encoding method suffered from fast T_2 relaxation, especially under desaturated conditions. It is therefore not reliable to investigate moisture changes in a natural soil material with increased amounts of clay and silt but can, nevertheless be a feasible method for soils with a significant sand content. The pure phase encoding SPI methods are immune to these phenomena since T_2^* decay is probed rapidly after excitation and they were therefore shown to be feasible to follow the drying process, and to determine the extent of a receding secondary evaporation front. Further, these methods do not suffer from artifacts due to frequency encoding [*Pusey et al.*, 1986]. Paramagnetic impurities and clay content of the soil material as well as the period between excitation and detection determined a priori how much signal was lost before image capture. It is advantageous for quantification that T_2^* is typically single exponential in porous media whereas T_2 is multiexponential By using SPRITE with t_p = 0.125 ms which is shorter than the T_2^* of the sample (0.24 ms) signal loss during the first encoding period played a minor role and did not interfere with the detection of Θ_{MR}. For FID-SPI t_P was limited to 0.325 ms due to technical reasons that led to significant decay which is reflected in a lower apparent Θ_{MR} saturation and a bias comparing Θ_{MR} to Θ. SPRITE did not suffer from the spin echo effects and is therefore the method of choice for monitoring moisture changes in natural soils. Nevertheless, to determine a quick estimate on water content distribution in a porous medium, FID-SPI can be used since it is a more sensitive image measurement.

Chapter IV

^{1}H-Magnetic resonance monitoring and numerical modeling of soil moisture during evaporation[4]

Abstract

Evaporation from bare soil surfaces can be restrained to a large amount with the origin of a dry subsurface layer what significantly impacts all processes coupled to the water cycle. Since water and water vapor are depleted from single pores of the soil matrix, an accurate characterization of these processes is required to predict the spatial variability of soil moisture at the field scale. In this study we employed different non-invasive Magnetic Resonance (MR) methods to monitor the evaporative drying of a silt loam and a sandy loam in high resolution at the lab scale with various soil profile depths. The MR data was used to evaluated a numerical simulated vertical moisture profiles using a coupled water, heat and vapor flow model approach in comparison to the one dimensional Richards equation. From the basis of our results two distinct drying regimes for both soil types were found where at the onset of the second evaporation stage a dry subsurface zone developed extending over time, independent of the soil profile extent. Our modeling results clearly demonstrated the need to consider heat and vapor flow also at lab scale processes. We further demonstrated the feasibility of simple and robust MR methods to investigate pore scale processes at the lab which might easily be transferred to the field scale in order to monitor moisture variability of the topmost soil layer in high resolution.

[4]Adapted from: Merz, S., B. J. Balcom, R. Enjilela, J. Vanderborght, Y. Rothfuss, H. Vereecken and A. Pohlmeier, ^{1}H-Magnetic resonance monitoring and numerical modeling of soil moisture during evaporation, (submitted)

1. Introduction

Evaporation and plant transpiration constitute two fundamental components in earth's water cycle since they deplete more than half of the precipitation. In this connection, evaporation from bare soil surfaces consumes one quarter of the incoming solar radiation and therefore controls the vapor and energy fluxes from the lithosphere to the atmosphere. Since soils typically consist of a solid phase and voids which are filled by liquid or gaseous phases in different fractions they are natural porous media. The drying of soil without a supplying water table usually proceeds in two distinct stages [*Or et al.*, 2013; *Scherer*, 1990; *Schlünder*, 2004]. During the first stage (*S1*), where evaporation is determined by the evaporativity of the atmosphere (assuming a sufficient conductive soil), the evaporation rate (e) is relatively constant (often referred to as the constant rate period or energy-limiting rate) and close to the rate from a free water surface (e_{pan}) under identical ambient conditions. The majority of the evaporative demand is supplied by the hydraulically connected capillary water flow from within the porous media to the surface, where the transition to vapor occurs. The process at this stage is controlled and determined by external conditions such as vapor pressure deficit [*Neriah et al.*, 2014] and wind velocity [*Shahraeeni et al.*, 2012]. During *S1* the desaturation of the soil surface progresses coincided with an increasing matric suction head what, in turn, will cause moisture from wetter layers below to be drawn upward. During this stage the evaporation rate remains, nevertheless, constant. When the surface becomes fully desiccated moisture evaporates below the surface forming a secondary evaporation front where water vapor transport occurs due to a latent heat flux through an increasing dry layer towards the soil surface atmospheric boundary layer. At this second stage of drying (*S2*), the evaporability of soil moisture (the ability of the soil to yield moisture) becomes the limiting factor for evaporation. Hence, the increasing dry surface layer during *S2* leads to increasing diffusion path lengths and the evaporation rate drops significantly.

Various approaches to describe and predict the onset of *S2*, the extent of the dry surface layer and the evaporation rate during *S2* can be found in literature (e.g., *Feyen et al.* [1998]; *Keulen and Hillel* [1974]; *Laurindo and Prat* [1998]; *Lehmann et al.* [2008]; *Qiu and Ben-Asher* [2010]; *Yiotis et al.* [2007]). One fundamental key concept has been introduced by *Philip and De Vries* [1957] in 1957. Nevertheless, predicting drying rates and moisture development in soils still remains challenging particularly under *S2* conditions [*Tran et al.*, 2015]. To simulate vertical soil moisture profiles the one dimensional Richards equation is commonly used which only considers liquid water flow and the hydraulic functions are commonly given by the Brooks and Corey [*Brooks and Corey*, 1964] or Mualem van-Genuchten [*Mualem*, 1976; *van Genuchten*, 1980] parameterization. The one dimensional Richards' approximation considers: i) isothermal water flow and ii) uses an unsaturated hydraulic conductivity based on the capillary bundle model. Various studies reveal that in unsaturated soils mass and energy between liquid and vapor are

frequently exchanged in the topmost layer [*Jassal et al.*, 2003; *Zeng*, 2013] what lead to a distinct dry layer below the surface of a bare soil where the profile below this layer remains much wetter. Therefore, to compute vertical moisture profiles caused by evaporation the water flow needs to be coupled to the vapor and heat fluxes since the Richards' approach uses a fixed pressure head at the soil surface and only considers liquid water flow. Therefore, this model cannot accurately reproduce the dynamics controlling *S2* evaporation and therefore overestimates the amount of water in the top layer [*Liu et al.*, 2005; *Novak*, 2010; *Sakai et al.*, 2009; *Teng et al.*, 2016].

In this regard, *Saito et al.* [2006] demonstrated numerically that under S2 conditions evaporation is strongly associated with vapor and heat transport. They evaluated the model using large scale field soil temperature and water content data. Since evaporation is a highly nonlinear process where under progressing desaturation processes inside the soil control to a large extend not only the dynamics of evaporation but determine a priori how much water is lost to the atmosphere pore scale processes are the driving factors which manifest themselves on large scales. Further, several methods like remote sensing exist [*Robinson et al.*, 2008] using soil surface temperature to determine soil moisture [*Qiu and Ben-Asher*, 2010] what can led to substantial deviations if vapor transport in the subsurface layer is neglected.

Several studies on evaporation from bare soils have been conducted for the lysimeter and mesoscale [*Assouline et al.*, 2013; *Bittelli et al.*, 2008; *Jassal et al.*, 2003; *Liu et al.*, 2005; *Moghadas et al.*, 2013; 2014; *Vanderborght et al.*, 2010; *Wythers et al.*, 1999], nevertheless non-invasive laboratory or pore scale measurements of near surface moisture still remain rare (e.g. *Shokri et al.* [2008], *Han and Zhou* [2013]). One study related to S*2* evaporation on a lab scale quasi-non-invasive has been conducted by [*Rothfuss et al.*, 2015] using stable isotopes measurements. They observed the origin and development of a dry surface layer using a column (60 cm in length, 11 cm in inner diameter) filled with sand. *Merz et al.* [2014] utilized the same type of sand to monitor the drying process on a smaller column (13 cm in length, 8 cm in inner diameter) by means of different Magnetic Resonance (MR) methods. They took a step further by employing a unilateral MR instrument on a laboratory lysimeter consisting of a silt loam [*Merz et al.*, 2015a] to monitor the near surface moisture content.

Since the MR technique was first used for the determination of soil moisture by *Andreev and Martens* [1960] the technique and associated methods have been undergone a constantly improvement during the course of the years and MR has become a versatile toolkit in the field of environmental science [*Nestle et al.*, 2007] and particularly for porous media research [*Koptyug*, 2012]. This is driven by the fact that MR is advantageous over other methods used for monitoring moisture since it is non-invasive and provides information on the environment of the water, the mere water content and can further provide insights on the diffusion pathways of water molecules in a probed volume [*Korb*, 2011; *Watson and Chang*, 1997]. Since the concept of single sided or unilateral MR has become more manageable [*Casanova*, 2011] since

its introduction in 1978 by the oil industry [*Kleinberg and Jackson*, 2001] direct field application has become possible.

The most prominent MR methods for field scale applications are surface (SNMR) - or earth field (ENMR) MR and bore hole MR where the latter is mostly used besides research intentions [*Müller-Petke and Yaramanci*, 2015]. This method is frequently applied in the petrol sector and requires bore holes to be drilled in order to insert the MR apparatus (MR logging tools [*Coates et al.*, 1999]) what lead to a substantial compaction of the soil in the vicinity of the instrument disabling this method for studying soil surfaces processes. SNMR, basically developed for groundwater investigations [*Legtchenko*, 2013] uses the earth magnetic field and requires large coils and mostly suffers from a low signal to noise (SNR) ratio. This aspect, in combination with the large investigated volume makes SNMR not well suited for monitoring pore scale processes.

Since sensor technologies are rapidly growing the focus constantly shifts from laboratory to field scale measurements [*Wang*, 2015] and as recently shown by *Rezaei et al.* [2016] and *Vereecken et al.* [2016] the link between in-situ characterization of soils in the laboratory to field scale investigations is of major relevance to understand vadose zone processes directly linked to modeling soil processes. Therefore, the objective of this study was to monitor the moisture development of silt and sandy loam columns exposed to evaporation on the lab scale using non-invasive and robust MR methods in high spatial resolution with the potential to be applied for MR field measurements in combination with an appropriate MR apparatus (e.g. the NMR MOUSE). Further we used our data to validate a coupled water, heat and vapor flow model and demonstrated that even on the lab scale drying of soils and particularly the formation of a dry surface layer acting as evaporative restraint cannot sufficiently be represented by liquid water flow only as it is the case for models based solely on the classical Richards approach.

2. Theory

$T_{2,app}$ Relaxation Time Distributions by means of CPMG and SE-SPI

Spin-spin (T_2) relaxation times measurements are powerful and most common techniques in order to obtain information about the local environment of water molecules confined in a porous material [*Jaeger et al.*, 2009]. T_2 values are mainly influenced by pore size, paramagnetic impurities, characteristic detection parameters (e.g. the echo time) and other variables [*Barrie*, 2000]. The four main relaxation processes involved in the signal decay of water in porous materials are given by

$$1/T_2^* = \rho_2(S/V) + 1/T_{2,bulk} + 1/T_{2,diffusion} + 1/T_{2,\ inhomogeneous} \quad (3.4.1)$$

where ρ_2 is the T_2 surface relaxivity parameter, S/V is the ratio of fluid volume to pore surface, $1/T_{2,bulk}$ is the relaxation rate of the bulk solution, $1/T_{2,diffusion}$ describes the signal loss due to diffusion in magnetic field gradients and $1/T_{2,inhomogeneous}$ describes the dephasing due to static inhomogeneities of the magnetic field. The bulk relaxation rate of pure water is usually in the range of 3 s and the term $1/T_{2,bulk}$ therefore negligible for most porous media. Since the observable decay depends on the choice of experimental parameters which control $1/T_{2,diffusion}$, both, surface relaxivity $\rho_2(S/V)$ and diffusion $1/T_{2,diffusion}$ are summarized by $T_{2,\,app}$ [*Pomerantz et al.*, 2008]. The Carr-Purcell-Meiboom-Gill (CPMG) sequence is a standard method to measure the decay of transverse magnetization. Typically a CPMG experiment uses a 90° pulse followed by a series of 180° pulses generating n spin echoes, each separated by t_E. The signal is described by

$$S(t, \mathbf{r}) = S(0,\mathbf{r})\ exp\text{-}\{t\ /T_{2,app}\} \tag{3.4.2}$$

where S(0,$\mathbf{r}$) is the initial signal amplitude, $t = n_E * t_E$, n_E is the number of echoes and t_E is the echo time.

Spin Echo Single Point Imaging (SE-SPI) T_2 mapping can provide spatially resolved monitoring of pore size distributions. After a 90° pulse, a stepped gradient pulse is applied which varies in strength for each repetition. Thereafter, a series of n 180° pulses creates n echoes after time $n*t_E$. The signal intensity after time t is given by

$$S(t,\mathbf{r})= S(0,\mathbf{r})\ exp\ \text{-}\{t_{E,0}/T_{2,app}\}\ exp\text{-}\{(n_E\text{-}1)\ (t_E/T_{2,app})\} \tag{3.4.3}$$

where $t = t_{E,0} + (n_E\text{-}1)t_E$. The echo time of the first pulse interval and the subsequent intervals are represented by $t_{E,0}$ and t_E, respectively. If a Fourier transformation is applied to the raw data followed by an inverse Laplace transformation a $T_{2,app}$ distribution for each pixel in the region of interest can be obtained. Detailed information on CPMG and SE-SPI can be found in *McIntosh* [2013] and *Petrov et al.* [2011], respectively.

Determination of Soil Moisture using 1D - Centric Scan SPRITE

A 1D – Centric Scan SPRITE method with centric scanning of k-space was employed for moisture monitoring. This method is based on a fully spatial phase encoding and starts k-space sampling at the k-space origin. The signal intensity is given by

$$S(t, \mathbf{r})=S(0, \mathbf{r})\ exp\ \{-t/T_2^*\}\ \sin\alpha \tag{3.4.4}$$

With a $t_p < T_2^*$ the signal is directly proportional to the moisture content in the sample. For a detailed description of the SPRITE method please see *Mastikhin and Balcom* [2012], *Muir and Balcom* [2012] and *Bernstein et al.* [2004], respectively.
The characteristic parameters of all MR methods described above are summarized in Table 6.

T_1 relaxation time distributions by means of Inversion Recovery (IR)

Inversion Recovery (IR) is one of most commonly used method to measure the longitudinal relaxation time constant T_1. This method is a conventional spin echo method utilizing a preceding 180° pulse. The signal is given by

$$S(t, \mathbf{r}) = S(0,\mathbf{r})\ 1- exp-\{t/T_1\} \tag{3.4.5}$$

where T_1 is the longitudinal relaxation time constant.

2.1 Modeling Moisture Development

Richards equation

In order to describe water movement in the vadose zone the Richards equation [*Richards*, 1931] is traditionally used

$$\frac{\partial\theta}{\partial t} = \frac{\partial}{\partial z}\left[K(h)\left(\frac{\partial h}{\partial z}+1\right)\right] - S(h) \tag{3.4.6}$$

where θ is the volumetric water content (moisture), h the pressure head, K the hydraulic conductivity, t the time, S a sink term and z is the vertical coordinate. To solve the Richards equation the initial and boundary conditions, the hydraulic conductivity function $K(h)$ and the moisture retention characteristic $\theta(h)$ need to be defined given by the Mualem-van Genuchten parameterization where the effective water saturation Θ given by,

$$\Theta = \frac{\theta-\theta_r}{\theta_s-\theta_r} \tag{3.4.7}$$

where θ_s and θ_r are the initial and residual saturations, respectively. The van Genuchten parameterization can then be written as:

$$\theta(h) = \theta_r + \frac{\theta_s - \theta_r}{[1+[\alpha h]^n]^{1-1/n}} \tag{3.4.8}$$

where α and n are scaling parameters with $1/\alpha$ as the air entry value and $1/n$ as a measure for pore size distribution. θ_s, θ_r, α and n are determined from a set of measurement points of soil moisture and the cor-

responding hydraulic head by minimizing the deviation between $\Theta(h)$ form Equation 3.4.7 and the measurements. Frequently, the Mualem-van Genuchten [*Mualem*, 1976; *van Genuchten*, 1980] approach is used to determine the relative $K_{Lh}(h)$:

$$K_{Lh}(h)=\frac{\left(1-(\alpha h)^{n-1}(1+(\alpha h)^{n})^{1-(1/n)}\right)^{2}}{(1+(\alpha h)^{n})^{[(1-(1/n))/2]}} \tag{3.4.9}$$

Coupled Water, Vapor and Heat Flow Model

Liquid Water and Vapor Flow

For the purpose of this work the simultaneous movement of water, vapor and heat as described by *Saito et al.* [2006] and [*Bittelli et al.*, 2008] was applied, where the liquid water and vapor transport is governed by

$$\frac{\partial\theta}{\partial t}=\frac{\partial}{\partial z}\left[K_{\mathrm{L}h}\frac{\partial h}{\partial z}+K_{\mathrm{L}h}+K_{\mathrm{L}T}\frac{\partial T}{\partial z}+K_{\mathrm{v}h}\frac{\partial h}{\partial z}+K_{\mathrm{v}T}\frac{\partial T}{\partial z}\right]-\mathrm{S}=\frac{\partial}{\partial z}\left[K_{\mathrm{T}h}\frac{\partial h}{\partial z}+K_{\mathrm{L}h}+K_{\mathrm{T}T}\frac{\partial T}{\partial z}\right]-S \tag{3.4.10}$$

with

$$K_{\mathrm{T}h}=K_{\mathrm{L}h}+K_{\mathrm{v}h} \tag{3.4.11}$$

$$K_{\mathrm{T}T}=K_{\mathrm{L}T}+K_{\mathrm{v}T} \tag{3.4.12}$$

where K_{Th} is the isothermal total (liquid water + vapor) hydraulic conductivity and K_{TT} is the thermal total (liquid water + vapor) hydraulic conductivity. The thermal conductivity describes the transport of energy due to a temperature gradient through a body of mass, whereas the isothermal vapor and liquid conductivities are unaffected by temperature gradients since they are driven by the gradient in soil water pressure. The term K is the hydraulic conductivity in general where the first character of the subscript refers to either liquid (L) or vapor (v) and the second character specifies the gradient in pressure head (h) or in temperature (T). S is a sink term which usually accounts for root water uptake which could be neglected since only bare soils were considered and z is the spatial coordinate positive upwards. The isothermal unsaturated hydraulic conductivity $K_{Lh}(h)$ is calculated by using the Mualem-van Genuchten approach according to Equation 3.4.9. The thermal hydraulic conductivity, K_{LT} is defined as

$$K_{\mathrm{L}T}=K_{\mathrm{L}h}\left(hG_{\mathrm{w}T}\frac{1}{\beta_0}\frac{\mathrm{d}\beta}{\mathrm{d}T}\right) \tag{3.4.13}$$

where G_{wT} is a gain factor which describes the temperature dependence of the soil water retention curve [*Nimmo and Miller*, 1986]. β_0 is the surface tension of water at 25°C and β the surface tension [J cm^{-2}] at a certain temperature [T in K] , described by $\beta = 75.6\text{-}0.1425(T\text{-}273.15) - 2.38\text{x}10^{-4}\,(T\text{-}273.15)^{2}$ [g s^{-2}]. K_{vh}, the isothermal vapor hydraulic conductivity and K_{vT} the thermal vapor hydraulic conductivity are given as

$$K_{vh}=\frac{D_v}{\rho_w}\,\rho_{vs}\frac{Mg}{R_u T}H_r \tag{3.4.14}$$

$$K_{vT}=\frac{D_v}{\rho_w}\,\eta H_r\frac{d\rho_{vs}}{dT} \tag{3.4.15}$$

where D_v is the vapor diffusivity in soil [$m^2\ s^{-1}$], ρ_w is the density of water (liquid) [$kg\ m^{-3}$], ρ_w is the saturated water vapor density [$kg\ m^{-3}$], M is the molecular weight of water [=0.018015 $kg\ mol^{-1}$], g is the acceleration due to gravity [= 9.81 $m\ s^{-2}$], R is the universal gas constant [= 8.341 $J\ mol^{-1}\ K^{-1}$], Hr is the relative humidity [-] and η is an enhancement facto [*Cass et al.*, 1984]. The vapor diffusivity in soil can be derived as $D_v = \tau_g\ a_v D_a$ where τ_g is the pore connectivity factor for the gaseous phase, a_v is the air filled porosity [$cm^3\ cm^{-3}$] and D_a , the diffusivity of water vapor in air [$m^2\ s^{-1}$] at temperature T [K] is given by $D_a = 2.12\text{x}10^{-5}\ (T/\ 273.15)^2$. Detailed empirical derivations are given in *Sakai et al.* [2009]

Heat Transport

The heat transport is governed by [*De Vries*, 1958]:

$$\underbrace{\frac{\partial C_P T}{\partial t}}_{\text{energy content}}+\underbrace{L_w\rho_w\frac{\partial \theta_v}{\partial z}}_{\text{latent heat of vapor phase}}=\underbrace{\left[\lambda(\theta_L)\frac{\partial T}{\partial z}\right]}_{\text{soil heat flow by conduction}}\underbrace{-C_w\frac{\partial q_L T}{\partial z}}_{\text{convection of sensible heat with water flow}}\underbrace{-C_a\frac{\partial q_v T}{\partial z}}_{\text{transfer of sensible heat by vapor diffusion}}\underbrace{-L_w\rho_w\frac{\partial q_v}{\partial z}}_{\text{transfer of latent heat by vapor diffusion}} \tag{3.4.16}$$

where L_w is the latent heat of the vaporization of water [$J\ kg^{-1}$]given as $2.501 \times 10^6 - 2369.2T$ [T in K] according to *Monteith and Unsworth* [1990]. The volumetric heat capacity C_P of the soil is given by:

$$C_P=C_n\theta_n+C_w\theta_{Ln}+C_a\theta_a \tag{3.4.17}$$

where C_n counts for the volumetric heat capacities of the solid [1.92 $MJ\ m^{-3}\ K^{-1}$], C_w counts for the volumetric heat capacities of the liquid [4.18 $MJ\ m^{-3}\ K^{-1}$] and C_a for the volumetric heat capacities of the air [0.0063 $MJ\ m^{-3}\ K^{-1}$], where all phases are multiplied by their respective volumetric fraction [$cm^3\ cm^{-3}$], where θ_n, θ_L and θ_a are the volumetric fractions of the solid, water and air phases, respectively.

$\lambda(\theta_L)$ is the thermal conductivity of the soil [$M\ L\ T^{-3}\ K^{-1}$]given as:

$$\lambda(\theta_L)=b_1+b_2\theta_L+b_3\theta_L^{1/2} \tag{3.4.18}$$

where b_1,b_2 and b_3 are constants which vary with soil composition (b values of different soil types can be found in *Chung and Horton* [1987]).

A detailed explanation on the coupled heat, vapor and liquid water transport model can be found in *Bittelli et al.* [2008]; *Saito et al.* [2006] , *Simunek et al.* [2008] and *Sakai et al.* [2009].

As boundary conditions we defined air temperature (25° C) and air humidity (65 %). The incoming long wave radiation was calculated from the emissivity of the soil surface (which was 0.9) and the emitted radiation of a black body with temperature of 25 °C, representing the radiation of the walls inside the chamber. The outgoing long wave radiation was calculated from emissivity and simulated temperature of the soil surface. The wind speed which is used to calculate the aerodynamic resistance for latent and sensible heat transfer between the soil surface and the atmosphere was adjusted such that the evaporation rate of a wet surface was equal to the average evaporation rate of *S1* for each sample.

To derive the Θ profiles as a function of depth using the one dimensional Richards approach we assumed that evaporation takes place under isothermal conditions and water flow is only driven by a gradient in h.

3. Material and Methods

Soil Samples and Hydraulic Properties

Two cylindrical acrylic columns 60 mm in length and 38 mm in diameter were packed with: i) a silt loam and ii) a sandy loam. Additionally a cylindrical glass column 500 mm in length and 33 mm in diameter was packed with the identical sandy loam. All soil samples originated from the test sites (45°55' 04.2" North, 66° 36' 29.4" West) of the Potato Research Center in Fredericton (NB, Canada) and were sieved to < 2mm and oven dried at 105° C. The soil hydraulic properties where determined by means of the HYPROP-Laboratory evaporation method (UMS GmbH Munich, Germany) [*Peters and Durner*, 2008; *Schindler et al.*, 2010a]. The water retention function and characteristic parameters of the different soils and samples are shown in Figure 34 and summarized in Table 5, respectively. Each column was initially saturated from the bottom which was sealed after saturation thus evaporation could only occur at the column surface. In order to eliminate radial radiation all samples were insulated (Armaflex). The samples were held in a climate chamber (Caron 6010) under a constant temperature of 25° C and a relative humidity of 65% between the MR measurements. Additionally, a container of 70 x 70 x 150 mm filled with pure water and a constant water table was evaporated under identical ambient conditions to determine e_0.

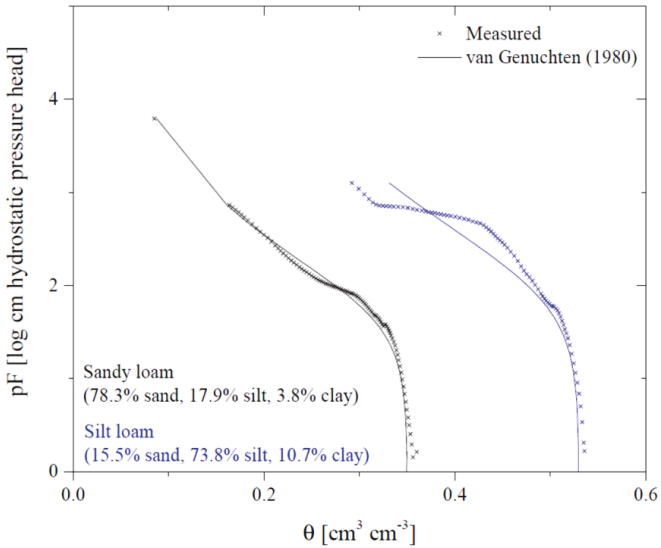

Figure 34. Measured (cross) water retention curves of the sandy loam (black) and the silt loam (blue) using the HYPROP evaporation method and fitted (line) based on *van Genuchten* [1980].

Table 5. Soil composition , Van-Genuchten-Mualem parameters, bulk density (ρ_B) and porosity (ε) for the silt loam and the sandy loam.

Soil	ρ_B (short sample) [g cm^{-1}]	ρ_B (long sample) [g cm^{-1}]	ε (short sample) [-]	ε (long sample) [-]	n [-]	α [cm^{-1}]	θ_r [-]	K_s [cm d^{-1}]	l [-]	Sand [%]	Silt [%]	Clay [%]
Sandy Loam	1.6	1.6	0.35	0.39	1.3	0.05	0.03	100	0.5	78.3	17.9	3.8
Silt Loam	1.2	-	0.5	-	1.2	0.03	0.09	50	0.5	15.5	73.8	10.7

MR Setup

A vertical bore MARAN DRX-HF imaging system (Oxford Instruments Ltd., Oxford, UK) equipped with 1 kW Techron gradient amplifiers (Type 7782, AETechron, Elkhart, IN, USA), water cooled gradient coils and a custom-built rf-resonator with a resonance frequency of 8.5 MHz and an inner diameter of 45 mm was employed to monitor the short samples. The specimens where placed vertically inside the probe

by means of a lab jack in order to reproduce an identical position for each measurement. Measurements of the long sandy loam column were performed using a vertical bore MARAN DRX spectrometer (Oxford Instruments Ltd., Oxford, UK) equipped with a 25 W amplifier and an rf- probe with an inner diameter of 51 mm operating at 2.2 MHz resonance frequency. The vertical resolution limit of the probe was restricted to 50 mm and the long sample was therefore measured in 10 steps to acquire the overall length of 500 mm by using a lab jack which was raised exactly 50 mm after each measurement. The characteristic parameters for each measurement are given in Table 6.

Table 6. Acquisition parameters of the Carr–Purcell–Meiboom–Gill (CPMG), spin echo single point imaging (SE-SPI), and single-point ramped imaging with T1 enhancement (SPRITE) MR methods.

	Short sample			Long sample		
Acquisition Parameter	CPMG	SE-SPI	SPRITE	CPMG	SE-SPI	SPRITE
Flip angle (α) [°]	90	90	2.6	90	90	3.3
Repetition time (t_R) [ms]	1000	600	200	1000	500	600
Encoding time (t_p) [ms]	-	-	0.125	-	-	0.125
First echo time ($t_{E,0}$) [ms]	0.25	0.72	-	0.25	0.72	-
Subsequent echo time (t_E) [ms]	0.25	0.7	-	0.25	0.7	-
Number of Echoes (NE)	1024	512	-	1024	512	-
Number of scans	128	128	128	128	4	500
Measurement time [min]	3	30	0.7	3	4	3

Moisture Profiles, $T_{2,app}$ and T_1 distributions

The raw MR SPRITE data was processed as follows to achieve the moisture profiles for each column as a function of time: The local image intensity was calibrated using an external reference placed above the sample consisting of 60% (w/w) D_2O and 40% (w/w) H_2O resulting in a simulated moisture content of 0.4. A nominal resolution of 2mm/pixel was set by a field of view (FOV) of 128mm for the 64 pixel primary data. Since the SPRITE measurements for the long column were performed with NS=500 the data was interpolated by means of a spline function as embedded in the R statistical computing environment

(R Development Core Team, 2016). The SE-SPI data was fitted and the final distribution images were generated using a home built data processing routine employed in the MATLAB (Math-Works, Natick, MA) environment, to achieve spatially resolved $T_{2,app}$ distributions. CPMG measurements were processed using an Inverse Laplace algorithm as implemented in the WinDXP (Resonance Instruments Ltd, UK) package and the Winfit (Bruker, Germany) software to obtain bulk $T_{2,app}$ distributions. The T_1 data was processed in an identical fashion as the $T_{2,app}$ data .

Effective Saturation and Relative Evaporation Rate

The effective saturation (Θ) and the relative evaporation rate (e/e_0) for the short silt and sandy loam columns as well as the long sandy loam column were determined gravimetrically every 24 h. Θ was calculated according to Equation 3.4.7 with $\theta_s = 0.9\varepsilon$ [*Rogowski*, 1971] and $\varepsilon = 1 - \rho_B / \rho_{grain}$, where ρ_B is the bulk density and ρ_{grain} , the particle density, is assumed to be 2.65 g cm^{-3} [*Cameron and Buchan*, 2005]. Since the pan evaporation rate (e_0) was found to be constant at 3.9 mm d^{-1} the relative evaporation (e/e_0) was calculated from the daily evaporation of each sample.

Statistical analysis

The coupled model simulated evaporation rates, the 1D moisture profiles and the Richards equation 1D moisture profiles of the 60mm silt and sandy loam columns and the 500 mm sand column were compared to the measured evaporation rates and the NMR determined moisture profiles. The performance of both models was evaluated using the coefficient of determination (r^2), the root-mean-square errors (RMSE) and the coefficient of efficiency (E_f) according to *Nash and Sutcliffe* [1970] with logarithmic values:

$$r^2 = \left(\frac{\sum_{i=1}^{n} (O_i - \overline{O})(P_i - \overline{P})}{\sqrt{\sum_{i=1}^{n} (P_i - \overline{P})^2 \sum_{i=1}^{n} (O_i - \overline{O})^2}} \right)^2 \tag{3.4.19}$$

$$RMSE = \sqrt{\frac{\sum_{i}^{n} (O_i - P_i)^2}{n}} \tag{3.4.20}$$

$$E_f = 1 - \frac{\sum_{i=1}^{n} (\ln O_i - \ln P_i)^2}{\sum_{i=1}^{n} (\ln O_i - \overline{O})^2} \tag{3.4.21}$$

where O and P are the measured and predicted data at time or position i, respectively and $\bar{O}$ is the mean value of the measured data. Using the logarithmic values of O and P for calculating the coefficient of efficiency E_f reduces the oversensitivity to extreme values caused by the mean square error in E [*Krause et al.*, 2005; *Legates and McCabe*, 1999], where the range of E_f lies between 1 and -∞. Higher values of E_f indicate a better agreement, e.g. $E_f = 1$for a perfect fit, $E_f = 0$ indicates that $\bar{O}$ (the observed mean) and the model are equally good and $E_f < 0$ (the mean square error exceeds the variance) indicates that $\bar{O}$ is a better predictor than the model.

4. Results and Discussion

Evolution of the measured Θ and e/e_0

Θ (green cross) and e/e_0 (blue circle) as a function of time are shown in Figure 35 and Figure 36 for the 60 mm sandy loam and silt loam columns, respectively. Instantly after saturation the relative evaporation rate of both soils dropped below the initial value of 1 what is because evaporation from wet soil surfaces not necessarily equals the rate from a free water surface since it is influenced by e.g. the surface roughness, the thermal conductivity, the surface reflectivity (albedo) and the emissivity of a soil. The relative evaporation e / e_0 of the sandy loam stayed declined below 1 during *S1* and *S2* was marked by a sharp decline in e / e_0 down to 0.2 approaching 0.05 at day 11. The effective evaporation rate of the silt loam declined down to 0.7 over the first 3 days followed by a constant rate during *S1* until day 10 marked the onset of *S2* coincided by a decline in e/e_0 down to 0.2 at day 11. Thereafter e/e_0 slowly decreased down to 0.1 until the end of the experiment at day 15. Since both soil columns where evaporated under identical ambient conditions the difference in the

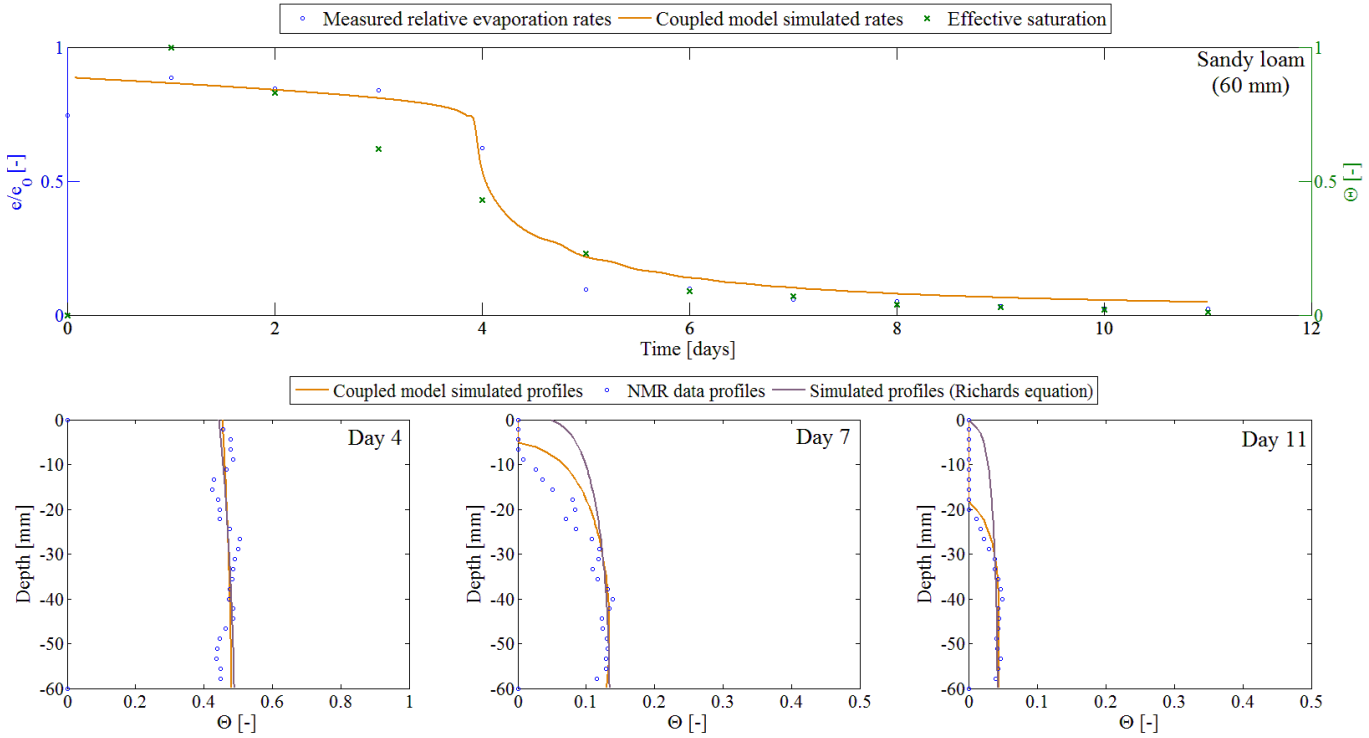

Figure 35. Measured relative evaporation rates e/e_0 (blue circle), the measured effective saturation Θ (green cross) and the coupled model simulated relative evaporation rates e/e_0 (orange line) of the 60 mm sandy loam column (Top). The corresponding measured effective saturation Θ (blue circles) as a function of depth monitored by MR, the coupled model simulated profiles (orange line) and the profiles of the one dimensional Richards equation (purple line) after 4, 7 and 11 days of drying (Bottom).

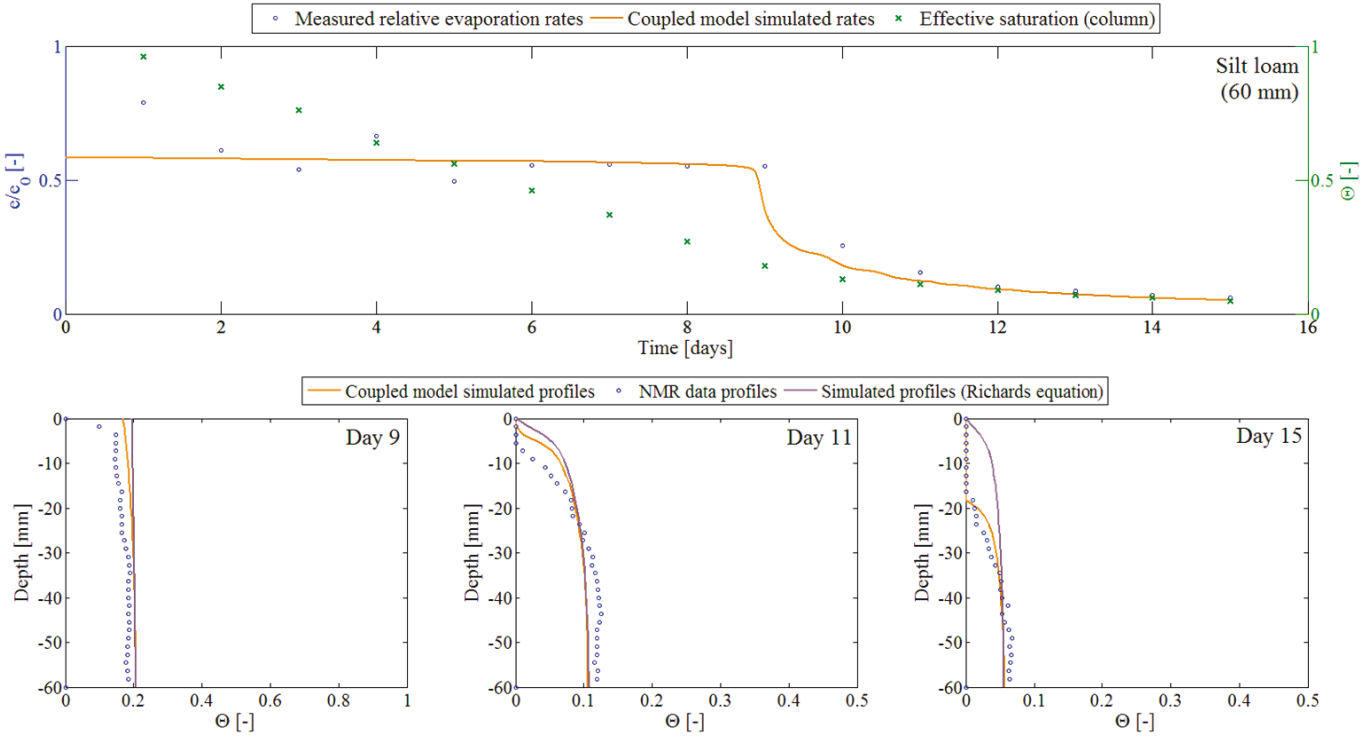

Figure 36. Measured relative evaporation rates e/e_0 (blue circle), the measured effective saturation Θ (green cross) and the coupled model simulated relative evaporation rates e/e_0 (orange line) of the 60 mm silt loam column (Top). The corresponding measured effective saturation Θ (blue circles) as a function of depth monitored by MR, the coupled model simulated profiles (orange line) and the profiles of the one dimensional Richards equation (purple line) after 9, 11 and 15 days of drying (Bottom).

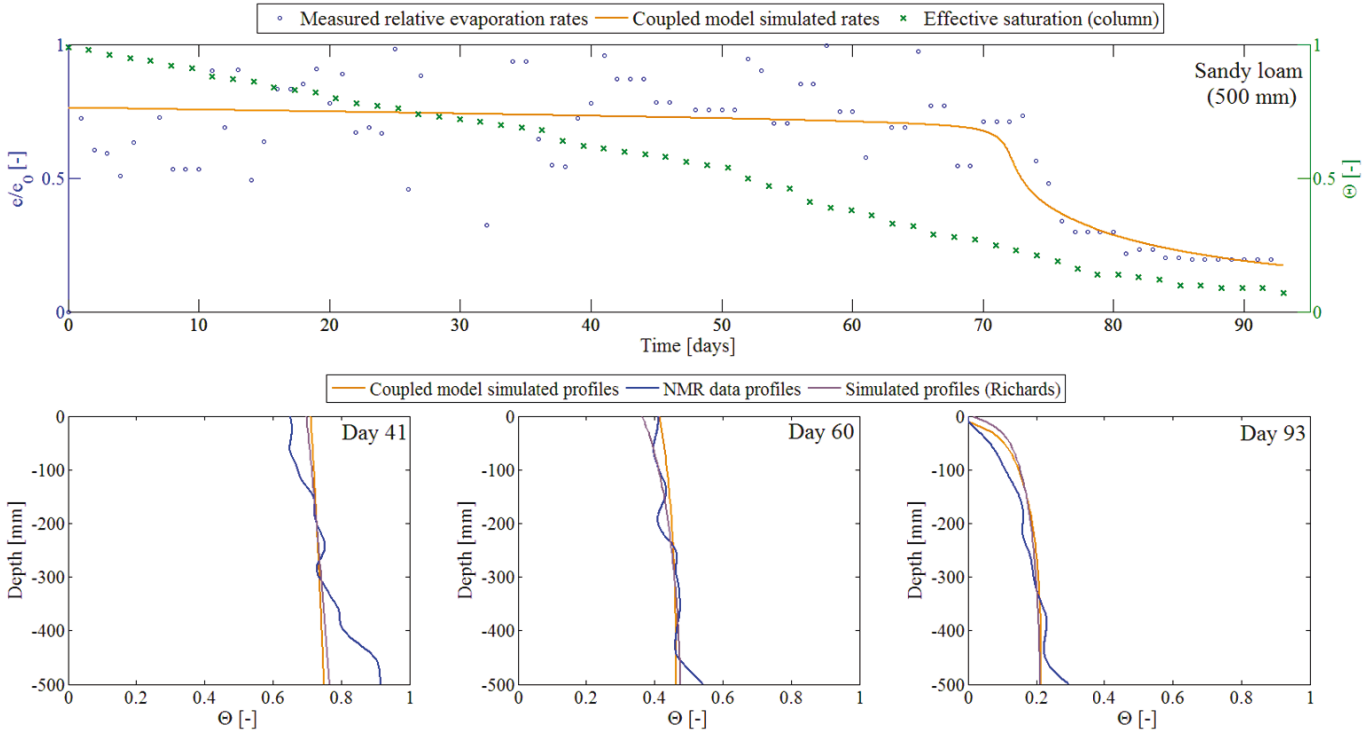

Figure 37. Measured relative evaporation rates e/e_0 (blue circle), the measured effective saturation Θ (green cross) and the coupled model simulated relative evaporation rates e/e_0 (orange line) of the 500 mm sandy loam column (Top). The corresponding measured and spline interpolated effective saturation Θ (blue line) as a function of depth monitored by MR, the coupled model simulated profiles (orange line) and the profiles of the one dimensional Richards equation (purple line) after 41, 60 and 93 days of drying (Bottom).

drying behavior during *S1* was driven by the differences in surface roughness of both soil types since the sandy loam exhibited an evaporation rate enhanced by approximately a factor of 1.3 compared to the silt loam. Since *S2* is also termed "soil controlled stage" parameters such as the pore size distribution (n) and the unsaturated hydraulic conductivity $K(h)$ are controlling to a large extend the moisture depletion of the soil. Therefore, the stronger decline in e/e_0 together with the final approached rate of 0.05 at an early point of *S2* for the sandy loam where this final rate is significantly smaller by a factor of 4 compared to the silt loam at *S2* were caused by mainly the individual soil properties (see Table 5). The effective saturation Θ of both soils declined linear during *S1*, where the duration of this first drying stage was found to be about as twice as long for the silt loam (9 days) compared to the sandy loam (≈ 5 days). At the onset of *S2* the decline of Θ slowed down since the evaporative demand of the atmosphere (the condition inside the climate chamber) could not be sustained by the liquid flow to the soil surface and the liquid continuity ceased. The transition from the *S1* to *S2* evaporation regime occurred at a Θ of 0.09 and 0.13 for the sandy and the silt loam, respectively accompanied with a considerable decline in e/e_0 for both soil types compared to their *S1* rates. The Θ (green cross) and e/e_0 (blue circle) for the 500 mm sandy loam column as a function of time are shown in Figure 37. Due to the temporarily fluctuations in e/e_0 we determined a 7 day average with a mean of 0.75 for e/e_0 and a standard deviation of 0.14 for the *S1* period which lasted for 75 days. From this point e/e_0 constantly declined approaching 0.2 at day 93. Comparing the development of e/e_0 from both sandy loam columns (60 mm and 500 mm) a similar rate for *S1* can be found what indicates that the effective *S1* evaporation rate is not a function of column depth. The effective saturation of the 500 mm sandy loam column Θ declined linearly during the *S1* period. With the onset of *S2* Θ decreased indicating a less sufficient water depletion caused by an increasing dry surface layer. The effective saturation declined down to 0.06 at day 93. For the 500 mm column and both 60 mm columns a linear decline in Θ was found down to the critical moisture content. Thereafter the slope of the effective saturation curve declined, marking the onset of the *S2* evaporation regime. For all samples the decline of Θ was correlated to the drop in the effective evaporation rate.

Comparison of the measured to the simulated coupled model rates e/e_0

The simulated evaporation rates were achieved by adjusting the wind speed such that the evaporation rate of a wet surface equaled the average *S1* evaporation rate for each sample. The simulated relative evaporation rates of the 60 mm sandy and silt loam columns are shown in Figure 35 and Figure 36, respectively (orange line). Comparing the simulated to the measured e/e_0 indicates that the model under predicted the relative evaporation rate of the silt loam during the first 2 days where for the sandy loam the model over predicated the rate only for day one. During *S1* the simulated e/e_0 rates were well predicted for both soil types. The prediction of the duration of *S1* which in turn correlates with the onset of *S2* was only biased

by approximately 0.5 days for both 60 mm columns compared to the measurements. Obviously, the measured data point right after the onset of *S2* is biased most for both soils compared to the prediction of the model. For the silt loam the model under predicts the relative evaporation rate at this point of time whereas it over predicts the rate for the sandy loam. Thereafter the measured rates were in good agreement with the simulations. Considering the statistical analysis as given in Table 7 for e/e_0 the overall evolution of the simulated evaporation rates of the 60 mm sand and silt loam columns agreed well with the measured data. The slightly biased data right after the onset of *S2* might be due to the measurement interval of 24 h^{-1} what indicates that the S2 transition needs to be monitored in high temporal resolution to achieve a significant set of evaporation data. The simulated rates for the 500 mm sandy loam column are given in Figure 37 (orange line). Comparing the 7 day average of $e/e_0 = 0.75$ for the measured relative evaporation rates during *S1* to the simulated rates during the first evaporation stage, a good agreement can be found. The duration of *S1*, what is equal to the onset of *S2* is predicted around day 72 by the model whereas the measured data shows a decline in e/e_0 first on day 75 what is a deviation of 3 days, or considering the overall duration of the experiment, an error of 3%. Nevertheless, considering the relatively small sizes of the columns (compared to lysimeters or field scale measurements) the results of the statistical analysis as given in Table 7 shows a reliable agreement between the measurement data and the coupled model simulates evaporation rates also for the 500 mm sandy loam column. Evaporation measurements performed on soil columns in the laboratory are always biased over field scale measurements since they can be prone to short circuit flow through macropores or preferential flow occurring along the column wall. However, evaporation data taken from lab measurements of different soil types and of various column length scales can be reproduced using a coupled water, heat and vapor flow model approach where reliable results can be obtained even if the measured data is fluctuating and/or of coarse temporal resolution. Since based on our statistical analysis the measured evaporation rates are in good agreement with the coupled model predicted rates we used this setup to simulate the moisture profiles for the 60 mm sandy and silt loam columns and the 500 mmm sandy loam column during drying.

Table 7. Calculated performance criteria of the correspondence between: i) the measured relative evaporation rates e/e_0 and the simulated rates using a coupled water, heat and vapor flow model ii) the effective saturation Θ profiles determined by means of MR and the coupled model simulated vertical Θ profiles iii) the effective saturation Θ profiles determined by means of MR and the vertical one dimensional Richards equation Θ profiles.

		Silt loam (60 mm)				Sandy loam (60 mm)				Sandy loam (500 mm)			
			Day				Day				Day		
		e/e_0	9	11	15	e/e_0	4	7	11	e/e_0	41	60	93
Coupled	ln E	0.96	-1.29	0.51	0.81	0.90	-0.12	0.34	0.90	0.81	0.21	0.53	0.92
Model	R^2	0.95	0.94	0.94	0.96	0.99	0.45	0.94	0.98	0.78	0.94	0.82	0.94
	RMSE	0.076	0.03	0.02	0.007	0.048	0.08	0.02	0.003	0.17	0.07	0.02	0.03
Richards	ln E		-2.86	-115.0	-264		-0.4	-911	-322		0.38	0.65	0.29
equation	R^2		0.92	0.84	0.84		0	0.04	0.05		0.94	0.84	0.94
	RMSE		0.034	0.083	0.12		0.026	0.35	0.4		0.07	0.02	0.06

Moisture profiles monitored by MR

The MR moisture data are computed as effective saturation Θ according to Equation 3.4.7. Figure 35 and Figure 36 show the measured Θ as a function of depth for the 60 mm sandy and silt loam columns, respectively (blue circle). For each column 3 representative plots at different stages of desaturation are given, where the effective saturation close to the onset of *S2*, 2 days after the transition from *S1* to *S2* and at the final stage of the experiment (6 days after the onset of *S2*) are displayed. Generally, comparing the shape of the profiles from both 60 mm columns it is obvious the packing of the silt loam was more homogeneously compared to the sandy loam what causes slight fluctuations in the Θ profile. Nevertheless, these deviations do not impact the drying behavior of the soil to a large extend, also these heterogeneities can be found frequently on the field scale. Based on the Θ profiles the water inside both columns was virtually homogeneously distributed until the onset of *S2*. Thereafter, a gradient in moisture developed from the bottom up to the evaporation front which was now located inside the soil instead at the soil surface and is therefore termed "secondary evaporation front". For both columns the moisture gradient extended from $\Theta = 0.1$ at the bottom to $\Theta = 0$ at the secondary evaporation front, which was located at a depth of 10 mm and 5 mm for the sandy and the silt loam, respectively 2 days after the onset of *S2*. The extend of the dry surface layer of the sandy loam at this point was already twice as large compared to the silt loam what was mainly driven by n and $K(h)$. These differences reflect themselves in the trend of e/e_0 for both 60 mm soil columns after the onset of *S2* since the extending dry subsurface layer increases the resistance to evaporation as it increases the diffusion path lengths for water vapor. The relative evaporation rate of the sandy loam therefore approached the final value relatively short after the onset *S2* stage compared to the silt loam. As drying proceeded the moisture gradient of both columns decreased by the factor of 2 where Θ stays constant at 0.5 from the bottom of both columns up to a depth of approximately 35 mm followed by a linear decrease in Θ approaching the secondary evaporation front. At the final stage of the experiments the secondary evaporation front was pinned at a depth of 20 mm for the sandy and the silt loam, respectively. The equal extend of the dry subsurface layer for both columns monitored at the final stage of the experiment can be explained with the early development of the layer for the sandy loam since evaporation was more restrained what led to an equally receding secondary evaporation front depth as a function of time. As it is shown in Figure 37, Θ profiles of the 500 mm sandy loam column are given for two temporally different *S1* stages and for the final stage of the experiment after 93 days (blue line). At day 41 a gradient in Θ across the column varying from $\Theta = 0.9$ at the bottom of the column to $\Theta = 0.7$ at the surface developed, where the minor fluctuations in Θ were caused by the packing of the soil. After 60 days of drying the gradient disappeared and no significant gradient or bias in Θ as a function of depth

was monitored. A mean effective saturation of ~ 0.45 was monitored at this stage of drying. Comparing the Θ profiles of the 60 mm and the 500 mm sandy loam column monitored during *S1*, both exhibit similar slight fluctuations in Θ as a function of depth caused by the packing of the soil what in turn is driven by the soil composition (see Table 5). The transition to the *S2* evaporation regime occurred shortly before day 93 since the dry subsurface layer was monitored to be around 10 mm in thickness at his time. For both, the 60 mm and the 500 mm sandy loam column a pronounced gradient pinned to the secondary evaporation front was monitored where the gradient of the 500 mm column extend from Θ = 0.3 at bottom to 0.2 at a depth of 150 mm where Θ declined much steeper from this point up to 10 mm depth, where the secondary evaporation front was located at this point of time. No correlation was found between the length of the column and the duration of the first stage of evaporation, considering an identical e/e_0 of ~ 0.75 for both columns during *S1*. Further, the extend of the gradient in Θ as a function of depth around the onset of *S2* is not a function of e/e_0 during the second stage of drying since the relative evaporation rates of the 60 mm and the 500 sandy loam column were found to be both e/e_0 = 0.2.

Comparison of $\Theta_{measured}$ and $\Theta_{simulated}$

The moisture profiles corresponding to the simulated evaporation rates were plotted as effective saturation Θ vs. depth. Figure 35 – 37 show the coupled model simulated vertical Θ profiles (orange line) and the simulated profiles using the Richards approach (purple line) for the 60 mm and 500 sandy and silt loam column, respectively. Generally, a positive trend in the coupled model results compared to the MR data can be observed towards progressing desaturation for all columns, also evident in the statistical relevant parameters E_f, R^2 and the *RMSE* as shown in Table 7. During *S1* evaporation a slightly lower Θ as a function of column depth is found for the MR data compared to the coupled model predicted profiles. Around the onset of *S2* evaporation the vertical gradient in Θ from the secondary evaporation front downwards the column bottom as predicted by the coupled model was less pronounced for the 60 mm silt loam in comparison to the MR data. For the 60 mm sandy loam the Θ gradient was well predicated by the coupled with no significant bias. The coupled model simulated profiles for 500 mm sandy loam column are shown in Figure 37 (orange line). For day 41 the steepness of the measured gradient in Θ is not reproduced by the coupled model, whereas after 60 days of drying the gradient disappeared what is reflected in an increasing E_f and decreasing *RMSE* (Table 7). At day 93 the coupled model a slightly higher effective saturation Θ compared to the MR data, with a particularly bias in the range of 150 mm up to 10 mm of depth. This is a trend opposed to the findings for the 60 mm silt and sandy loam columns, where the coupled model predicted profiles did reflect the strong moisture gradient from the column bottom to the secondary evaporation front. Nevertheless, according to the statistical analysis for the 500 mm sandy loam

column the best agreement between the coupled model predicted Θ profiles and the MR data was achieved after 93 days of drying.

Since the one dimensional Richards equation is commonly used to describe water flow in unsaturated soils, we compared the high spatially resolved MR data to the simulated Θ profiles using the Richards approach particularly focusing on moisture content changes in the topmost layer after the onset of *S2*. For each of the columns the Richards profiles are given in Figure 35 – 37 (purple line). At the first stage of drying for all columns the simulated Θ profiles using the Richards approach were minor biased compared to the coupled model profiles. During progressing desaturation the bias between the Θ profiles of the Richards approach and the coupled model got more pronounced with larger deviations in the uppermost part of each column, where the gradient in Θ developed more strongly. This trend continues since the Richards approach doesn't count for vapor and heat transport and therefore cannot reproduce the dry surface layer under *S2* conditions. At the final stage of the experiment the differences in the absolute water content (given in mm or liter/m²) above the drying front were 13 mm for the 60 mm silt loam and 18 mm for the 60 mm sandy loam column, what is an overall deviation between the Richards approach and the MR data of ~ 50% compared to the initial saturation. For the 500 mm sandy loam column the overall deviation in water above the dry layer at 93 days of drying was ~ 16% what corresponds to an absolute water content of 26 mm. As shown in Table 7 all statistical coefficients deteriorated with progressing desaturation, with particularly strong negative values in E_f for the 60 mm columns. The overall trend for the Richards approach to larger deviations with progressing desaturation of the soil and the strong bias in moisture content for the topmost soil layer clearly demonstrates that accurate moisture profiles are only achievable if vapor and heat flow are considered besides liquid water flow.

T_1 and $T_{2,app}$ Distributions during drying

T_1 distribution and mean log T_1

Water in soils is confined in voids, pore throats and grain surfaces what considerably chances the relaxation behavior of water molecules compared to the neat liquid. A profound method to study confined water dynamics (e.g. pore sizes) are T_1 and $T_{2,app}$ relaxation time measurements. Since T_1 describes the spin-lattice relaxation, where the values of T_1 get shorter if the range of the molecular tumbling rates gets narrow and therefore close to the Larmor frequency, what in turn indicates restricted water. Figure 38 shows the integral T_1 and $T_{2,app}$ relaxation time distributions of the IR and CPMG MR data (8.5 MHz) for the 60 mm silt and sandy loam columns (whole column) over time. Since the 500 mm sandy loam column was monitored using the 2.2 MHz apparatus with a sensitive spot of 50 mm in length, the integral T_1 and $T_{2,app}$

relaxation time distributions are given in 10 subsequent plots with each plot representing a measured soil volume of 43 cm³ (Figure 39).

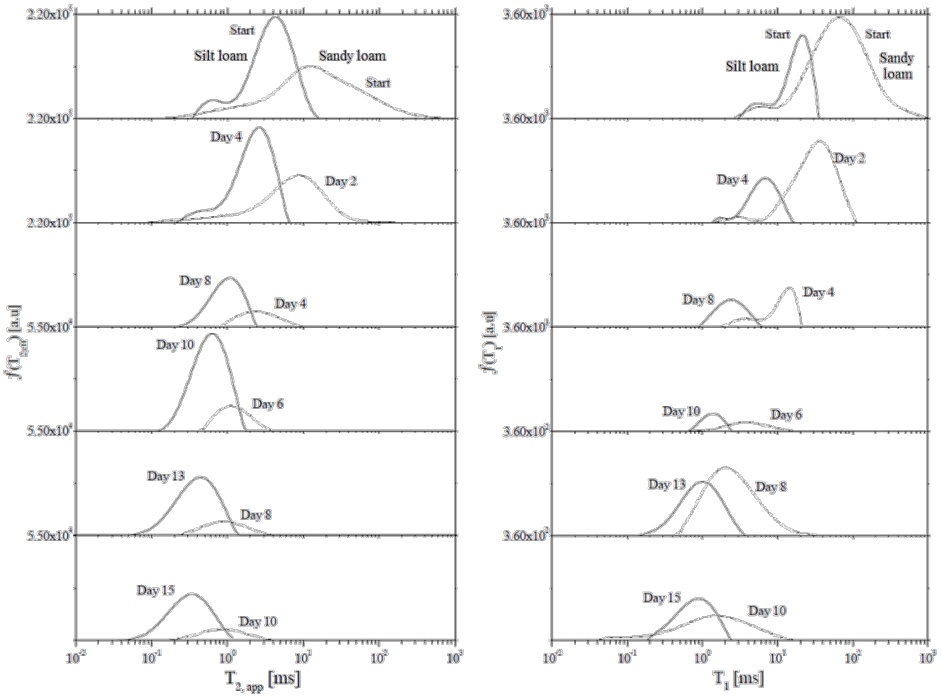

Figure 38. $T_{2,app}$ (left) and T_1 (right) relaxation time spectrum (measured at 8.5 MHz) for the 60 mm silt loam (line) and sandy loam (dotted line) columns as a function of drying time. The $T_{2,app}$ and T_1values were determined by means of a bulk CPMG and IR method, respectively.

For all columns the relaxation time spectrum shows a bimodal distributed logarithmic T_1 under saturated conditions, attributed to a fast exchange of the spins with their surroundings (fast mode) and a comparatively slower exchange (slow mode). During desaturation a trend in the overall T_1 logarithmic mean towards faster relaxation was observed for all columns where the fast mode vanished at the onset of *S2*. The mean log T_1 of the 60 mm silt loam shifted from 10 ms (saturation) to ~ 1ms (*S2*) with a constantly decreasing amplitude of the overall T_1 distribution until day 15. The mean log T_1 of the 60 mm sandy loam shifted rapidly from 70 ms (saturation) to 4 ms (onset of *S2*) followed by a sharp shift to ~2ms which was not observable for the silt loam. Comparing the mean log T_1 and the amplitude of the relaxation time distributions of both 60 mm columns, the mean log T_1 of the sandy loam decreased from a factor of 7 under saturation to a factor of 4 at the final stage of the experiment. These differences are driven by the pore

size distribution (n) of both soils, where an increasing sand content is coincided with an increasing longitudinal relaxation time T_1 since the overall pore size distribution narrows (larger n). Furthermore, because the rate of decrease in water content, described by the desaturation coefficient (α), is strongly related to n and increases with sand content, the differences in n α of both soil types causes the shift in T_1 after the onset of *S2* what can be seen as an abrupt desaturation of pores equal in size.

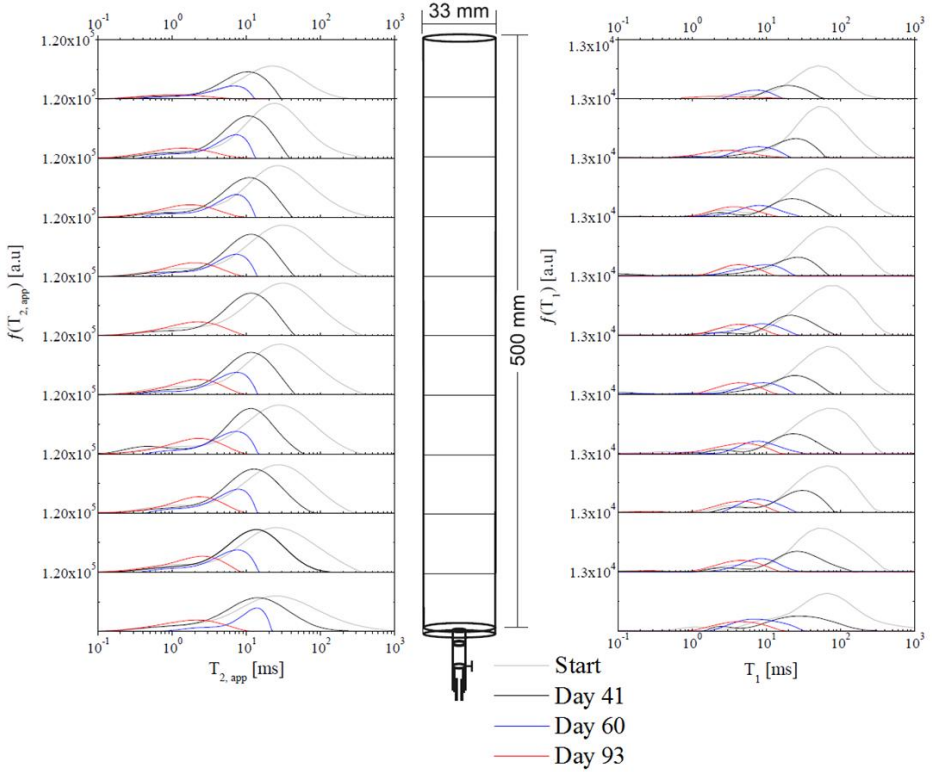

Figure 39. $T_{2,app}$ (left) and T_1 (right) relaxation time spectrum (measured at 2.2 MHz) for the 500 sandy loam column as a function of drying time. The $T_{2,app}$ and T_1values were determined in by means of a bulk CPMG and IR method, respectively.

For the 500 mm sandy loam column all measurements where performed using the 2.2 MHz magnet. Since T_1 relaxation times are logarithmically dependent on the Larmor frequency [*Korb and Bryant*, 2002] the absolute mean log T_1 value is slightly slower compared to the 60 mm sandy loam column. Under satura-

tion a mean log T_1 of 65 ms was found, not significantly changing as a function of depth with a fast mode ~ 3ms. After 41 days of drying the distribution spectrum shifted to faster values with a decreasing mean log T_1 of ~20 ms, where the fast mode disappeared in the topmost layer of the column (first 50 mm) and vanished completely after 60 days. This stage of desaturation was characterized by a mean log T_1 of ~ 7 ms with no significant shift over depth. At the final stage of the experiment after 93 days of drying the T_1 distribution shifted significantly to faster values with a mean log T_1 of: ~ 1 ms for the first 50 mm, ~ 2ms for the next two subsequent volumes (100mm and 150 mm) and ~ 5 ms from 150 mm depth to the column bottom. Comparing the evolution of the overall T_1 distribution and the log mean of the 60 mm and 500 sandy loam columns an identical behavior down to lower water contents was found what showed that T_1 as a function of drying time does not depend on the extend of the soil profile.

$T_{2,app}$ bulk distribution and spatially resolved $T_{2,app}$

It is well known that the distribution of T_2 times is directly correlated to the absolute pore size distribution of a porous medium [*Haber-Pohlmeier et al.*, 2014; *Stingaciu et al.*, 2010] provided the fast diffusion assumption and a known surface relaxivity what is still a challenging field to investigate [*Duschl et al.*, 2015]. Additionally, according to Equation 3.4.1 the influence of higher modes of the MR signal (faster decaying components) such as diffusion and susceptibility driven decays is assumed to be neglectable.
As it is shown in Figure 38 under saturation the 60 mm silt loam column shows a bimodal $T_{2,app}$ distribution with a slow and fast mode ~ 4 ms and ~0.6 ms, respectively , whereas a broad range of $T_{2,app}$ from 0.1 ms to 200 ms can be found for the 60 mm sandy loam column with no distinct slow and fast mode. At the onset of *S2* the fast mode of the silt loam vanished and the overall distribution of both soils narrowed. Thereafter only the amplitude of the distribution decreased with a log mean $T_{2,app}$ of ~ 0.6 ms for the silt loam and ~1 ms for the sandy loam.
T_2 relaxation times are less affected by the Larmor frequency but nevertheless some minor influence on $T_{2,app}$ is observable between the 2.2 MHz and the 8.5 MHz magnet. Therefore, the mean log $T_{2,app}$ of the 500 mm sandy loam column is slightly shifted towards slower relaxation times. Under saturated conditions a broad distribution can be found ranging from ~0.1 ms to ~200 ms, identical to the 60 mm sandy loam column. With progressing desaturation $T_{2,app}$ shifted uniformly over depth until the onset of *S2* similar to the 60 mm column. Thereafter, a difference in mean log $T_{2,app}$ of ~ 1 ms between the first 50 mm and the other compartments was found indicating a dry subsurface layer and the development of an migrating secondary evaporation front. Comparing the bulk $T_{2,app}$ distributions of the 60 mm and 500 mm sandy loam columns, both show an identical shift in the distribution towards faster relaxation with progressing desaturation.

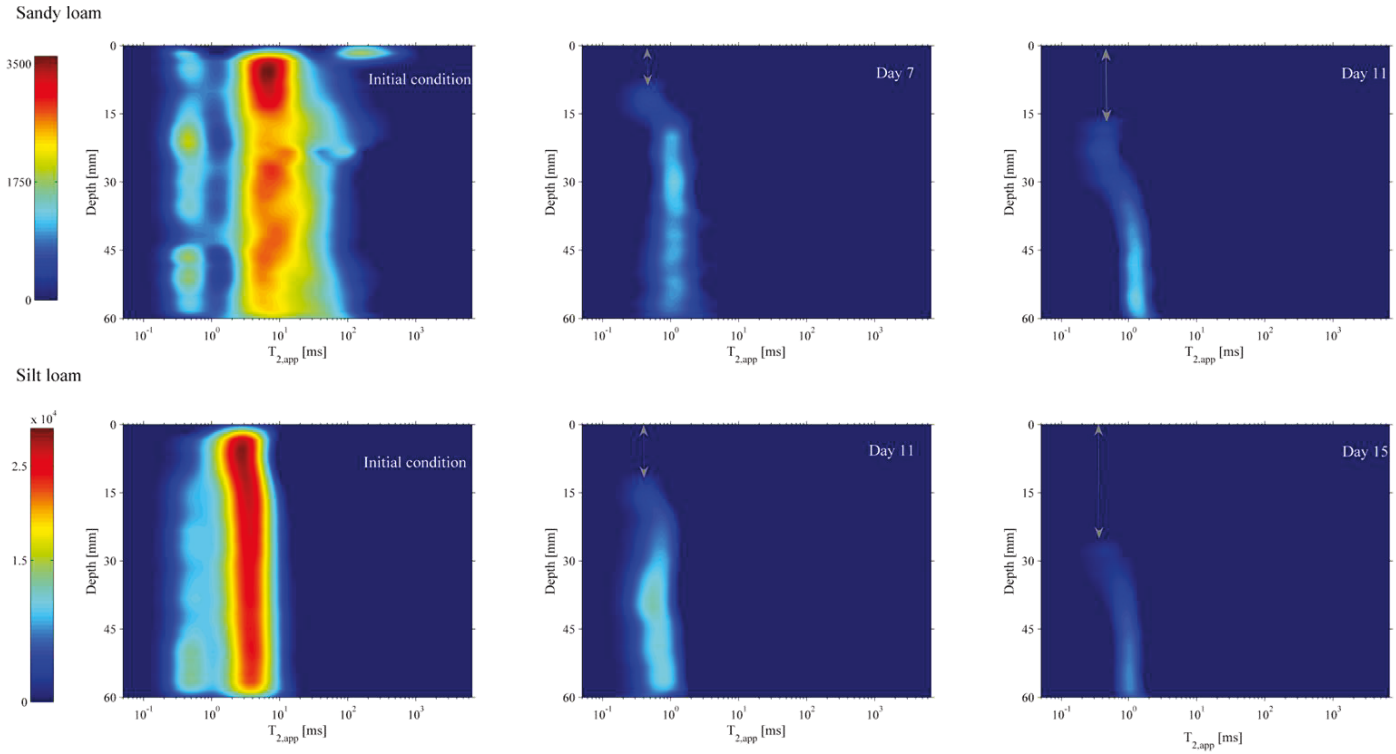

Figure 40. *T2,app* relaxation time spectrum as a function of drying time of the 60 mm sandy loam (top) and silt loam (bottom) columns monitored at 8.5 MHz by means of SE-SPI with a resolution of 2mm/pixel.

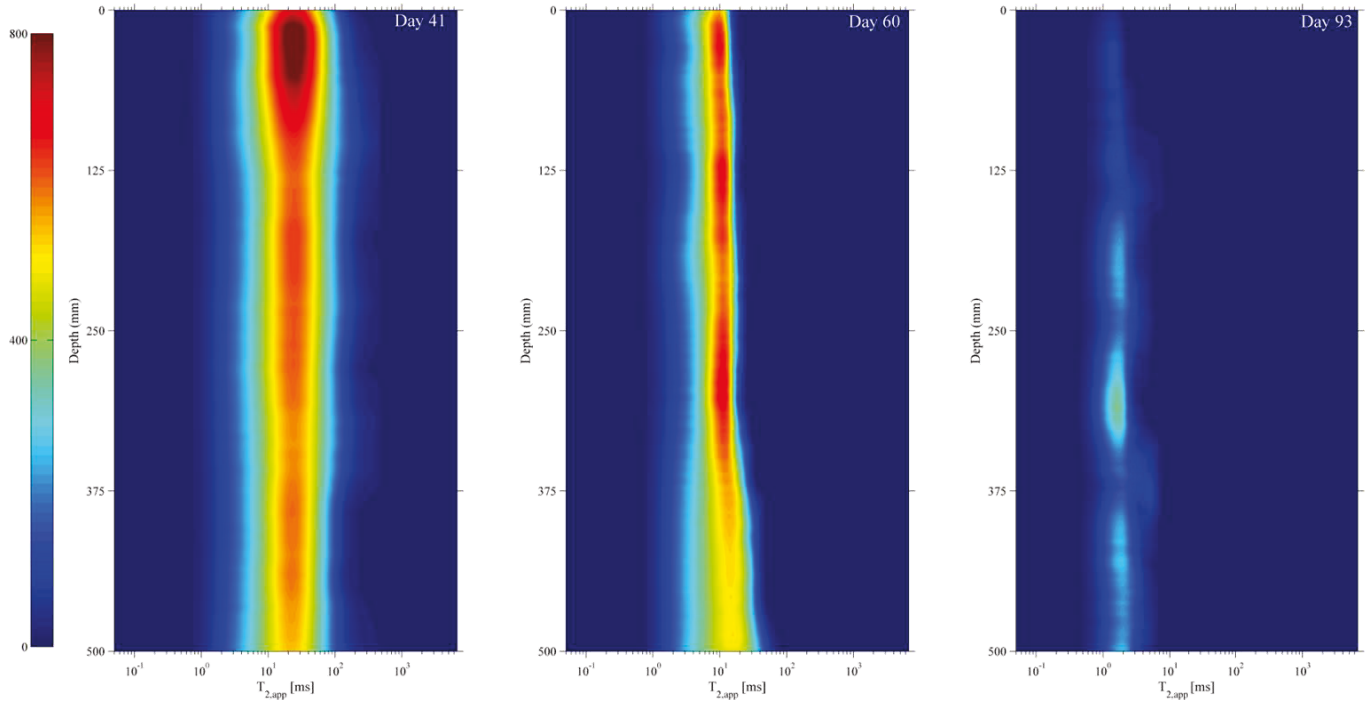

Figure 41. *T2,app* relaxation time spectrum as a function of drying time of the 500 mm sandy loam column monitored at 2.2 MHz by means of SE-SPI with a resolution of 2mm/pixel.

Since CPMG measurements commonly yield bulk distributions, we additionally monitored $T_{2,app}$ as a function of column depth. Figure 40 shows the $T_{2,app}$ distributions for the 60 mm sandy and silt loam at saturation, after the onset of *S2* and at the final stage of the experiment. Under initial saturation both columns show a strong bimodal distribution which is not reflected in the bulk measurement of the sandy loam. This might be due to the regularization function of the Inverse Laplace algorithm since the range of $T_{2,app}$ is found to be identical for both measurements. Two days after the onset of *S2* the bimodal behavior in the $T_{2,app}$ distribution vanished and the overall distribution narrows coincided with a shift towards faster relaxation times with a mean log $T_{2,app}$ of ~ 1 ms and ~ 0.6 ms for the 60 mm sandy and silt loam columns, respectively. A distinct dry surface layer (grey arrow) of 7 mm (sandy loam) and 10 mm (silt loam) in thickness was found for both 60 mm columns (Figure 40). Below the location of the secondary evaporation front a gradient in the $T_{2,app}$ distribution similar to the gradient in Θ indicates that water was predominantly located in smaller pores along with strongly bounded water at the grain boundaries (film water). For the subsurface layer this trend continued until the final stage of the experiment. Surprisingly, a slightly opposed trend in the mean log $T_{2,app}$ was observed for the bottom of both 60 mm columns. After the onset of *S2* the mean log $T_{2,app}$ stayed constant at the location of the secondary evaporation front but decreased down to slower relaxation times at the bottom of the column. This effect might be driven by a condensation process at the bottom layer of the column, where larger pores were reloaded with what led leading to slower $T_{2,app}$. Figure 41 shows the spatially resolved $T_{2,app}$ distribution of the 500 mm sandy loam column after 41, 60 and 93 days of drying. After 41 days of drying all pores in the range of *n* were saturated sufficiently since no gradient was found in the $T_{2,app}$ distributions. This further indicates that the moisture along the soil profile is still homogenous distributed even with strong gradient in Θ as shown in Figure 37. As water depletion continued, the overall $T_{2,app}$ distribution narrowed with a corresponding mean log $T_{2,app}$ of ~ 8 ms, where a slightly broader $T_{2,app}$ distribution from 500 mm to ~315 mm was found for day 60. At the final stage of the experiment after 93 days the overall distribution narrowed coincided with decreasing signal amplitudes driven by a decreasing Θ. A log mean $T_{2,app}$ of ~ 2 ms which increased to ~ 1 ms from a depth of ~ 100 mm to the surface of the column. Within this range the overall distribution was narrowed compared to the lower part of the column indicating water in small pores and film water at the grain surfaces. Even if the $T_{2,app}$ signal amplitude significantly decreased towards the surface of the 500 sandy loam column on a secondary evaporation front cannot be found. This might be due to the small extend of the front at this stage of around 10 mm where the water content of the boundary layer (relative humidity) is still in balance with the vapor inside the dry layer what led to a detectable signal in the SE-SPI measurements. Further, these phenomena could be due to the regularization procedure of the Inverse Laplace algorithm since the signal was almost decayed at this position after 93 days of drying. Comparing the $T_{2,app}$ distributions achieved shortly after the onset of *S2* of the 60 mm (Figure 40, day 7)

and 500 mm (Figure 41, day93) sandy loam columns an identical pattern in the distribution functions was found. Despite the differences in the absolute log mean $T_{2,app}$ driven only by the differences in Larmor frequency of the instruments (assuming an identical t_E), both columns showed an identical distribution in the range of 0.6 ms to 7 ms for the lower part of the soil profile. Towards the secondary evaporation front the overall distribution narrows as the overall amplitude decreased. However, the gradient pinned to the evaporation front wasn't clearly observable for the 500 mm column.

5. Summary and Conclusions

In the presented study, we monitored the evaporative drying over time of three different soil columns by means of various Magnetic Resonance methods. The effective saturation profiles of each column were compared to the one dimensional Richards approach and vertical profiles achieved using a numerical liquid water, vapor and heat flow model. Results clearly demonstrate the feasibility of ^{1}H-MR methods such as the $T_{2,app}$ distribution in combination with the signal amplitude to monitor the drying process of different soils at the lab scale. Distinct evaporation stages with the development of a dry topmost layer extending over time could be monitored for both types of soil and no correlation between the extent of the soil profile and the drying behavior was found. The numerical coupled model approach clearly demonstrated the need to consider heat and vapor flow additively to solely water flow as the one dimensional Richards equation assumes, what can lead to overestimations in water content up to 50 % compared to the initial saturation. The statistical parameters showed a good agreement between the coupled model and the MR data particularly in the Nash-Sutcliffe efficiency down to lower moisture contents. Although, lab scale measurements are considered to be more effected from soil disturbance and preferential flow caused by possible anisotropies our results clearly showed no influence on the drying behavior and moisture development over time. Nevertheless, since all soil parameters were derived by means of the HYPROP evaporation method, the achieved parameters might be biased [*Schindler et al.*, 2010b] what might have affected the modeling results. Surprisingly, for the 60 mm sandy loam and silt loam columns a shift back to slower $T_{2,app}$ times was found at the columns bottom at the final stage of the experiment what could be caused by downward directed vapor flow. Increasing temperatures at the top of the column due to the extending dry subsurface layer increased vapor pressure and thus the matric potential. Therefore, water started to move to the colder bottom, what in turn increased the water content at the colder bottom. Water then refills larger pores or forms liquid films at grain boundaries what led to larger $T_{2,app}$.

As future perspective, the MR methods used in this study can be employed on mobile MR devices, e.g. the NMR MOUSE, to monitor moisture content as function of space and time in the top layer of soils directly in the field to link lab scale investigations to field scale measurements.

IV. Synthesis

1. Final Conclusions

Magnetic resonance (MR) proved to be a feasible method to monitor evaporation driven moisture changes in soils at the lab scale non-invasively in high spatial resolution. For medium sand as a model system high-field and unilateral MR methods allow for quantitative moisture monitoring as a function of time and to follow the origin and migration of the secondary evaporation front inside the soil profile. Monitoring an evaporating silt loam on an intermediate scale the concept of the mobile unilateral MR sensor was shown to be a promising tool for quantifying moisture changes in high resolution with perspective for field scale measurements. Since superconducting magnets are not applicable for field measurements, single sided and Halbach magnets can be applied where certain methods allow not only the quantification of soil moisture non-invasively and in high resolution but also the saturation degree as a function of pore size distribution.

Even though field methods involve larger volumes of soil and are therefore usually considered more realistic compared to laboratory methods which can be prone to marcopore flow or flow along the core wall, it is essential to investigate pore scale processes since they are the origin of heterogeneities in soil moisture on the field scale. Using radiation data together with the measured evaporation rate and the soil hydraulic parameters of a silt loam and a sandy loam as input parameters for a coupled water, vapor and heat flow model, we showed that pore scale moisture dynamics achieved at the lab scale using various MR techniques in combination with different MR methods are in sufficient agreement with the model output. Therefore, high-resolution MR data can be used to evaluate soil moisture models also on the field scale if applied as a grid of measurement points.

Moisture dynamics of bare soils exposed to evaporation is a challenging process to model since it involves heat and vapor flow in addition to liquid water transport where vapor and heat transport become more pronounced with progressing desaturation. The high resolution MR data was used together with the analytical derived moisture profiles of a coupled water, vapor and heat flow model to show that after the onset of *S2* evaporation moisture content predicted by the common Richards approach which is based solely on liquid water transport becomes strongly biased in the topmost layer of the soil. This may have considerable influence on remote sensing of soil temperatures, water contents and derived quantities like evaporation.

Summarizing, the results presented in this thesis showed that well-chosen MR techniques in combination with feasible methods are a valuable tools for providing quantitative, volumetrically averaged or spatially resolved information about soil moisture dynamics from sandy soils to clays during evaporation. The technique further allows to conclude implicitly on pore size saturations and distributions. Using the high resolution MR data to validate a coupled water, vapor and heat flow model showed that moisture dynamics of bare topmost soil layers under evaporative conditions clearly proceeds in two distinct stages, where the expanding dry subsurface layer restrains evaporation.

2. Outlook

As it was demonstrated in this thesis MR can be used to quantify moisture dynamics for a broad range of soil types exposed to evaporation. Since MR field measurements are not trivial in terms power supply, SNR, penetration depth, etc. feasible MR concepts and methods need to be constantly developed and tested under laboratory conditions. Until today the most common methods for soil moisture measurements directly at the test site do not or rarely involve gradient based methods which allow high spatial resolution, moisture imaging or anisotropic diffusion measurements. However, considering the latest development, e.g. single sided sensors can be equipped with gradient systems, field maps of local soil physical parameters, soil hydraulic permeability and dual permeability are achievable. These parameters can serve as a parametric uplink from local soil properties to field scale modeling in order to improve water-energy transfer simulations between the land surface and the atmosphere.

References

Abtew, W., and A. Melesse (2013), Evaporation and Evapotranspiration Measurement, in *Evaporation and Evapotranspiration*, edited, pp. 29-42, Springer Netherlands.

Amin, M. H. G., R. J. Chorley, K. S. Richards, B. W. Bache, L. D. Hall, and T. A. Carpenter (1993), Spatial and temporal mapping of water in soil by magnetic resonance imaging, *Hydrological Processes*, *7*(3), 279-286.

Amin, M. H. G., R. J. Chorley, K. S. Richards, L. D. Hall, T. A. Carpenter, M. Cislerova, and T. Vogel (1997), STUDY OF INFILTRATION INTO A HETEROGENEOUS SOIL USING MAGNETIC RESONANCE IMAGING, *Hydrological Processes*, *11*(5), 471-483.

Andreev, S. V., and B. K. Martens (1960), Soil Moisture Determination by the Method of Nuclear Magnetic Resonance, *Soviet Soil Sci*, *10*(Ref. Oct.), 1129-1133.

Assouline, S., S. W. Tyler, J. S. Selker, I. Lunati, C. W. Higgins, and M. B. Parlange (2013), Evaporation from a shallow water table: Diurnal dynamics of water and heat at the surface of drying sand, *Water Resour Res*, *49*(7), 4022-4034.

Balcom, B. J., J. C. Barrita, C. Choi, S. D. Beyea, D. J. Goodyear, and T. W. Bremner (2003), Single-point magnetic resonance imaging (MRI) of cement based materials, *Mat. Struct.*, *36*(3), 166-182.

Barrie, P. J. (2000), Characterization of porous media using NMR methods, in *Annual Reports on NMR Spectroscopy*, edited, pp. 265-316, Academic Press, Cambridge, MA.

Behroozmand, A., K. Keating, and E. Auken (2015), A Review of the Principles and Applications of the NMR Technique for Near-Surface Characterization, *Surv Geophys*, *36*(1), 27-85.

Belhamri, A. (2003), Characterization of the First Falling Rate Period During Drying of a Porous Material, *Drying Technology*, *21*(7), 1235-1252.

Bernstein, M., K. King, and X. Zhou (2004), *Handbook of MRI Pulse Sequences*, Academic Press, Burlington, Mass.

Bird, N. R. A., A. R. Preston, E. W. Randall, W. R. Whalley, and A. P. Whitmore (2005), Measurement of the size distribution of water-filled pores at different matric potentials by stray field nuclear magnetic resonance, *European Journal of Soil Science*, *56*(1), 135-143.

Bittelli, M., F. Ventura, G. S. Campbell, R. L. Snyder, F. Gallegati, and P. R. Pisa (2008), Coupling of heat, water vapor, and liquid water fluxes to compute evaporation in bare soils, *Journal of Hydrology*, *362*(3–4), 191-205.

Bloch, F. (1946), Nuclear induction, *Physical review*, *70*(7-8), 460.

Bluemich (2005), Essential NMR for scientists and engineers.

Blümich, P. Blümler, G. Eidmann, A. Guthausen, R. Haken, U. Schmitz, K. Saito, and G. Zimmer (1998), The NMR-mouse: construction, excitation, and applications, *Magnetic Resonance Imaging*, *16*(5–6), 479-484.

Blümich, B., S. Haber-Pohlmeier, and W. Zia (2014), *Compact NMR*.

Brooks, R. H., and A. T. Corey (1964), Hydraulic properties of porous media, *Hydrology Paper No. 3 Civil Engineering Dept., Colorado State Univ., Fort Collins, CO*.

Brutsaert, W. (1982), *Evaporation into the Atmosphere: Theory, History and Applications*, Springer Netherlands.

Buck, A. L. (1981), New equations for computing vapor pressure and enhancement factor, *Journal of Applied Meteorology*, *20*(12), 1527-1532.

Callaghan, P. T. (1993), *Principles of nuclear magnetic resonance microscopy*, Clarendon Press Oxford.

Camaiti, M., V. Bortolotti, and P. Fantazzini (2015), Stone porosity, wettability changes and other features detected by MRI and NMR relaxometry: a more than 15-year study, *Magnetic Resonance in Chemistry*, *53*(1), 34-47.

Cameron, K. C., and G. D. Buchan (2005), Porosity and Pore Size Distribution, in *Encyclopedia of Soil Science, Second Edition*, edited, CRC Press, Boca Raton.

Carr, H. Y., and E. M. Purcell (1954), Effects of diffusion on free precession in nuclear magnetic resonance experiments, *Physical Review*, *94*(3), 630.

Casanova, F. (2011), *Single-Sided NMR*, Springer, Berlin Heidelberg.

Cass, A., G. S. Campbell, and T. L. Jones (1984), Enhancement of Thermal Water Vapor Diffusion in Soil1, *Soil Science Society of America Journal*, *48*(1), 25-32.

Chang, C. T. P., A. T. Watson, and C. M. Edwards (1999), NMR Imaging of Fluids and Flow in Porous Media, in *Experimental Methods in the Physical Sciences*, edited by W. Po-zen, pp. 387-423, Academic Press.

Chung, S.-O., and R. Horton (1987), Soil heat and water flow with a partial surface mulch, *Water Resour Res*, *23*(12), 2175-2186.

Coates, G. R., L. Xiao, and M. G. Prammer (1999), *NMR logging: principles and applications*, Haliburton Energy Services.

Coussot, P. (2000), Scaling approach of the convective drying of a porous medium, *Eur. Phys. J. B*, *15*(3), 557-566.

Dai, A., K. E. Trenberth, and T. R. Karl (1999), Effects of Clouds, Soil Moisture, Precipitation, and Water Vapor on Diurnal Temperature Range, *Journal of Climate*, *12*(8), 2451-2473.

De Vries, D. A. (1958), Simultaneous transfer of heat and moisture in porous media, *Eos, Transactions American Geophysical Union*, *39*(5), 909-916.

Desborough, C. E., A. J. Pitman, and P. Iranneiad (1996), Analysis of the relationship between bare soil evaporation and soil moisture simulated by 13 land surface schemes for a simple non-vegetated site, *Global and Planetary Change*, *13*(1–4), 47-56.

Deurer, M., I. Vogeler, A. Khrapitchev, and D. Scotter (2002), Imaging of Water Flow in Porous Media by Magnetic Resonance Imaging Microscopy, *Journal of Environmental Quality*, *31*(2), 487-493.

Dunn, K. J., D. J. Bergman, and G. A. LaTorraca (2002), *Nuclear magnetic resonance: petrophysical and logging applications*, Elsevier.

Duschl, M., P. Galvosas, T. I. Brox, A. Pohlmeier, and H. Vereecken (2015), In situ determination of surface relaxivities for unconsolidated sediments, *Water Resour Res*, *51*(8), 6549-6563.

Ernst, R. R., G. Bodenhausen, and A. Wokaun (1987), *Principles of Nuclear Magnetic Resonance in one and two dimensions*, Clerendon Press.

Faure, P., and P. Coussot (2010), Drying of a model soil, *Phys Rev E*, *82*(3), 036303.

Faure, P., E. Michel, S. Sammartino, and C. Doussan (2011), Magnetic Resonance Imaging and Relaxometry as Tools to Investigate Water Distribution in Soils, *AIP Conference Proceedings*, *1330*(1), 69-72.

Faure, P., S. Caré, J. Magat, and T. Chaussadent (2012), Drying effect on cement paste porosity at early age observed by NMR methods, *Construction and Building Materials*, *29*(0), 496-503.

Feyen, J., D. Jacques, A. Timmerman, and J. Vanderborght (1998), Modelling Water Flow and Solute Transport in Heterogeneous Soils: A Review of Recent Approaches, *Journal of Agricultural Engineering Research*, *70*(3), 231-256.

Foley, I., S. A. Farooqui, and R. L. Kleinberg (1996), Effect of Paramagnetic Ions on NMR Relaxation of Fluids at Solid Surfaces, *Journal of Magnetic Resonance, Series A*, *123*(1), 95-104.

Gallagher, T. A., A. J. Nemeth, and L. Hacein-Bey (2008), An Introduction to the Fourier Transform: Relationship to MRI, *American Journal of Roentgenology*, *190*(5), 1396-1405.

García-Naranjo, J. C., I. V. Mastikhin, B. G. Colpitts, and B. J. Balcom (2010), A unilateral magnet with an extended constant magnetic field gradient, *Journal of Magnetic Resonance*, *207*(2), 337-344.

Grunewald, E., and R. Knight (2011), The effect of pore size and magnetic susceptibility on the surface NMR relaxation parameter, *Near Surface Geophysics*, *9*(2), 169-178.

Gummerson, R. J., C. Hall, W. D. Hoff, R. Hawkes, G. N. Holland, and W. S. Moore (1979), Unsaturated water flow within porous materials observed by NMR imaging, *Nature*, *281*(5726), 56-57.

Haber-Pohlmeier, S., S. Stapf, and A. Pohlmeier (2014), NMR Fast Field Cycling Relaxometry of Unsaturated Soils, *Appl Magn Reson*, *45*(10), 1099-1115.

Haber-Pohlmeier, S., M. Bechtold, S. Stapf, and A. Pohlmeier (2010), Water Flow Monitored by Tracer Transport in Natural Porous Media Using Magnetic Resonance Imaging, *Vadose Zone J*, *9*(4), 835-845.

Hahn, E. L. (1950), Spin Echoes, *Physical Review*, *80*(4), 580-594.

Hall, C., and W. D. Hoff (2011), *Water Transport in Brick, Stone and Concrete*, Taylor & Francis.

Hall, L. D., M. H. Gao Amin, E. Dougherty, M. Sanda, J. Votrubova, K. S. Richards, R. J. Chorley, and M. Cislerova (1997), MR properties of water in saturated soils and resulting loss of MRI signal in water content detection at 2 tesla, *Geoderma*, *80*(3–4), 431-448.

Han, J., and Z. Zhou (2013), Dynamics of Soil Water Evaporation during Soil Drying: Laboratory Experiment and Numerical Analysis, *The Scientific World Journal*, *2013*, 10.

Hanks, R. J., H. R. Gardner, and M. L. Faikbourn (1967), Evaporation of Water From Soils As Influenced By Drying With Wind or Radiation1, *Soil Sci. Soc. Am. J.*, *31*(5), 593-598.

Hennig, J. (1991), Echoes—how to generate, recognize, use or avoid them in MR-imaging sequences. Part II: Echoes in imaging sequences, *Concepts in Magnetic Resonance*, *3*(4), 179-192.

Hinedi, Z. R., Z. J. Kabala, T. H. Skaggs, D. B. Borchardt, R. W. K. Lee, and A. C. Chang (1993), Probing soil and aquifer material porosity with nuclear magnetic resonance, *Water Resour Res*, *29*(12), 3861-3866.

Huxman, T. E., B. P. Wilcox, D. D. Breshears, R. L. Scott, K. A. Snyder, E. E. Small, K. Hultine, W. T. Pockman, and R. B. Jackson (2005), Ecohydrological Implications Of Woody Plant Encroachment, *Ecology*, *86*(2), 308-319.

Jaeger, F., S. Bowe, H. Van As, and G. E. Schaumann (2009), Evaluation of 1H NMR relaxometry for the assessment of pore-size distribution in soil samples, *European Journal of Soil Science*, *60*(6), 1052-1064.

Jassal, R. S., M. D. Novak, and T. A. Black (2003), Effect of surface layer thickness on simultaneous transport of heat and water in a bare soil and its implications for land surface schemes, *Atmosphere-Ocean*, *41*(4), 259-272.

Katul, G. G., and M. B. Parlange (1992), A Penman-Brutsaert Model for wet surface evaporation, *Water Resour Res*, *28*(1), 121-126.

Keating, K., and R. Knight (2012), The effect of spatial variation in surface relaxivity on nuclear magnetic resonance relaxation rates, *Geophysics*, *77*(5), E365-E377.

Keita, E., P. Faure, S. Rodts, and P. Coussot (2013), MRI evidence for a receding-front effect in drying porous media, *Phys Rev E*, *87*(6), 062303.

Keulen, H., and D. Hillel (1974), A Simulation Study Of The Drying-Front Phenomenon, edited, pp. 270-273, The State Agricultural University, Wageningen, The Netherlands, and The Hebrew University, Faculty of Agriculture, Rehovot, Israel, (C) Williams & Wilkins 1974.

Kleinberg, S. A. Farooqui, and M. A. Horsfield (1993), T1/T2 Ratio and Frequency Dependence of NMR Relaxation in Porous Sedimentary Rocks, *Journal of Colloid and Interface Science*, *158*(1), 195-198.

Kleinberg, R. L. (1994), Pore size distributions, pore coupling, and transverse relaxation spectra of porous rocks, *Magnetic Resonance Imaging*, *12*(2), 271-274.

Kleinberg, R. L. (1999), Nuclear Magnetic Resonance, in *Experimental Methods in the Physical Sciences*, edited by W. Po-zen, pp. 337-385, Academic Press.

Kleinberg, R. L., and J. A. Jackson (2001), An introduction to the history of NMR well logging, *Concepts in Magnetic Resonance*, *13*(6), 340-342.

Koptyug, I. V. (2012), MRI of mass transport in porous media: Drying and sorption processes, *Progress in Nuclear Magnetic Resonance Spectroscopy*, *65*(0), 1-65.

Korb, and R. G. Bryant (2002), Magnetic field dependence of proton spin-lattice relaxation times, *Magnetic Resonance in Medicine*, *48*(1), 21-26.

Korb, J. P. (2011), Nuclear magnetic relaxation of liquids in porous media, *New Journal of Physics*, *13*(3), 035016.

Krause, P., D. P. Boyle, and F. Bäse (2005), Comparison of different efficiency criteria for hydrological model assessment, *Adv. Geosci.*, *5*, 89-97.

Laukien, D. D., and W. H. Tschopp (1994), Superconducting NMR magnet design, *Concepts in Magnetic Resonance*, *6*(4), 255-273.

Laurindo, J. B., and M. Prat (1998), Numerical and experimental network study of evaporation in capillary porous media. Drying rates, *Chemical Engineering Science*, *53*(12), 2257-2269.

Legates, D. R., and G. J. McCabe (1999), Evaluating the use of "goodness-of-fit" Measures in hydrologic and hydroclimatic model validation, *Water Resour Res*, *35*(1), 233-241.

Legtchenko, A. (2013), *Magnetic resonance imaging for groundwater*, John Wiley & Sons, Hoboken, NJ.

Lehmann, P., S. Assouline, and D. Or (2008), Characteristic lengths affecting evaporative drying of porous media, *Phys Rev E*, *77*(5).

Li, L., H. Han, and B. J. Balcom (2009), Spin echo SPI methods for quantitative analysis of fluids in porous media, *Journal of Magnetic Resonance*, *198*(2), 252-260.

Liu, B. C., W. Liu, and S. W. Peng (2005), Study of heat and moisture transfer in soil with a dry surface layer, *International Journal of Heat and Mass Transfer*, *48*(21–22), 4579-4589.

Marble, A. E., I. V. Mastikhin, B. G. Colpitts, and B. J. Balcom (2007), A compact permanent magnet array with a remote homogeneous field, *Journal of Magnetic Resonance*, *186*(1), 100-104.

Marica, F., F. G. Goora, and B. J. Balcom (2014), FID-SPI pulse sequence for quantitative MRI of fluids in porous media, *Journal of Magnetic Resonance*, *240*(0), 61-66.

Markl, M., and J. Leupold (2012), Gradient echo imaging, *Journal of Magnetic Resonance Imaging*, *35*(6), 1274-1289.

Mastikhin, I. V., and B. J. Balcom (2012), *Centric SPRITE MRI of Biomaterials with Short T_2**, John Wiley & Sons Ltd, Chichester, UK.

Maxwell, R. M., and S. J. Kollet (2008), Interdependence of groundwater dynamics and land-energy feedbacks under climate change, *Nature Geosci*, *1*(10), 665-669.

McIntosh, L. P. (2013), CPMG, in *CPMG. Encyclopedia of Biophysics*, edited by G. K. Roberts, pp. 386-386, Springer Berlin Heidelberg.

Meiboom, S., and D. Gill (1958), Modified Spin-Echo Method for Measuring Nuclear Relaxation Times, *Review of Scientific Instruments*, *29*(8), 688-691.

Merz, S., A. Pohlmeier, J. Vanderborght, D. van Dusschoten, and H. Vereecken (2014), Moisture profiles of the upper soil layer during evaporation monitored by NMR, *Water Resour Res*, *50*(6), 5184-5195.

Merz, S., A. Pohlmeier, J. Vanderborght, D. van Dusschoten, and H. Vereecken (2015a), Transition of stage I to stage II evaporation regime in the topmost soil: High-resolution NMR imaging, profiling and numerical simulation, *Microporous and Mesoporous Materials*, *205*(0), 3-6.

Merz, S., A. Pohlmeier, B. Balcom, R. Enjilela, and H. Vereecken (2015b), Drying of a Natural Soil Under Evaporative Conditions: A Comparison of Different Magnetic Resonance Methods, *Appl Magn Reson*, 1-18.

Mezrich, R. (1995), A perspective on k-space, *Radiology*, *195*(2), 297-315.

Mitchell, J., T. C. Chandrasekera, and L. F. Gladden (2010), Obtaining true transverse relaxation time distributions in high-field NMR measurements of saturated porous media: Removing the influence of internal gradients, *Journal of Chemical Physics*, *132*(24).

Mitchell, J., T. C. Chandrasekera, and L. F. Gladden (2013), Measurement of the true transverse nuclear magnetic resonance relaxation in the presence of field gradients, *The Journal of Chemical Physics*, *139*(7).

Moghadas, D., K. Z. Jadoon, J. Vanderborght, S. Lambot, and H. Vereecken (2013), Effects of Near Surface Soil Moisture Profiles During Evaporation on Far-Field Ground-Penetrating Radar Data: A Numerical Study, *Vadose Zone J.*, 1-11.

Moghadas, D., K. Z. Jadoon, J. Vanderborght, S. Lambot, and H. Vereecken (2014), Estimation of the near surface soil water content during evaporation using air-launched ground-penetrating radar, *Near Surface Geophysics*, *1*(1), 1-12.

Mohnke, O. (2014), Jointly deriving NMR surface relaxivity and pore size distributions by NMR relaxation experiments on partially desaturated rocks, *Water Resour Res*, *50*(6), 5309-5321.

Monteith, J. (1981), Evaporation and surface temperature, *Quarterly Journal of the Royal Meteorological Society*, *107*(451), 1-27.

Monteith, J., and M. Unsworth (1990), *Principles of environmental physics*, Academic Press.

Monteith, J. L. (1965), Evaporation and environment, 1965.

Mualem, Y. (1976), A new model for predicting the hydraulic conductivity of unsaturated porous media, *Water Resour Res*, *12*(3), 513-522.

Muir, C. E., and B. J. Balcom (2012), Pure Phase Encode Magnetic Resonance Imaging of Fluids in Porous Media, in *Annual Reports on NMR Spectroscopy*, edited by A. W. Graham, pp. 81-113, Academic Press.

Muir, C. E., and B. J. Balcom (2013), A comparison of magnetic resonance imaging methods for fluid content imaging in porous media, *Magnetic Resonance in Chemistry*, *51*(6), 321-327.

Müller-Petke, M., and U. Yaramanci (2015), Tools and Techniques: Nuclear Magnetic Resonance in *Treatise on Geophysics (Second Edition)*, edited, pp. 419-445, Elsevier, Oxford.

Nash, J. E., and J. V. Sutcliffe (1970), River flow forecasting through conceptual models part I — A discussion of principles, *Journal of Hydrology*, *10*(3), 282-290.

Neriah, A. B., S. Assouline, U. Shavit, and N. Weisbrod (2014), Impact of ambient conditions on evaporation from porous media, *Water Resour Res*, *50*, 6696–6712.

Nestle, N., T. Baumann, and R. Niessner (2002), Magnetic resonance imaging in environmental science, *Environmental science & technology*, *36*(7), 154A-160A.

Nestle, N., R. Morris, and T. Baumann (2007), Environmental NMR: Magnetic Resonance Imaging, in *eMagRes*, edited, John Wiley & Sons, Ltd, Hoboken, NJ.

Nimmo, J. R. (2009), Vadose Water, in *Encyclopedia of Inland Waters*, edited by G. E. Likens, pp. 766-777, Academic Press, Oxford.

Nimmo, J. R., and E. E. Miller (1986), The Temperature Dependence of Isothermal Moisture vs. Potential Characteristics of Soils1, *Soil Sci. Soc. Am. J.*(5), 1105-1113.

Nishimura, D. G. (1996), *Principles of magnetic resonance imaging*, Stanford University.

Novak, M. D. (2010), Dynamics of the near-surface evaporation zone and corresponding effects on the surface energy balance of a drying bare soil, *Agricultural and Forest Meteorology*, *150*(10), 1358-1365.

Novák, V. (2012), *Evapotranspiration in the Soil-Plant-Atmosphere System*, Springer.

Oki, T., and S. Kanae (2006), Global Hydrological Cycles and World Water Resources, *Science*, *313*(5790), 1068-1072.

Or, D., P. Lehmann, E. Shahraeeni, and N. Shokri (2013), Advances in Soil Evaporation Physics—A Review, *Vadose Zone J.*, *12*(4).

Paetzold, R. F., G. A. Matzkanin, and A. De Los Santos (1985), Surface Soil Water Content Measurement Using Pulsed Nuclear Magnetic Resonance Techniques1, *Soil Sci. Soc. Am. J.*, *49*(3), 537-540.

Penman, H. L. (1948), Natural Evaporation from Open Water, Bare Soil and Grass, *Proceedings of the Royal Society of London A: Mathematical, Physical and Engineering Sciences*, *193*(1032), 120-145.

Peters, A., and W. Durner (2008), Simplified evaporation method for determining soil hydraulic properties, *Journal of Hydrology*, *356*(1-2), 147-162.

Petrov, O. V., G. Ersland, and B. J. Balcom (2011), T2 distribution mapping profiles with phase-encode MRI, *Journal of Magnetic Resonance*, *209*(1), 39-46.

Philip, J. R., and D. A. De Vries (1957), Moisture movement in porous materials under temperature gradients, *Eos, Transactions American Geophysical Union*, *38*(2), 222-232.

Pickett, A. G., and M. M. Lemcoe (1959), An investigation of shear strength of the clay-water SYSTEM by radio-frequency spectroscopy, *Journal of Geophysical Research*, *64*(10), 1579-1586.

Pohlmeier, S. Haber-Pohlmeier, and S. Stapf (2009), A Fast Field Cycling Nuclear Magnetic Resonance Relaxometry Study of Natural Soils., *Vadose Zone J.*, *8*(3), 735-742.

Pohlmeier, S. Haber-Pohlmeier, M. Javaux, and H. Vereecken (2013), Magnetic Resonance Imaging (MRI) Techniques for Visualization of Root Growth and Root Water Uptake Processes in: Tomography and Imaging of Soil-Water-Root, *SSSA Special Publication*.

Pohlmeier, A., A. Oros-Peusquens, M. Javaux, M. I. Menzel, J. Vanderborght, J. Kaffanke, S. Romanzetti, J. Lindenmair, H. Vereecken, and N. J. Shah (2008), Changes in Soil Water Content Resulting from Ricinus Root Uptake Monitored by Magnetic Resonance Imaging., *Vadose Zone J.*, *7*(3), 1010-1017.

Pomerantz, A. E., P. Tilke, and Y.-Q. Song (2008), Inverting MRI measurements to heterogeneity spectra, *Journal of Magnetic Resonance*, *193*(2), 243-250.

Priestley, C. H. B., and R. J. Taylor (1972), On the Assessment of Surface Heat Flux and Evaporation Using Large-Scale Parameters, *Monthly Weather Review*, *100*(2), 81-92.

Pusey, E., R. B. Lufkin, R. K. Brown, M. A. Solomon, D. D. Stark, R. W. Tarr, and W. N. Hanafee (1986), Magnetic resonance imaging artifacts: mechanism and clinical significance, *RadioGraphics*, *6*(5), 891-911.

Qiu, G. Y., and J. Ben-Asher (2010), Experimental Determination of Soil Evaporation Stages with Soil Surface Temperature., *Soil Sci. Soc. Am. J.*, *74*(1), 13-22.

Raich, H., and P. Blümler (2004), Design and construction of a dipolar Halbach array with a homogeneous field from identical bar magnets: NMR Mandhalas, *Concepts in Magnetic Resonance Part B: Magnetic Resonance Engineering*, *23B*(1), 16-25.

Rezaei, M., P. Seuntjens, R. Shahidi, I. Joris, W. Boënne, B. Al-Barri, and W. Cornelis (2016), The relevance of in-situ and laboratory characterization of sandy soil hydraulic properties for soil water simulations, *Journal of Hydrology*, *534*, 251-265.

Richards, L. A. (1931), Capillary Conduction Of Liquids Through Porous Mediums, *Physics*, *1*(5), 318-333.

Robinson, D. A., C. S. Campbell, J. W. Hopmans, B. K. Hornbuckle, S. B. Jones, R. Knight, F. Ogden, J. Selker, and O. Wendroth (2008), Soil Moisture Measurement for Ecological and Hydrological Watershed-Scale Observatories: A Review, *Vadose Zone J.*(1), 358-389.

Rogowski, A. S. (1971), Watershed Physics: Model of the Soil Moisture Characteristic, *Water Resour Res*, *7*(6), 1575-1582.

Rossel, V. I. Adamchuk, K. A. Sudduth, N. J. McKenzie, and C. Lobsey (2011), Chapter Five - Proximal Soil Sensing: An Effective Approach for Soil Measurements in Space and Time, in *Advances in Agronomy*, edited by L. S. Donald, pp. 243-291, Academic Press.

Rothfuss, Y., S. Merz, J. Vanderborght, N. Hermes, A. Weuthen, A. Pohlmeier, H. Vereecken, and N. Brüggemann (2015), Long-term and high-frequency non-destructive monitoring of water stable isotope profiles in an evaporating soil column, *Hydrol. Earth Syst. Sci.*, *19*(10), 4067-4080.

Saito, H., J. Šimůnek, and B. P. Mohanty (2006), Numerical Analysis of Coupled Water, Vapor, and Heat Transport in the Vadose Zone, *Vadose Zone J.*, *5*(2), 784-800.

Sakai, M., N. Toride, and J. Šimůnek (2009), Water and Vapor Movement with Condensation and Evaporation in a Sandy Column., *Soil Sci. Soc. Am. J.*(3), 707-717.

Scherer, G. W. (1990), Theory of Drying, *Journal of the American Ceramic Society*, *73*(1), 3-14.

Schindler, U., W. Durner, G. von Unold, L. Mueller, and R. Wieland (2010a), The evaporation method: Extending the measurement range of soil hydraulic properties using the air-entry pressure of the ceramic cup, *Journal of Plant Nutrition and Soil Science*, *173*(4), 563-572.

Schindler, U., W. Durner, G. Von Unold, L. Mueller, and R. Wieland (2010b), The evaporation method: Extending the measurement range of soil hydraulic properties using the air-entry pressure of the ceramic cup, *Journal of Plant Nutrition and Soil Science*, *173*(4), 563-572.

Schlünder, E. U. (2004), Drying of Porous Material During the Constant and the Falling Rate Period: A Critical Review of Existing Hypotheses#, *Drying Technology*, *22*(6), 1517-1532.

Seager, R., et al. (2007), Model Projections of an Imminent Transition to a More Arid Climate in Southwestern North America, *Science*, *316*(5828), 1181-1184.

Sellers, P. J., et al. (1997), Modeling the Exchanges of Energy, Water, and Carbon Between Continents and the Atmosphere, *Science*, *275*(5299), 502-509.

Seneviratne, S. I., T. Corti, E. L. Davin, M. Hirschi, E. B. Jaeger, I. Lehner, B. Orlowsky, and A. J. Teuling (2010), Investigating soil moisture–climate interactions in a changing climate: A review, *Earth-Science Reviews*, *99*(3–4), 125-161.

Shahraeeni, E., P. Lehmann, and D. Or (2012), Coupling of evaporative fluxes from drying porous surfaces with air boundary layer: Characteristics of evaporation from discrete pores, *Water Resour Res*, *48*(9), W09525.

Shokri, and Or (2011), What determines drying rates at the onset of diffusion controlled stage-2 evaporation from porous media?, *Water Resour. Res.*, *47*(9), W09513.

Shokri, and Sahimi (2012), Structure of drying fronts in three-dimensional porous media, *Phys Rev E*, *85*(6), 066312.

Shokri, P. Lehmann, P. Vontobel, and D. Or (2008), Drying front and water content dynamics during evaporation from sand delineated by neutron radiography, *Water Resour. Res.*, *44*(6), W06418.

Shokri, N., P. Lehmann, and D. Or (2010), Liquid-phase continuity and solute concentration dynamics during evaporation from porous media: Pore-scale processes near vaporization surface, *Phys Rev E*, *81*(4), 046308.

Simunek, J., M. T. van Genuchten, and M. Sejna (2008), *Modeling subsurface water flow and solute transport with HYDRUS and related numerical software packages*, 95-114 pp.

Sněhota, M., M. Císlerová, M. H. G. Amin, and L. D. Hall (2010), Tracing the Entrapped Air in Heterogeneous Soil by Means of Magnetic Resonance Imaging., *Vadose Zone J.*, *9*(2), 373-384.

Song (2010), Recent Progress of Nuclear Magnetic Resonance Applications in Sandstones and Carbonate Rocks, *Vadose Zone J*, *9*(4), 828-834.

Stafford, J. V. (1988), Remote, non-contact and in-situ measurement of soil moisture content: a review, *Journal of Agricultural Engineering Research*, *41*(3), 151-172.

Stingaciu, L. R., L. Weihermüller, S. Haber-Pohlmeier, S. Stapf, H. Vereecken, and A. Pohlmeier (2010), Determination of pore size distribution and hydraulic properties using nuclear magnetic resonance relaxometry: A comparative study of laboratory methods, *Water Resour. Res.*, *46*(11), W11510.

Stingaciu, L. R., A. Pohlmeier, P. Blümler, L. Weihermüller, D. van Dusschoten, S. Stapf, and H. Vereecken (2009), Characterization of unsaturated porous media by high-field and low-field NMR relaxometry, *Water Resour Res*, *45*(8).

Straley, C., H. Vinegar, C. Morriss, and A. Soc Core (1994), Core analysis by low field NMR, *1994 International Symposium of the Society of Core Analysts, Proceedings*, 43-56.

Sucre, O., A. Pohlmeier, A. Minière, and B. Blümich (2011), Low-field NMR logging sensor for measuring hydraulic parameters of model soils, *Journal of Hydrology*, *406*(1–2), 30-38.

Talabi, O. A., S. Alsayari, M. J. Blunt, H. Dong, and X. Zhao (2009), Predictive Pore Scale Modeling: From 3D Images to Multiphase Flow Simulations, edited, Society of Petroleum Engineers.

Teng, J. D., N. Yasufuku, S. Zhang, and Y. He (2016), Modelling water content redistribution during evaporation from sandy soil in the presence of water table, *Computers and Geotechnics*, *75*, 210-224.

Too, V., C. Omuto, E. Biamah, and J. Obiero (2014), Review of Soil Water Retention Characteristic (SWRC) Models between Saturation and Oven Dryness. , *Open Journal of Modern Hydrology*, *4*, 173-182.

Tran, D. T. Q., D. G. Fredlund, and D. H. Chan (2015), Improvements to the calculation of actual evaporation from bare soil surfaces, *Canadian Geotechnical Journal*, *53*(1), 118-133.

Trenberth, K. E., J. T. Fasullo, and J. Kiehl (2009), Earth's Global Energy Budget, *Bulletin of the American Meteorological Society*, *90*(3), 311-323.

Valckenborg, R. M. E., L. Pel, K. Hazrati, K. Kopinga, and J. Marchand (2001), Pore water distribution in mortar during drying as determined by NMR, *Mat. Struct.*, *34*(10), 599-604.

Van der Heijden, G. H. A., H. P. Huinink, L. Pel, and K. Kopinga (2009), Non-isothermal drying of fired-clay brick, an NMR study, *Chemical Engineering Science*, *64*(12), 3010-3018.

van Genuchten, M. T. (1980), A Closed-form Equation for Predicting the Hydraulic Conductivity of Unsaturated Soils1, *Soil Sci. Soc. Am. J.*, *44*(5), 892-898.

Vanderborght, J., A. Graf, C. Steenpass, B. Scharnagl, N. Prolingheuer, M. Herbst, H. J. H. Franssen, and H. Vereecken (2010), Within-Field Variability of Bare Soil Evaporation Derived from Eddy Covariance Measurements, *Vadose Zone J*, *9*(4), 943-954.

Varian (2007), VnmrJ Imaging User Guide, edited, Varian, Inc., Palo Alto, California.

Vereecken, H., J. A. Huisman, H. Bogena, J. Vanderborght, J. A. Vrugt, and J. W. Hopmans (2008), On the value of soil moisture measurements in vadose zone hydrology: A review, *Water Resour Res*, *44*(4), W00D06.

Vereecken, H., et al. (2016), Modeling Soil Processes: Review, Key Challenges, and New Perspectives, *Vadose Zone J*, *15*(5).

Wang, X. (2015), Vapor Flow Resistance of Dry Soil Layer to Soil Water Evaporation in Arid Environment: An Overview, *Water*, *7*(8).

Washburn, K. E., C. D. Eccles, and P. T. Callaghan (2008), The dependence on magnetic field strength of correlated internal gradient relaxation time distributions in heterogeneous materials, *Journal of Magnetic Resonance*, *194*(1), 33-40.

Watson, A. T., and C. T. P. Chang (1997), Characterizing porous media with NMR methods, *Progress in Nuclear Magnetic Resonance Spectroscopy*, *31*(4), 343-386.

Williams, A. B., and F. J. Taylor (1995), *Electronic filter design handbook (third ed.)*, 600 pp., McGraw-Hill, Inc.

Wolter, B., and M. Krus (2005), Moisture Measuring with Nuclear Magnetic Resonance (NMR), in *Electromagnetic Aquametry*, edited by K. Kupfer, pp. 491-515, Springer Berlin Heidelberg.

Wythers, K. R., W. K. Lauenroth, and J. M. Paruelo (1999), Bare-Soil Evaporation Under Semiarid Field Conditions, *Soil Sci. Soc. Am. J.*(5), 1341-1349.

Yiotis, A. G., A. K. Stubos, A. G. Boudouvis, and Y. C. Yortsos (2001), A 2-D pore-network model of the drying of single-component liquids in porous media, *Advances in Water Resources*, *24*(3–4), 439-460.

Yiotis, A. G., I. N. Tsimpanogiannis, A. K. Stubos, and Y. C. Yortsos (2007), Coupling between external and internal mass transfer during drying of a porous medium, *Water Resour. Res.*, *43*(6), W06403.

Zeng, Y. (2013), in *Coupled Dynamics in Soil*, edited, Springer Berlin Heidelberg.

Zhu, Z. Q., and D. Howe (2001), Halbach permanent magnet machines and applications: a review, IET, 2001.

Band / Volume 363
Quantitative Analyse der Lithiumverteilung in Kathoden- und Elektrolyt-Dünnschichten für Festkörperbatterien
C. Dellen (2017), vi, 161 pp
ISBN: 978-3-95806-214-6

Band / Volume 364
Intragruppentrennung Seltener Erden mittels neuer phosphororganischer Liganden
S. Hadić (2017), VIII, 164 pp
ISBN: 978-3-95806-215-3

Band / Volume 365
Automated Magnetic Divertor Design for Optimal Power Exhaust
M. Blommaert (2017), xxiv, 220 pp
ISBN: 978-3-95806-216-0

Band / Volume 366
PEM-Elektrolyse-Systeme zur Anwendung in Power-to-Gas Anlagen
G. Tjarks (2017), IV, 135 pp
ISBN: 978-3-95806-217-7

Band / Volume 367
Fundamental Insights into the Radium Uptake into Barite by Atom Probe Tomography and Electron Microscopy
J. Weber (2017), IX, 160 pp
ISBN: 978-3-95806-220-7

Band / Volume 368
Entwicklung von elektronenleitenden Schutzschichten gegen die anodische Auflösung von Stromsammlern in neuartigen „Dual-Ionen"-Energiespeichern
G. Teucher (2017), VIII, 119 pp
ISBN: 978-3-95806-222-1

Band / Volume 369
Herstellung und Charakterisierung oxiddispersionsverstärkter Haftvermittlerschichten
J. Bergholz (2017), V, 133, II pp
ISBN: 978-3-95806-223-8

Band / Volume 370
Performance of Plasma Facing Materials under Thermal and Plasma Exposure
I. Steudel (2017), XVI, 150 pp
ISBN: 978-3-95806-226-9

Band / Volume 371
The Impact of Transient Thermal Loads on Beryllium as Plasma Facing Material
B. Spilker (2017), XII, 134 pp
ISBN: 978-3-95806-227-6

Band / Volume 372
Analysis and Simulation of Macroscopic Defects in Cu(In,Ga)Se_2 Photovoltaic Thin Film Modules
B. Misic (2017), iv, 147 pp
ISBN: 978-3-95806-228-3

Band / Volume 373
Chemical and physical properties of sodium ionic conductors for solid-state batteries
M. Guin (2017), ix, 126 pp
ISBN: 978-3-95806-229-0

Band / Volume 374
Prediction of Oxidation Induced Life Time for FCC Materials at High Temperature Operation
R. Duan (2017), vi, 180 pp
ISBN: 978-3-95806-230-6

Band / Volume 375
Microstructure Evolution of Laves Phase Strengthened Ferritic Steels for High Temperature Applications
J. K. Lopez Barrilao (2017), XVI, 134 pp
ISBN: 978-3-95806-231-3

Band / Volume 376
Drying front formation in topmost soil layers as evaporative restraint
Non-invasive monitoring by magnetic resonance and numerical simulation
S. Merz (2017), xxii, 108 pp
ISBN: 978-3-95806-234-4

Weitere ***Schriften des Verlags im Forschungszentrum Jülich*** unter
http://wwwzb1.fz-juelich.de/verlagextern1/index.asp

Energie & Umwelt /
Energy & Environment
Band / Volume 376
ISBN 978-3-95806-234-4